SYNTHESIS OF ONE-DIMENSIONAL NANOCOMPOSITES BASED ON ALUMINA NANOFIBRES AND THEIR CATALYTIC APPLICATIONS

Submitted by

Erming Liu

To the Discipline of Chemistry, Queensland University of Technology, in fulfilment of the requirements of the degree of Doctor of Philosophy

February 2011

Keywords

1D nanostructure

Alumina nanofibres

Core-shell structure

Hierarchical structure

Marco-mesoporous material

Nanocomposite

Photocatalyst

Solid superacid

Titania or anatase

Zirconia

Abstract

Materials with one-dimensional (1D) nanostructure are important for catalysis. They are the preferred building blocks for catalytic nanoarchitecture, and can be used to fabricate designer catalysts. In this thesis, one such material, alumina nanofibre, was used as a precursor to prepare a range of nanocomposite catalysts. Utilising the specific properties of alumina nanofibres, a novel approach was developed to prepare macro-mesoporous nanocomposites, which consist of a stacked, fibrous nanocomposite with a core-shell structure. Two kinds of fibrous ZrO_2/Al_2O_3 and TiO_2/Al_2O_3 nanocomposites were successfully synthesised using boehmite nanofibers as a hard temperate and followed by a simple calcination. The alumina nanofibres provide the resultant nanocomposites with good thermal stability and mechanical stability.

A series of one-dimensional (1D) zirconia/alumina nanocomposites were prepared by the deposition of zirconium species onto the 3D framework of boehmite nanofibres formed by dispersing boehmite nanofibres into a butanol solution, followed by calcination at 773 K. The materials were characterised by X-ray diffraction (XRD), Scanning electron microscopy (SEM), Transmission electron microscope (TEM), N_2 adsorption/desorption, Infrared Emission Spectroscopy (IES), and Fourier Transform Infrared spectroscopy (FT-IR). The results demonstrated that when the molar percentage, X, X=100*Zr/(Al+Zr), was > 30%, extremely long ZrO_2/Al_2O_3 composite nanorods with evenly distributed ZrO_2 nanocrystals formed on their surface. The stacking of such nanorods gave rise to a new kind of macroporous material without the use of any organic space filler\template or other specific drying techniques. The mechanism for the formation of these long ZrO_2/Al_2O_3 composite nanorods is proposed in this work.

A series of solid-superacid catalysts were synthesised from fibrous ZrO_2/Al_2O_3 core and shell nanocomposites. In this series, the zirconium molar percentage was varied from 2 % to

50 %. The ZrO_2/Al_2O_3 nanocomposites and their solid superacid counterparts were characterised by a variety of techniques including ^{27}Al MAS-NMR, SEM, TEM, XPS, Nitrogen adsorption and Infrared Emission Spectroscopy. NMR results show that the interaction between zirconia species and alumina strongly correlates with pentacoordinated aluminium sites. This can also be detected by the change in binding energy of the 3d electrons of the zirconium.

The acidity of the obtained superacids was tested by using them as catalysts for the benzolyation of toluene. It was found that a sample with a 50 % zirconium molar percentage possessed the highest surface acidity equalling that of pristine sulfated zirconia despite the reduced mass of zirconia. Preparation of hierarchically macro-mesoporous catalyst by loading nanocrystallites on the framework of alumina bundles can provide an alternative system to design advanced nanocomposite catalyst with enhanced performance.

A series of macro-mesoporous TiO_2/Al_2O_3 nanocomposites with different morphologies were synthesised. The materials were calcined at 723 K and were characterised by X-ray diffraction (XRD), Scanning electron microscopy (SEM), Transmission electron microscope (TEM), N_2 adsorption/desorption, Infrared Emission Spectroscopy (IES), and UV-visible spectroscopy (UV-visible). A modified approach was proposed for the synthesis of 1D (fibrous) nanocomposite with higher Ti/Al molar ratio (2:1) at lower temperature ($<100^oC$), which makes it possible to synthesize such materials on industrial scale.

The performances of a series of resultant TiO_2/Al_2O_3 nanocomposites with different morphologies were evaluated as a photocatalyst for the phenol degradation under UV irradiation. The photocatalyst (Ti/Al =2) with fibrous morphology exhibits higher activity than that of the photocatalyst with microspherical morphology which indeed has the highest Ti to Al molar ratio (Ti/Al =3) in the series of as-synthesised hierarchical TiO_2/Al_2O_3 nanocomposites. Furthermore, the photocatalytic performances, for the fibrous nanocomposites with Ti/Al=2, were optimized by calcination at elevated temperatures. The

nanocomposite prepared by calcination at 750^{o}C exhibits the highest catalytic activity, and its performance per TiO_2 unit is very close to that of the gold standard, Degussa P 25. This work also emphasizes two advantages of the nanocomposites with fibrous morphology: (1) the resistance to sintering, and (2) good catalyst recovery.

Contents

Keywords i

Abstract ii

List of Figures vii

List of Tables xi

List of Abbreviations xiii

Statement of Original Authorship xiv

Acknowledgments xv

CHAPTER 1: INTRODUCTION 1

1.1 Background and motivation 1

1.2 The aims of this thesis 3

1.3 Account of scientifc progress 3

1.4 Thesis Outline 4

1.5 References 5

CHAPTER 2: LITERATURE REVIEW 7

2.1 Preparation of boehmite nanofibres in various synthetic systems 8

2.2 The formation mechanism of boehmite nanofibres 12

2.3 The unique properties of boehmite and alumina nanofibres 16

2.3.1 Dispersibility of boehmite nanofibres 16

2.3.2 Large pore size and pore volume 17

2.3.3 Thermal stability 20

2.4 Nanocomposite based on alumina nanofibres and their applications 22

2.4.1 synthesis of nanocomposites 22

2.4.2 applications of nanocomposites 24

2.5 Summary and Implications 28

2.6 Reference and notes 29

CHAPTER 3: FABRICATION OF MACRO-MESOPOROUS ZIRCONIA-ALUMINA MATERIALS WITH A 1D HIERARCHICAL STRUCTURE 35

3.1 Introduction 35

3.2 Experimental section 37

3.3 Results and discussion 39

3.4 Conclusion 64

3.5 Reference and notes 65

CHAPTER 4: SULFATED 1D ZIRCONIA-ALUMINA CORE-SHELL NANOCOMPOSITES: A NOVEL SUPERACID CATALYST WITH HIERARCHICALLY MACRO-MESOPOROUS NANOSTRUCTURE 71

4.1 Experimental section 74

4.2 Results 78

4.3 Discussion 96

4.4 Conclusion 98

4.5 Reference and notes 99

CHAPTER 5: FABRICATION OF MACRO-MESOPOROUS TITANIA-ALUMINA NANOCOMPOSITES WITH A 1D HIERARCHICAL STRUCTURE 103

5.1 Introduction 103

5.2 Experimental section 105

5.3 Results and discussion 106

5.4 Conclusion 122

5.5 Reference and notes 124

CHAPTER 6: PHOTOCATALYSIS OF TIO_2-AL_2O_3 CORE-SHELL NANOCOMPOSITES WITH DIFFERENT MORPHOLOGIES 129

6.1 Introduction 129

6.2 Experimental section 130

6.3 Result and discussion 132

6.3.1 Effects of catalyst morphologies 132

6.3.2 The effect of calcination temperature 139

6.4 Conclusion 147

6.5 Reference and notes 147

CHAPTER 7: CONCLUSIONS 151

APPENDICES 160

List of Figures

Chapter 2

Figure 1. Boehmite nanofibres synthesised by Bugosh. (Image from Reference 18) 8

Figure 2. The Morphology of boehmite nanofibres synthesised at various temperatures A) 155°C B) 175°C C) 190°C and D) 220°C (Image from Reference 27.) 12

Figure 3. Schematic illustration of the surfactant-induced fiber formation change mechanism. (Image from Reference 13.) 13

Figure 4. Schematic illustration of a potential mechanism for the assembly and disassembly of boehmite nanofibres (a) Hydrolysis of aluminium alkoxide generates amorphous alumina hydrate gels. (b) When the solution is heated, boehmite nanocrystallites are formed at the expense of amorphous alumina hydrate gels and assembly in liquid phase. (c) Boehmite nanofibers continue to grow. (Image from Reference 36.) 14

Figure 5. Boehmite structure and the possible adsorption configuration of sulfate on the (010) plane (a) and (001) plane, no adsorption on (100) plane (c). (Image from Reference 37.) 15

Figure 6. Schematic drawing of the particle structure in the dispersions of boehmite nanofibres with different LiCl concentrations (Image from Reference 41.) 17

Figure 7. N_2 absorption and desorption isotherms and pore-size distributions (insets) for the boehmite nanofibres (Image from Reference 42.) 18

Figure 8. Effect of thermal treatment on surface areas of (■) Al_2O_3 nanofibres and (□) Al_2O_3 nanopowder. (Image from Reference 16.) 21

Chapter 3

Figure 1. XRD patterns of composite nanofibres (a) pristine boehmite nanofibres, (b) Zr-5 (Zr%=5 mol%), (c) Zr-10 (Zr%=10 mol%), (d) Zr-15 (Zr%=15 mol%), (e) Zr-30 (Zr%=30 mol%), (f) Zr-50 (Zr%=50 mol%) 39

Figure 2. Powder XRD patterns of a) Al_2O_3 nanofibres; b) Zr-5-500; c) Zr-10-500; d) Zr-15-500; e) Zr-30-500; f) Zr-50-500; g) Pristine ZrO_2 (M and T represent monoclinic ZrO_2 and tetragonal ZrO_2, respectively) 40

Figure 3. SEM images of 1D ZrO_2/Al_2O_3 nanocomposites obtained by calcination at 500°C: a) Zr-5-500; b) Zr-10-500; c) Zr-15-500; d) Zr-30-500; e) Zr-50-500; f) Zr-50-500 at a larger scale 43

Figure 4. TEM image for γ-Al_2O_3 nanofibres and the 1D nanocomposite with 50 mol% Zr 45

Figure 5. (a) Typical conventional TEM bright field, (b) the select-area electron diffraction pattern taken from this area, (c) the dark field image using the intensity of the (400) diffraction spot of γ-Al_2O_3 (shown as inset image) and (d) the dark field by selecting one of the diffraction rings of zirconia for imaging 47

Figure 6. FT-IR spectra of a) pristine ZrO_2, b) γ-Al_2O_3 nanofibres, c) Zr-5-500, d) Zr-10-500, e) Zr-15-500, f) Zr-30-500, g) Zr-50-500 48

Figure 7. Infrared emission spectra in the region of OH stretching obtained at 400°C. a) γ-Al_2O_3 nanofibres, b) Zr-5-500, c) Zr-10-500, d) Zr-15-500, e) Zr-30-500, f) Zr-50-500, g) pristine ZrO_2 50

Figure 8. Nitrogen adsorption and desorption isotherms for some representative samples with various Zr molar percentage. a) γ-Al_2O_3 nanofibres, b) Zr-15-500, c) Zr-30-500, d) Zr-50-500 52

Figure 9. Pore size distributions for samples with various Zr molar percentage 54

Figure 10. SEM images of thin films made from a) Dry boehmite nanofibres butanol suspension and b) wet boehmite nanofibres gel 56

Figure 11. Schematic illustration of the formation mechanism of 1D zirconia/alumina nanocomposites and the macroporous material constituted by their 1D nanostructure: a) boehmite nanofibres are stabilized in butanol solution by forming an aggregated structure. b) 3D grid is formed by connected boehmite nanofibres. c) Zirconium butoxide is exclusively hydrolysed on the surface of boehmite nanofibres. d) 1D structure is maintained after separation and naturally packed into a macroporous material 57

Figure 12. Infrared emission spectra of the Zr-50 characterised at a) 100°C; b) 300°C; c) 400°C; d) 450°C; e) 500°C 58

Figure 13. *In-situ* hot-stage Raman spectra of Zr-50 characterised from 100°C to 500°C: a) 100°C, b) 300°C c) 400°C d) 450°C e) 500°C 60

Figure 14. SEM image and XRD pattern for the sample with 50 % Zr molar percentage after calcination at 1000 °C 62

Figure 15. HRTEM image showing the embedment of ZrO_2 nanocrystallites on Al_2O_3 nanofibres 63

Chapter 4

Figure 1. Observed Zr percentage in samples as a function of nominal Zr percentage 78

Figure 2. XRD patterns for the sulfated 1D zirconia-alumina nanocomposites, alumina nanofibres and zirconia obtained by calcining at 650°C for 3 h. (a) sulfated alumina nanofibres (b) S-Zr-2, (c) S-Zr-5, (d) S-Zr-10, (e) S-Zr-15, (f) S-Zr-30, (g) S-Zr-50 and (h) sulfated zirconia. M and T represent monoclinic phase and tetragonal phase, respectively. The patterns in (H) underwent a 0.6-fold Y-scale reduction 79

Figure 3. ^{27}Al MAS NMR spectra of sulfated pristine alumina nanofibres and 1D ZrO_2/Al_2O_3 nanocomposites obtained by calcination at 650°C: (a) SA-F; (b) S-Zr-2; (c) S-Zr-5; (d) S-Zr-10; (e) S-Zr-15; (f) S-Zr-30 82

Figure 4. Separated components of (a) S-Zr-30; and (b) S-Zr-50 obtained by spectrum fitting procedure. *quadrupolar sideband 83

Figure 5. SEM images of sulfated pristine alumina nanofibres and 1D ZrO_2/Al_2O_3 nanocomposites obtained by calcination at 650°C: A) SA-F; B) S-Zr-2; C) S-Zr-5; D) S-Zr-10; E) S-Zr-15; F) S-Zr-30; G) S-Zr-50; H) S-Zr-50 at a larger scale 84

Figure 6. TEM image for a) S-Zr-30 and b) S-Zr-50 superacid 85

Figure 7. XPS results a) XPS surface Zr/Al molar ratio as a function of bulk Zr/Al molar ratio, b) Zr 3d XPS spectra of S-Zr-30 and c) Zr 3d XPS spectra of S-Zr-50 86

Figure 8. Nitrogen adsorption and desorption isotherms for some representative samples with various Zr content 88

Figure 9. Pore size distributions for samples with various Zr content 90

Figure 10. Infrared emission spectra of S-Zr-50 in the region 1000~ 2000 cm^{-1} from 50°C to 350°C at 100°C intervals 93

Figure 11. Benzoylation of toluene at 110°C 95

Chapter 5

Figure 1. SEM images of a) boehmite nanofibres b) a-Ti-1-450 c) Ti-1-450 d) Ti-1.5-450 e) Ti-2.0-450 f) Ti-3.0-450 109

Figure 2. TEM image for the nanocomposites with different morphologies a) densely aggregated morphology (a-Ti-1-450) b) 1D nanostructure (Ti-2-450) c) titania microsphere (Ti-3-450) 110

Figure 3. X-ray diffraction patterns of a) pristine Al_2O_3 nanofibers b) a-Ti-1-450 c) Ti-1-450 d) Ti-1.5-450 e) Ti-2.0-450 f) Ti-3.0-450 113

Figure 4. UV-visible spectra of as-synthesised TiO_2/Al_2O_3 nanocomposites 114

Figure 5. Determination of the indirect interband transition energies for as-synthesized TiO_2/Al_2O_3 nanocomposites 117

Figure 6. Nitrogen adsorption and desorption isotherms for as-synthesized nanocomposites 118

Figure 7. Pore size distributions for TiO_2/Al_2O_3 nanocomposites 119

Figure 8. Infrared emission spectra of a) a representative sample (Ti-2-450) measured from 200°C to 450°C and b) all TiO_2/Al_2O_3 nanocomposites measured at 450°C 121

Chapter 6

Figure 1. Wavelength spectra of the light sources 132

Figure 2. Temporal course of the photodegradation of the phenol in the presence of TiO_2/Al_2O_3 nanocomposites with various Ti/Al molar ratios with all the samples calcined at 450°C 132

Figure 3. Linear fitness of the kinetics of phenol degradation for various catalysts during irradiation 134

Figure 4. Uv-visible absorption band of sulforhodamine-B and its chemical structures 136

Figure 5. Temporal course of the photodegradation of the sulforhodamine B 138

Figure 6. XRD patterns for the sample with 2 Ti/Al molar ratios calcined from 450°C to 900°C 140

Figure 7. UV-visible spectra of calcined TiO_2/Al_2O_3 nanocomposites (Ti/Al=2) 143

Figure 8. Temporal course of the photodegradation of phenol for the calcined nanocomposites (Ti/Al=2) 144

Figure 9. Specific surface area of calcined nanocomposites as a function of crystal sizes 145

List of Tables

Chapter 2

Table 1. Origin and textural properties of the γ-alumina supports 19

Table 2. Textural properties of 3 kinds of γ-alumina nanofibres 20

Chapter 3

Table 1. Lattice parameters evolvement of γ-Al_2O_3 phase and tetragonal zirconia phase for the calcined sample with various Zr/Al molar ratios 42

Table 2. Crystallite dimension in (101) direction of tetragonal phase for pristine zirconia and zirconia deposited on alumina nanofibres with various zirconia content (The data were derived from X-ray diffraction patterns) 42

Table 3. Pore structures of γ-Al_2O_3 nanofibres and as-synthesised nanocomposites 55

Table 4. Structure change for the sample with 50 % Zr molar percentage after calcining at 500 ^oC, 750 ^oC and 1000 ^oC for 3 hours 63

Chapter 4

Table 1. Crystallite dimension in (101) direction for sulfated tetragonal zirconium and that deposited on alumina nanofibres with various zirconia content (The data were derived from X-ray diffraction patterns) 80

Table 2. The relative percentages of the AlO_4, AlO_5 and AlO_6 species for the nanocomposites with various Zr content (obtained by spectrum simulation procedure) 83

Table 3. The binding energies of $Zr3d_{5/2}$ photopeak corresponding to two kinds of Zr species and their relative ratio in XPS spectra 87

Table 4. Powder properties of the sulfated 1D ZrO_2/Al_2O_3 nanocomposites with various Zr molar percentage and sulfated alumina nanofibres obtained by calcination at 650^oC 91

Table 5. Effect of Water Adsorption on S=O including Stretching Wavenumber, Bond Order and Partial Charge on Oxygen 94

Chapter 5

Table 1. XPS binding energies for all the nanocomposites and their Ti/Al molar ratios measured by EDX and XPS respectively 110

Table 2. The crystallite dimensions of anatase phase of titania calculated from both the Uv-spectra and X-ray diffraction patterns 116

Table 3. Pore structures of as-synthesised TiO_2/Al_2O_3 nanocomposites 120

Chapter 6

Table 1. Physical properties of resultant TiO_2/Al_2O_3 nanocomposites.....131

Table 2. Crystal sizes and phase component of the fibrous nanocomposites (Ti/Al=2) calcined at various temperatures.....141

Table 3. Rate constant and turnover frequency (initial activities) in the photodegradation of phenol over calcined nanocomposites.....145

List of Abbreviations

1D	One dimensional
BET	Brunauer-Emmett-Teller
DFT	Density functional theory
DLVO	Derjaguin-Landau-Verwey-Overbeek theory
EDX	Energy dispersive X-Ray spectroscopy
FT-IR	Fourier Transform Infrared spectroscopy
IES	FT-IR emission spectrescopy
MAS-NMR	Magic angle spinning nuclear magnetic resonance
SEM	Scanning electron microscopy
SRB	Sulforhodamine B
TEM	Transmission electron microscopy
TOF	Turnover frequency
UV-visible	Ultraviolet-visible
XPS	X-ray photoelectron spectroscopy
XRD	X-ray diffraction

Statement of Original Authorship

The work contained in this thesis has not been previously submitted to meet requirements for an award at this or any other higher education institution. To the best of my knowledge and belief, the thesis contains no material previously published or written by another person except where due reference is made.

Signature: 
(Erming Liu)

Date: 28-Feb-2011

Acknowledgments

My doctoral research work was realised under the supervision of Dr. Wayde N. Martens and Prof. Ray L. Frost. I would like to express my deepest appreciations to them for their guidance and discussions during the course of this work. Their support, patience, and understanding are unforgettable in my life.

Many thanks are given to Dr Xuebin Ke, A/Prof. Xuzhuang Yang, Dr Dongjiang Yang, Dr Xi Chen and Dr Zhanfeng Zheng for their advice and discussions.

I am grateful to Mr Ashley J. Locke and Mr Massimiliano Vezzoli for their friendship, support and help during the hardest time of this work. Many thanks also go to the students Blain Paul, Jing Yang and Sarina Sarina for their friendship.

I cannot forget to mention Mr Pat Stevens, Mr Tony Raftery, Dr Loc Duong, Dr Liew Rintoul and Dr Thor Bostrom for their assistance during various experiments and for their many suggestions.

Moreover, the financial and infra-structure support from the Queensland University of Technology Inorganic Materials Research Program of the School of Physical and Chemical Sciences and Discipline of Chemistry, Faculty of Science and Technology is gratefully acknowledged.

Finially, I would like to express my appreciation to my wife, Yingjun Song, and my daughter, Linxiao Liu, for their support, understanding and encouragement, which gave me faith and strength to finish this work.

Chapter 1:

Introduction

1.1 BACKGROUND AND MOTIVATION

Since the discovery of carbon nanotubes[1], one-dimensional (1D) nanostructures have become an exciting, intellectually challenging, and rapidly expanding research field. Over the past several years, considerable efforts have been devoted to the synthesis of different type of 1D nanostructures such as nanowires, nanofibres, nanorods, nanobelts, and nanotubes owing to their unique performance in the fields of chemistry, physics and material science[2].

In particular, the 1D nanostructure is also important for catalysis. Recent progress in catalyst preparation highlights the design of catalytic nanoarchitectures which require the incorporation of multifunctional nanoscale building blocks into an integrated edifice. This new research direction underlines the importance of pore volume and the unimportance of periodic porosity for a catalyst, since in most cases the periodic porosity presents a one dimensional pore channel where any blockage by small nanoparticles or coke will shut off a small section of pipe from reacting[3].

Materials with 1D nanostructure should be preferential building blocks for fabricating architectural catalysts, because they can be easily assembled into macroporous frameworks with large void spaces, through which the diffusion of reactants and products can be significantly enhanced, thereby increasing the catalytic activity of the catalyst.

Wet chemical processes such as hydrothermal or solvethermal methods can be used to prepare large quantities of the 1D nanomaterials with excellent reproducibility[4]. Nevertheless, one major hurdle that obstructs these materials from catalytic application is their constituent unicity prepared by wet chemical processes. In catalytic applications, multifunctionality is obligatory. High performance catalysts usually need a combination of multiple components to achieve specific surface functionality, and provide a favourable structure to facilitate mass transport of reactant as well as resist coking. Therefore, the preparation of complex

functional 1D nanomaterials with controlled size and morphology, such as core/shell, nanowires and nanobelts heterostructures and superlattices, are highly desirable[5]. The resultant nanocomposites, containing more than one type of component, may display higher complexity and a wider range of properties. These properties are not only derived from the simple addition of properties of parent constituents but also result from their morphology and interfacial characteristics[6-8].

Therefore, to further develop 1D alumina into commercially viable, functional materials, we synthesised ZrO_2 - Al_2O_3 and TiO_2 - Al_2O_3 1D nanocomposites by incorporating ZrO_2 and TiO_2 nanocrystallites on alumina nanofibres with an extremely large loading ratio (Zr or Ti/Al molar ratio can be prepared to 2:1), producing a core-shell structure. By taking advantage of their unique textural properties, the 1D nanocomposite can be easily aggregated into a macroporous framework, of which the surface properties are very close to the pristine ZrO_2 and TiO_2, while the surface area is significantly larger. Furthermore, in this work, these materials were developed into viable catalysts and their activities tested.

In this thesis, only titanium dioxide and zirconium dioxide were chosen to demonstrate our invented strategy for synthesis of fibrous nanocomposite as they are widely used in many application fields: Titanium dioxide is well known for its utilization in solar energy conversion and hazardous waste remediation, whereas zirconium dioxide is becoming increasingly important in the field of catalysis. Starting with their alkoxide precursor, both metal oxides can be deposited onto the frameworks of aluminium nanofibres by a modified sol-gel process. This determined that not only the ZrO_2 - Al_2O_3 and TiO_2 - Al_2O_3 1D nanocomposites can be prepared, and in the future we can construct fibrous nanocomposites of other metal oxide from their corresponding alkoxide precursor.

1.2 THE AIMS OF THIS THESIS

The primary objective of this project is the synthesis and characterisation of nanocomposite materials based on boehmite nanofibres, and an exploration of their applications in catalysis.

1) To controllably incorporate some transition metal nanocrystallites, such as tetragonal zirconia, anatase TiO_2, on the outer surface of alumina nanofibres, and further fabricate fibrous nanocomposites with core-shell structures.

2) To systematically characterise the structure and properties of nanocomposite materials with specific core-shell structures.

3) To investigate the applicability of the 1D nanocomposite catalysts and develop some industrially important organic reactions in which the 1D nanocomposite catalysts show much higher activity than conventional catalysts (without 1D structure).

4) To illustrate morphological effects on the catalytic performance for a 1D (fibrous) catalyst with core-shell structure.

1.3 ACCOUNT OF SCIENTIFC PROGRESS

In this thesis, unique 1D nanocomposites with core-shell structure were synthesised from highly dispersed bundles of boehmite (AlOOH) nanofibres that act as a hard template. Meanwhile, we proposed that the macroporous frameworks can be readily fabricated from these fibrous materials.

In the previous literature, macroporous frameworks have been synthesised by two strategies, the first uses expensive organic templates, such as latex spheres or block-copolymers, which produce ordered networks usually unnecessary for the most catalytic reactions. The second is to combine sol-gel methods with a complicated drying technique,

such as freeze-drying or supercritical drying. Both strategies involve complex procedures, which makes them unsuitable for scaling-up to practical applications.

With the proposed approach, there is no need to use any organic templates, and the macroporous material is supported by a robust skeleton, which is formed by inter-connected boehmite nanofibres and then enhanced by the amorphous shell of transition metal oxide. Additionally, there is no need to conserve a network of wet-product during the drying step, and no complicated drying technology is necessary. Moreover, the core-shell structure allows the materials to take on extremely large supporting ratios which ensure that the surface properties will not be compromised by the interaction with their alumina core after calcination.

We developed the nanocomposites into a functional catalyst, and during investigation of their catalytic performances, we were specifically interested in the morphology-performance relationship of the hierarchical catalyst. We demonstrate that the surface properties of our synthesised nanocomposites were close to their pristine counterpart and the fibrous morphology is particularly important for a high efficient photocatalyst. Moreover, a catalyst with such morphology can be more easily recovered from solution by traditional filtration methodology compared to spherical-nanoparticles catalyst. We expect that our work could be comlementary to existing techniques for the new rising field of catalytic nanoarchitectures.

1.4 THESIS OUTLINE

This thesis is organised into seven chapters: the next chapter (Chapter 2) is a review of the literature investigating boehmite (AlOOH) or alumina (Al_2O_3) nanofibres on their synthesis and applications. Chapter 3 introduces the synthesis and characterisation of macro-mesoporous zirconia-alumina materials with a 1D hierarchical structure and discusses its synthetic mechanism. Chapter 4 describes how these nanocomposites were developed into a series of solid superacids and their catalytic performances tested. In Chapter 5, based on the synthetic mechanism for macro-mesoporous zirconia-alumina materials, a novel approach

for synthesis of macro-mesoporous titania-alumina materials was developed and the surface properties of these materials were investigated. In the following chapter, these titania-alumina materials were prepared into photocatalysts, and the morphological effects were evaluated in this chapter. The final chapter concluded our works and highlighted the contributions.

1.5 REFERENCES

(1) Lijima, S. *Nature* **1991**, *354*, 56.

(2) Xia, Y.; Yang, P.; Sun, Y.; Wu, Y.; Mayer, B.; Gates, B.; Yin, Y.; Kim, F.; Yan, H. *Adv. Mater.* **2003**, *15*, 353.

(3) Rolison, D. R. *Science* **2003**, *299*, 1698.

(4) Armstrong, A. R.; Armstrong, G.; Canales, J.; Bruce, P. G. *Angew. Chem., Int. Ed.* **2004**, *43*, 2286.

(5) Nagashima, K.; Yanagida, T.; Tanaka, H.; Seki, S.; Saeki, A.; Tagawa, S.; Kawai, T. *J. Am. Chem. Soc.* **2008**, *130*, 5378.

(6) Lee, M. C.; Choi, W. *J. Phys. Chem. B* **2002**, *106*, 11818.

(7) Soriano, L.; Fuentes, G. G.; Quiros, C.; Trigo, J. F.; Sanz, J. M. *Langmuir* **2000**, *16*, 7066.

(8) Sanchez-Agudo, M.; Soriano, L.; Quiros, C.; Abbate, M.; Roca, L.; Avila, J.; Sanz, J. M. *Langmuir* **2001**, *17*, 7339.

Chapter 2:

Literature Review

Recently, the synthesis and application of one-dimensional (1D) nanomaterials including nanofibres, nanowires, nanotubes, etc., has attracted intense attention in the literature. Many kinds of 1D inorganic nanomaterials have been successfully synthesised which include titanate nanofibres[1], CeO_2 nanowires[2], $Cd(OH)_2$ nanowires[3], MnO_2 nanowires[4], *etc.* The distinctive geometric characteristics of these nanomaterials may lead to novel physical and chemical properties, which are not achieved by their bulk analogues.

Amongst the 1D nanomaterials, boehmite (AlOOH) nanofibres have drawn noteworthy attention. This is because it can undergo a phase transformation to γ-Al_2O_3 nanofibres without a distinct morphological change through a simple dehydration process at approximately 673 K. γ-Al_2O_3 is one of the most industrially important oxides with uses in advanced catalysis, adsorption, composite materials and advanced ceramics[5-9]. Studies utilising γ-Al_2O_3 nanofibres instead of traditional particulate γ-Al_2O_3 are of tremendous interest for both fundamental research and technological application, with some of these studies concluding that nanocomposites synthesised with alumina nanofibres have superior properties due to their unique morphology[10-17].

This chapter reviews the current state of research and focuses on the synthesis of boehmite nanofibres and their nanocomposites. This chapter is organised into five sections: Section 2.1 introduces different synthetic conditions currently utilised when making boehmite nanofibres, which results in the formation of various aspect ratios and surface areas of boehmite nanofibres. Section 2.2 briefly introduces some of the formation mechanisms relevant to those proposed by authors to account for the morphology. Section 2.3 highlights a range of unique properties that AlOOH nanofibres and their dehydrated counterparts (γ-Al_2O_3 nanofibres) possess. Section 2.4 focuses on the modification of boehmite nanofibres and

Al_2O_3 nanofibres to produce functional nanocomposites. Finally, Section 2.5 provides a summary of alumina nanofibre research and along with a personal perspective.

2.1 PREPARATION OF BOEHMITE NANOFIBRES IN VARIOUS SYNTHETIC SYSTEMS

Alumina nanofibres can be synthesised by many methods including the hydrothermal method[18], anodic oxidation of high-purity aluminium[19,20], flame aerosol synthesis[21], etching of a porous alumina membrane template[22], electrospinning[23] or even the pyrolysis of aluminium oxyhydride at 800-1000^{o}C[24]. These methods differ in their difficulty, cost, feasibility and environmental impact. Among these methods, the hydrothermal treatment is the simplest, and it is also reliable and scaleable[25].

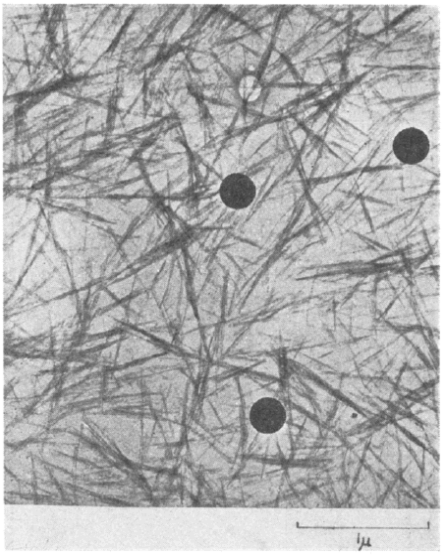

Figure 1. Boehmite nanofibres synthesised by Bugosh. (Image from Reference 18)

The first synthesis of alumina nanofibres by hydrothermal treatment was reported by John Bugosh in 1961[18]. Bugosh firstly prepared the aluminium chlorohydrate as precursor by the addition of Al powder to an aqueous solution of $AlCl_3$ to achieve an Al/Cl ratio of 2/3. Such a mixture was then diluted and hydrothermally treated at 160^{o}C for 40 h to prepare boehmite (AlOOH) nanofibres. In Bugosh's work, γ-alumina nanofibres were subsequently prepared by the dehydration of boehmite nanofibres above 500 ^{o}C[26]. To the best of the author's

knowledge, alumina nanofibres were not further investigated until 1990, when Buinning and co-workers investigated the effect of hydrothermal temperatures from 140 ^{o}C to 220 ^{o}C on the synthesis of boehmite nanofibres using Bugosh's method. It was found in a study by Buinning *et al.* [27]that fibrous boehmite could be obtained in the hydrothermal temperature range of 140 to 160 ^{o}C, while fully crystalline platelike boehmite particles approximately 260 nm long, 95 nm broad, and 14 nm thick were obtained at 220 ^{o}C. In addition to their findings, Buinning's group also modified the synthetic method. This modified method used an acidified aqueous solution to react with aluminium alkoxides, which replaced the alumina precursor used in Bugosh's method – basic aluminium chlorohydrate – with further hythermal treatment at 150 ^{o}C. Two aluminium alkoxides, aluminium tri-sec-butoxide and aluminium isopropoxide were used in the Buinning study. The authors showed that the average fibre length could be varied from 100 nm to 500 nm by controlling the concentration of aluminium alkoxide and HCl[28].

In more recent years, the hydrothermal process has been modified and used by many research groups to prepare boehmite nanofibres. The use of a surfactant to assist the nucleation process has proved to be an effective approach to control the size and morphology of final products. Kuang and co-workers[29] used $AlCl_3 \bullet 6H_2O$ as an alumina precursor but added the cationic surfactant (cetyl trimethylammonium bromide, CTAB) into a hydrothermal system in a method similar to the Bugosh method. Kuang claimed the finial products were boehmite nanotubes, which had a 30~ 70 nm outer diameter with wall thicknesses of 5~ 6 nm. Although nanotube structure was observed by transmission electron microscopy (TEM), uniform mesoporosity of the nanotube morphology was not detected by other characterisation techniques. In addition, the surface area was relatively low (about 137.5 m^2/g) which does not exhibit superiority to that of alumina nanofibres[30,31].

Valtchev and co-workers[30] added the surfactant, sodium polyacrylate (NaPa) 2100 in a 0.1M aqueous solution of aluminium chloride. In this system the sodium polyacrylate (NaPa) 2100 was employed as a size-/morphology-controlling agent. They found that a stable

colloidal suspension of round boehmite nanoparticles of sizes between 15 nm and 40 nm was obtained when hydrothermally treated at 160 °C for 1 day. When the synthesis time was increased from 24 to 168 h the product was boehmite fibers, 1000~ 2000 nm long and about 10 nm wide. The surface areas of these materials were about 103 ~ 155 $m^2 g^{-1}$.

Zhu and co-workers reported[13] an interesting new synthesis method using neutral surfactant to direct the formation of Al_2O_3 nanofibres. With the assistance of a non-ionic poly ethylene oxide (PEO), the particles were assembled into nanofibres. The synthetic procedure started from the addition of $NaAlO_2$ solution into an acetic acid solution to prepare an aluminium hydrate. The resulting white precipitate was separated by centrifugation and washed to remove sodium acetate. The washed precipitate was then mixed with PEO surfactant at a desired molar ratio of surfactant to hydrate. After hydrothermally treating the mixture at 373 K for 48 h, the hydrate was transformed into alumina nanofibres which are about 30~ 60 nm long and 3~ 4 nm thick with the surface area of resultant nanofibres being about 376 $m^2 g^{-1}$. Zhu *et al*. also demonstrated that the growth of the nanofibres could be improved by the regular supply of fresh precipitate. Under these conditions, the nanofibres could grow to over 100 nm long, as long as the reaction conditions were well-controlled[32].

Besides the surfactant-aided strategy, Shen *et al*.[31] recently reported that 1D nanostructures of Al_2O_3 can be prepared by a steam-assisted solid-phase conversion of an amorphous aluminium hydroxide wet-gel, without the use of surfactants or solvents. In Shen's work, the aluminium precursor solution was prepared via dropwise addition of an ammonium hydroxide solution to an aluminium nitrate solution under stirring to achieve a pH of 5. Instead of hydrothermally treating the aluminium precursor solution, Shen and co-workers filtered off the amorphous aluminium hydroxide precipitate and heated the wet precipitate in a hydrothermal bomb to create steam environment. Under these conditions the resulting solid, cakelike, wet-gel converted into an 1D alumina nanostructure, with average lengths of 100~400 nm and uniform diameter of about 20~30 nm. The advantage of Shen's method is

that the yield of boehmite nanofibres can be remarkably improved due to the removal of excess water.

Boehmite nanofibres have also been synthesised in the presence of room-temperature ionic liquids (RTILs) such as 1-hexadecyl-3-methylimidazolium chloride (C_{16}MimCl)[33]. Generally, to induce the formation of boehmite nanofibres, an aluminum precursor solution needs to undergo a hydrothermal treatment at more than 120^{o}C for 2 days, and autoclave is necessary to conduct the procedure. The use of RTILs eliminates the complications associating with high hydrothermal pressures, and the reaction can be conducted in an open container due to the decreased vapour pressure of the solvent.

In summary, these results show that the synthesis of boehmite nanofibres can be realised in many synthetic systems. The aluminium precursor is usually an acidic aluminium source, such as $AlCl_3$, $Al(NO_3)_3$ or acidified aluminium alkoxide. Kaya and co-workers initially reported that the initial pH value strongly affects the final morphology of boehmite colloid. Boehmite nanofibres crystallised under acidic conditions of between pH 2 to pH 5, and platelike crystallites were obtained at a pH of 10[34]. Zhu *et al.*[35] demonstrated that under the assistance of surfactant (PEO), nanofibres were formed under acidic conditions, while at neutral or high pH values, porous plates of several nanometers thick were obtained. For the steam-assisted solid-phase conversion[31], Shen *et al.* also found that boehmite nanofibres were obtained from the wet-cake precipitated at a pH from 5.0 to 7.0, whereas irregular boehmite particles were obtained if wet-cake was precipitated at pH higher than 10.0. Although, this principle may not be applicable for all synthetic systems, it is at least indicated that weakly acid medium favours the formation of boehmite nanofibres.

2.2 THE FORMATION MECHANISM OF BOEHMITE NANOFIBRES

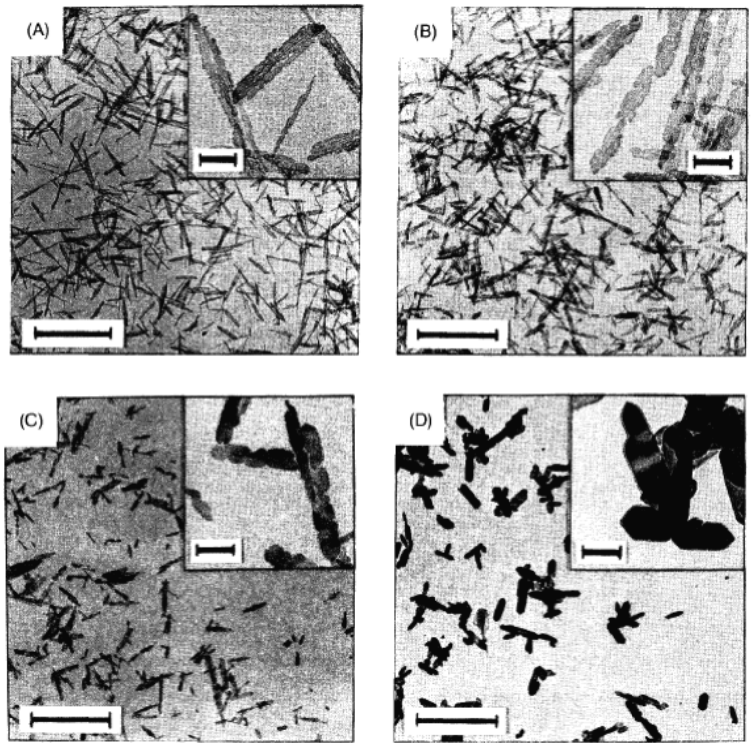

Figure 2. The Morphology of boehmite nanofibres synthesised at various temperatures A) 155°C B) 175°C C) 190°C and D) 220°C (Image from Reference 27.)

In 1990, Buining *et al.*[27] investigated the effect of hydrothermal temperature and Al_2O_3 to Cl^- molar ratio on the morphology of boehmite nanofibres synthesised by the Bugosh method. They observed by TEM that the boehmite nanofibres synthesised at 155°C were built up of very small co-oriented crystallites which were about 40 nm long, 10 nm broad and 8 nm thick. The length of boehmite nanofibres depended on the number of crystallite units. Because the boehmite unit becomes bigger and more crystalline at elevated temperatures, the average width of boehmite naonofibres is also correlated to the synthetic temperature. From Buining's work, it is now known that the boehmite nanofibres consisted of a number of boehmite nanocrystals with hexagonal shapes oriented along the fibre axis.

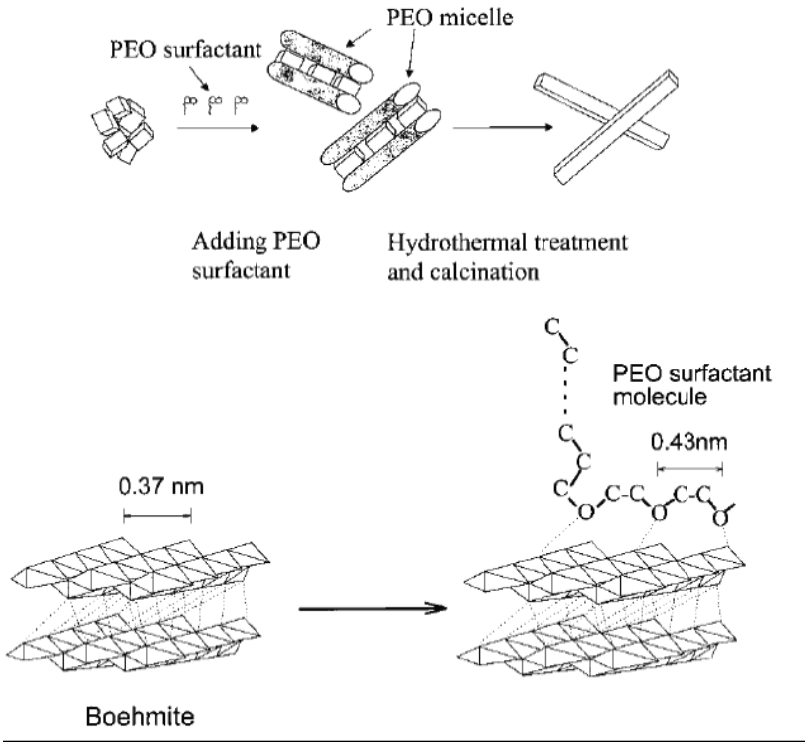

Figure 3. Schematic illustration of the surfactant-induced fiber formation change mechanism. (Image from Reference 13.)

In Zhu's work[13], boehmite nanofibres were synthesised in the presence of an organic surfactant. The authors proposed a surfactant-induced fibre formation process (Figure 3) where the PEO surfactant aggregated into micelles formation that possesses a one-dimensional structure. The growth of boehmite nanocrystals was then regulated by the micelles which strongly bind to the surface of boehmite. This allowed the boehmite crystallites to only grow along the 1D axis of the micelle to form boehmite nanofibres. Their mechanism demonstrates the oriented stacking of boehmite nanocrystallite under a specific condition, but fails to explain why the boehmite nanofibres can also be fabricated without surfactant assistance.

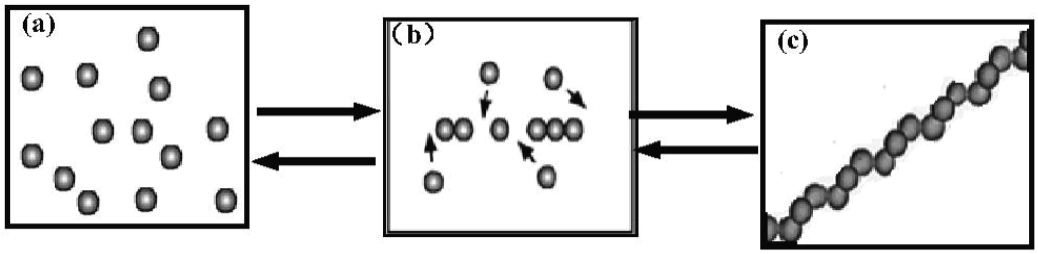

Figure 4. Schematic illustration of a potential mechanism for the assembly and disassembly of boehmite nanofibres (a) Hydrolysis of aluminium alkoxide generates amorphous alumina hydrate gels. (b) When the solution is heated, boehmite nanocrystallites are formed at the expense of amorphous alumina hydrate gels and assembly in liquid phase. (c) Boehmite nanofibers continue to grow. (Image from Reference 36.)

Ning and co-workers[36] observed two opposite shape transformation processes in the synthesis of boehmite nanofibres. In the liquid phase, the boehmite nanofibres can spontaneously "grow" by the assembly of numerous nanosphere building blocks which are generated by the hydrolysis of aluminium alkoxide,this procedure was carried out without the aid of surfactant. Furthermore, these nanofibers can disassemble into nanospheres under electron beam bombardment *in-vacuo,* found in TEM. Base on this observation, Ning *et al.* proposed that the growth of boehmite nanofibers follows a preferential growth mechanism (Figure 4.), and the preferential growth direction is responsible for the nature of the boehmite crystal structure. However, the Ning *et al*. could not provide further structural information to prove their observations.

Recently, Xiang *et al.*[37] studied the hydrothermal treatment of $Al(OH)_3$ gel in sulphate solutions and found the aspect ratio of the boehmite nanofibres increased to 300 as the initial H_2SO_4 concentration increased to 0.043 mol•L^{-1}. The mechanism of preferential growth along the [100] direction was proposed as follows.

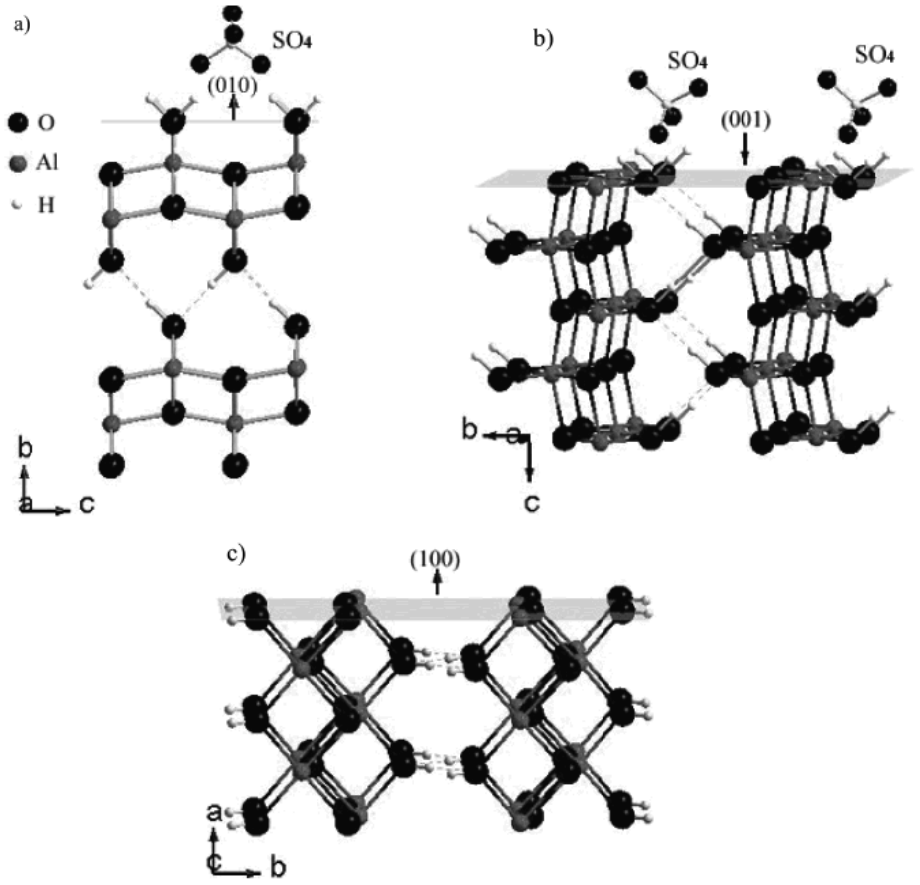

Figure 5. Boehmite structure and the possible adsorption configuration of sulfate on the (010) plane (a) and (001) plane, no adsorption on (100) plane (c). (Image from Reference 37.)

In the boehmite structure (Figure 5), each Al is surrounded by four O atoms and two OH groups to form $AlO_4(OH)_2$ octahedra. These $AlO_4(OH)_2$ octahedra are linked to each other by sharing edges, forming AlO(OH) layers parallel the (010) plane. AlO(OH) layers are bonded with each other via a H-bond interaction between OH groups. The hydroxyl group on (010) planes can also absorb SO_4^{2-} via H-bonding, which improves the stability and reduces the growth rate of (010) plane (Figure 5a). The growth of the (001) plane may also be inhibited by the adsorption of SO_4^{2-} with the OH group on the (001) plane (Figure 5b). The (100) planes are however linked by Al-O bonds (Figure 5c), making the adsorption of SO_4^{2-} on this plane difficult; therefore the boehmite nanofibres preferentially grow along this crystal axis.

2.3 THE UNIQUE PROPERTIES OF BOEHMITE AND ALUMINA NANOFIBRES

With its importance as a catalyst and catalytic support in chemical industry[5], even a small improvement to alumina properties is commercially significant. The usefulness of this material can be traced to the favourable combination of its textual properties, including surface area, pore size and pore volume with its chemical properties. In the literature, the properties of alumina nanofibres are usually discussed as follows.

DISPERSIBILITY OF BOEHMITE NANOFIBRES

Boehmite nanofibres can be highly dispersed into aqueous solutions where a self-sustaining gel is formed when the particle volume fractions are below 1%. The stability of this gel-like structure in aqueous solution was dependant on the aspect ratio of boehmite nanofibres[38]. Samples with a higher aspect ratio can retain a longer period of stability and possess higher gel strength. In addition, the stability of the dispersion was also found to vary with the salt concentration and particle volume fraction. At low salt concentrations, the particle-particle interactions are dominated by repulsion and after about 1 month, a separation of isotropic upper phase and ordered nematic lower phase can be observed for long nanofibres with an aspect ratio of about 20. This phenomenon of ordered arrangement arises when the nanofibres take up a more or less parallel orientation, and the loss of orientation entropy is compensated by a decrease in "excluded volume[39]". Above a critical salt concentration, the phase behaviours are mainly governed by the attractive interactions[40]. Under these circumstances a space-filling amorphous gel is formed irrespective of particle length of boehmite nanofibre[38].

Generally, the length of boehmite nanofibres presents as a distribution with the longest fibres being 2 to 3 times longer than the shortest ones. Because of this nonhomogeneity of the nanofibres' particle size, mass and other characteristics, the dispersion measured by gel strength, may exhibit a peculiar dependence on salt concentration. An example of this is shown in Philipse's work[41], where the gel strength was decreased by the addition of LiCl below 10mM. Reduction in gel strength was attributed to the compression of the electrified

double layer, which reduced the entanglement of boehmite nanofibres. However, when the concentration of LiCl was in the range from 10mM to 75mM, the gel strength is increased due to the formation of a skeleton of flocculated particles. With the further increase of LiCl concentration, the gel strength was reduced again due to the formation of more flocculated particles. These experimental measurements were schematically illustrated, as in Figure 6.

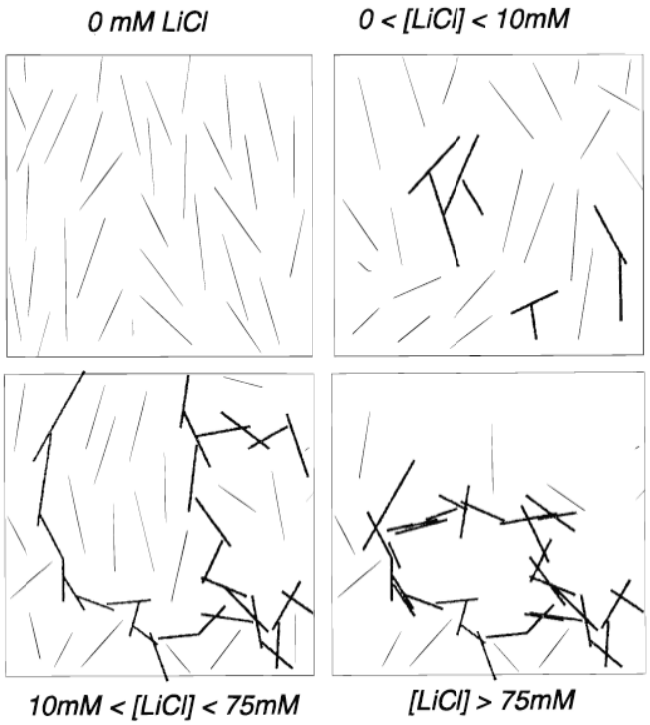

Figure 6. Schematic drawing of the particle structure in the dispersions of boehmite nanofibres with different LiCl concentrations (Image from Reference 41.)

LARGE PORE SIZE AND PORE VOLUME

The large pore size and pore volume are one of the important properties of alumina nanofibres, which is attributed to the inter-fibrous voids of the randomly stacked alumina nanofibres[13]. In the literature, (Figure 7) the N_2 adsorption-desorption measurements shows non-reversible adsorption-desorption isotherms[13,42-44] which can be attributed to the a type IV isotherm. The hysteresis loop, which is associated with capillary condensation, falls within the H3 and H4 categories[43]. This kind of hysteresis loop is observed for slit-shaped pores generated from the aggregates of plate-like particles[45]. Nevertheless, the pore size of alumina

nanofibres exhibited an extremely broad distribution, presumably because the pore-structure resulting from the randomly stacking of fibrous nanoparticles are close to a three-dimensional network, and do not possess regular shapes or size[13].

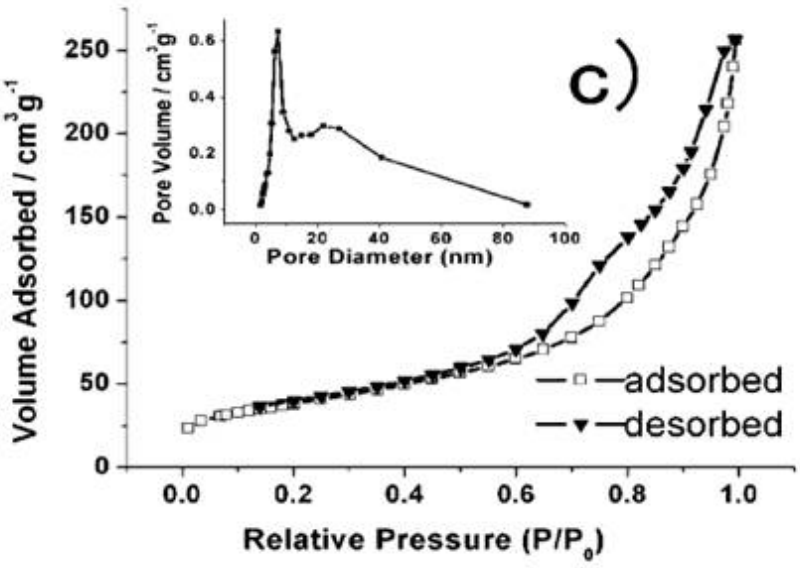

Figure 7. N_2 absorption and desorption isotherms and pore-size distributions (insets) for the boehmite nanofibres (Image from Reference 42.)

The textural properties of alumina nanofibres are different to that of bulk alumina. Martinez and co-workers used alumina nanofibres as a support for Co-based Fischer-Tropsch catalysts. After comparing the texture structure of alumina nanofibres with commercial γ-Al_2O_3 (Table 1.), the authors believed that, for the commercial alumina, the surface area and pore size were not independent parameters and that any increase in surface area is inevitably accompanied by a decrease in the mean pore size. Alumina nanofibres on the other hand simultaneously display both a very high surface area and a large pore size[43].

Table 1. Origin and textural properties of the γ-alumina supports

Support	Origin	N_2 physisorption			Hg intrusion PV[c] (cm^3/g)	Crystal size (nm)
		B.E.T.(m^2/g)	PD[a] (nm)	PV[b] (cm^3/g)		
Al_2O_3_1	Catapal-B (Sasol)	254	6.0	0.48	—	3.9
Al_2O_3_2	Pural-SB (Sasol)	192	9.1	0.55	0.04	4.2
Al_2O_3_3	Puralox TH100/150 (Sasol)	157	21.8	0.98	0.09	7.0
Al_2O_3_4	Catalox HTa101 (Sasol)	70	32.4	0.65	0.11	8.5
Al_2O_3_nf	Nanofibrous Al_2O_3	321	16.1	1.29	0.26	3.5

[a] Mean pore diameter estimated from the absorption branch of the isotherm by applying the B.J.H. formalism

[b] Total Pore diameter

[c] Total pore volume for pores in the range of 50-103 nm diameter as determined by Hg intrusion porosimetry

However, it is worth mentioning here that alumina nanfibres also obeyed the inverse relationship between pore size and surface area in a similar fashion as the normal support. Gevert and co-workers[46,47] synthesised three different alumina nanofiber batches by varying the hydrothermal temperatures. The increase of hydrothermal temperatures led to an increase in size of the fibrous particles, therefore the surface areas of these three alumina nanofibres gradually decreased with a simultaneous increase of average pore size. The direct comparison of the the textural properties of alumina nanofibres and traditional corpuscular alumina led the authors to conclude that alumina nanofibres have a large surface area for a given average pore diameter or a larger average pore diameter at a given specific surface area (Table 2.).

Table 2. Textural properties of 3 kinds of γ-alumina nanofibres

Carrier produced at temperature	145 °C	160 °C	180 °C
Surface area (m^2g^{-1})	244	176	150
Pore volume [a] (mlg^{-1})	0.79	1.12	1.00
Average Pore diameter[b] (nm)	13.0	25.4	26.7

[a] Estimated as the liquid volume adsorbed at a relative pressure of 0.995.

[b] Calculating assuming cylindrical pores

THERMAL STABILITY

It is reported by many authors[13,48] that γ-Al_2O_3 with fibrous morphology also retains a large surface area after calcination at a temperature of about 1473K. Shen and co-workers[16] investigated the effect of thermal treatment on the surface areas of alumina nanofibres and alumina nanopowders. The comparison commenced at 600°C and the surface areas of two materials are very close, with 201 m^2/g for nanofibres and 185 m^2/g for nanopowder. The surface areas for both materials decreased with increasing of the calcination temperature. However, the surface areas of alumina nanopowder exhibited a remarkable shrinkage at higher temperatures. At 1473K, the surface area for alumina nanofibres was still 133 $m^2 \cdot g^{-1}$ while the surface area of alumina nanopowder shrank to 6.2 $m^2 g^{-1}$. At 1573 K, the surface area of alumina nanopowder shrank to 0.89 $m^2 g^{-1}$ but that of alumina nanofibres was still 68 $m^2 g^{-1}$.

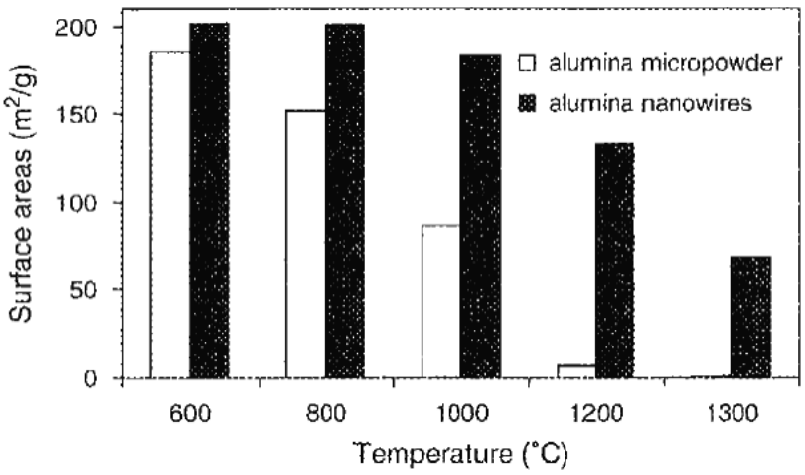

Figure 8. Effect of thermal treatment on surface areas of (■) Al_2O_3 nanofibres and (□) Al_2O_3 nanopowder. (Image from Reference 16.)

This reduction in surface area was attributed to the fact that γ-Al_2O_3 is at a metastable phase and will transform into α-Al_2O_3 at temperatures above 1000°C. This phase change is accompanied by remarkable particle growth, leading to a catastrophic loss of specific surface area and a change in surface chemistry. The particle growth proceeds through atomic diffusion from smaller particles to large particles via their contact region. Alumina with fibrous morphology can be aggregated so it may have a low bulk density, and in this case, the contact area of primary particles is dramatically minimized, and therefore the surface diffusion is kinetically suppressed. Consequently, alumina nanofibres can keep a larger surface area than traditional alumina supports at elevated temperature. Tatsuro Horiuchi *et al.* demonstrated[49] that fibrous alumina with a bulk density of 1.1 g cm^{-3} transferred into α-phase at 1443K, while the phase transition for alumina with a lower bulk density of 0.06 g cm^{-3} occurred at 1573K. After heating at 1473K for 5 h, the latter fibrous alumina also retained a large surface area of 90 $m^2 g^{-1}$.

The thermal stabilities of alumina nanofibres with different lengths exhibited a different story. Khalil[50] synthesised long alumina (about 200 nm) and short alumina nanofibres (about 50 nm) via the hydrolysis of aluminium alkoxide at slow and high stirring rates. The

comparison of thermal stability between these two kinds of nanofibres showed that the short nanofibres are more thermally resistant than the long alumina nanofibres. Although different textural structures are derived from the length of nanofibrs, the author speculated that the different thermal stability is due to the low concentration of OH anions on the surface of the short fibers when compared to the longer ones, since the surface/mass ratio is larger for the short nanofibres.

2.4 NANOCOMPOSITE BASED ON ALUMINA NANOFIBRES AND THEIR APPLICATIONS

The synthesis of alumina nanofibres has been studied extensively due to their interesting one-dimensional morphology and resultant unique properties. However, for real applications, these materials need to be further functionalised via various methods in order to fabricate specific nanocomposites. Reports dedicated to the synthesis and application of alumina nanofibre-based nanocomposites are not numerous but are being increasingly reported.

SYNTHESIS OF NANOCOMPOSITES

Coating a layer of silica onto colloidal materials to form a core-shell structure is a widely used strategy to improve the stability of colloidal particles from coalescence. Philipse and co-workers[11], using boehmite nanofibres as a template, controlled the growth of silica onto boehmite nanofibres using an aqueous sodium silicate solution. Philipse's method was able to avoid the formation of silica particles and also allowed a subsequent grafting with silanes or octadecyl alcohol. The grafted 1D nanocomposites resulting from the process have a dense alkane layer on their surface, which screens the van der Waals attractions rendering them more stable in liquid solutions. The presence of translucent sediments in their experiments illustrated the suppression of turbidity by interparticle interactions.

A more reproducible method for coating silica onto the surface of boehmite nanofibres was reported by Graf *et al.*[51]. Graf *et al*. firstly stabilised the boehmite nanofibres by adsorbing a layer of poly(vinylpyrrolidone) (PVP) as a coupling agent. After stabilisation, the material was directly transferred into an ammonia/ethanol mixture where a smooth and

homogeneous silica layer was grown with variable thickness by the addition of tetraethoxysilane (TEOS).

In addition, for the preparation of 1D alumina nanocomposite, Frost[52] *et al.* further developed the methodology previously used in the synthesis of boehmite nanofibres[13]. Their synthetic strategy can be summarised as follows: transition metal ions are added into an aluminium solution at the beginning, and a homogeneous co-precipitate was prepared via the addition of NaOH solution as precipitating agent. The resultant co-precipitate, a metal-aluminium hydrate was transformed into a 1D alumina nanocomposite in the subsequent preparation stages in the same manner as that 1D alumina is prepared from pristine alumina hydrate. An example of this strategy is Zhao *et al.*'s[52] preparation of iron-doped boehmite nanofibres synthesised at low temperatures using a modified poly (ethylene oxide) surfactant-induced fibre formation method (SIFF)[13]. In this example a series of iron-doped boehmite nanofibres with varying iron contents was systematically studied. TEM images showed that when the doped iron content was less than 5%, the resulting nanostructures were predominantly nanofibres; in contrast, when iron doping was above 4%, nanosheets were formed, and nanotubes and iron-rich particles can be observed in samples with 20% added iron. These materials were analysed by thermogravimetric and differential thermogravimetric methods. From the observation for both the temperature of the loss of interstitial water and the dehydroxylation, the iron doped boehmite nanofibres are more thermally stable than undoped boehmite[53].

Besides iron-doped boehmite nanofibres, the 1D Ga-doped boehmite nanocomposites have also been synthesised in the Frost group via the same methodology[54]. In their study, Ga-doped boehmite nanotubes were synthesised when added Ga molar percentage was less than 5%, whereas a mixture of nanosheets, nanotubes and nanoribbons were formed when the Ga content was increased between 5% and 10%.

Moreover, they also synthesised yttrium doped boehmite nanofibres with varying yttrium content[55]. All samples with low doped Y% proved to be nanofibres, whereas at high doped Y%, large crystals of yttrium hydroxide were formed with nanofibres. When investigating the influence of hydrothermal temperature, a second Y rich phase was observed to occur at much higher temperature, which indicated that higher hydrothermal temperature readily results in the lowered substitution of yttrium into the boehmite nanocrystallites.

In summation, it seems the exact morphology of nanostructures synthesised by modified SIFF methods are dependent on the amount of added doping metal ions. The nanofibre morphology is normally maintained when the molar ratio of doping metal to aluminium is below 5%. The Frost group's work provides a fundamental and comprehensive understanding of the growth of metal doped boehmite nanostructures, which is valuable for future studies on the manipulation and control of properties for applications of boehmite/alumina nanostructures.

Further to this work, recently Frost *et al.*[56] synthesised chromium doped boehmite nanofibres by modifying the so-called steam assisted wet-gel conversion process[16]. The as-synthesised nanocomposites were characterised by thermogravimetric analysis. Again, doping with chromium resulted in an increase in the thermal stability as seen by the dehydroxylation temperature of boehmite increasing from ~406.5 to 436.5^{o}C.

More importantly, their experiments demonstrate that their synthetic method is a versatile strategy that may be extended to various synthesis procedures in order to prepare 1D alumina nanocomposites.

APPLICATIONS OF NANOCOMPOSITES

Besides the synthesis of 1D alumina nanocomposites, the applications of 1D alumina nanocomposites are also an intriguing and intellectually challenging research field. Kawi and co-workers[14] synthesised novel nanostructured and rod-like thermally stable spinel Zn-Al complex oxide by doping boehmite nanofibres with Zn ion. In this case, the one dimensional

nanocomposites generated were well dispersed and randomly piled together, with a clear nanorod shape. These structures were not sintered together even after being calcined at a high temperature (up to 900^{o}C). The as-synthesised composite material subsequently was evaluated as environmentally friendly catalyst for the catalytic reduction of NO. The superior catalytic activity and selectivity of this catalyst was attributed to the much smaller particle size and correspondingly larger surface areas resulting from its superior thermal stability. The report by Kawi *et al*.[57] demonstrates that the thermal stability of nanomaterials can be dramatically increased by doping metal ions or metal oxides in to the structure. In addition, Iler[10] reported that the higher thermal stability can also be achieved by the addition of silica, which sidelines the phase conversion from γ to θ and α -Al_2O_3, by permitting the formation of an intermediate κ-phase under the high temperature calcination.

Alumina nanofibres have been used as supports for stabilizing metal cluster in various catalytic applications[12,43,58,59]. In this case, large average pore diameters decrease the resistance to interior diffusion, minimising the diffusion control of chemical reactions. Due to this reason, Cortright, Davda and Dumesic[12] used 3 wt% Pt catalyst supported on nanofibres of γ-alumina to produce hydrogen from sugars and alcohols at temperatures near 500K in a single-reactor aqueous-phase reforming process. This catalyst exhibited good performance.

As a support for active nanoparticles, the advantages of alumina nanofibres were unambiguously demonstrated by Martinez and co-workers[43], who prepared the RuCo Fischer-Tropsch catalysts using alumina nanofibres as support. By comparing alumina nanofibres with commercial alumina, Martinez *et al*. concluded the larger surface area of alumina nanofibres allowed a high dispersion of cobalt nanoparticles. Furthermore, the open, porous structure of the nanofibrous alumina enhanced the inter-pellet diffusion of carbon monoxide and hence increased access to the active sites resulting in negligible loss of activity during the initial reaction stages. Especially at high loading of active components

(RuCo), the alumina nanofibre catalyst exhibited the highest specific activity and productivity to diesel (C_{13}~C_{22} products).

It is worth mentioning here that boehmite nanofibres can also be used as catalyst support to entrap nanparticles of noble metal. Park *et al.*[60] synthesised Rh/AlO(OH) catalysts by a one-pot procedure exhibited in Scheme 1. Rhodium nanoparticles were prepared by the solvothermal treatment of $RhCl_3$ in the presence of 2-butanol and $Al(O\text{-}sec\text{-}Bu)_3$ to simultaneously entrap them into a boehmite matrix. By gelation of this mixture with water, rinsing and drying, a dark grey powder was obtained.

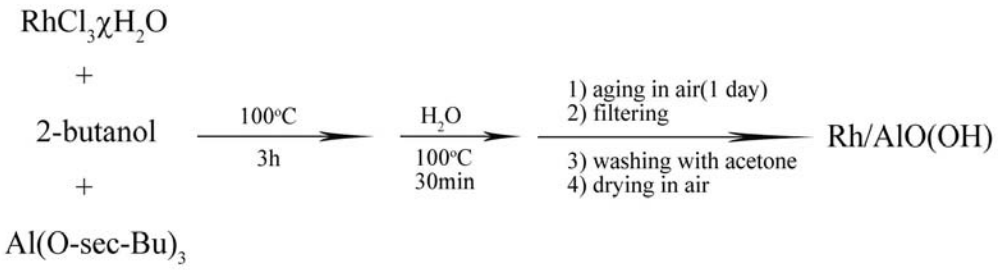

Scheme 1. Preparation of the rhodium nanoparticle catalyst

The readily prepared rhodium nanoparticles entrapped on boehmite nanofibres were used for the hydrogenation of various arenes and were sufficiently robust to recycle and are highly active, even at room temperature under 1 atm H_2.

The unique porosity of alumina nanofibres also contributes its long life-span as a catalyst. Gevert *et al.*[47] claimed that alumina nanofibres can also be used as supports in the preparation of HDM (hydrodemetallisation) and HDS (hydrodesulfurisation) catalysts used in the treatment of crude oil. The deactivation of such catalysts is usually caused by the deposition of metal sulphides at the orifice of the pores in these catalysts blocking the transport routes for reactant molecule. Owing to the combination of large surface area and a larger pore size resulting from the randomly stacked nanofibres, the catalyst showed a

constant level of hydrodemetallisation even after 500 h whereas the commercial catalyst completely deactivated after 350 h.

Alumina nanofibres are also an important precursor for building structured catalysts. Nanofibres of alumina were coated on the microsilica fibers to fabricate diesel catalytic converters, with higher soot-capturing capacity[61] due to their high resistance to the soot particulates.

Advanced adsorbents for the removal of toxic contaminants from water may also be developed from alumina nanofibres. Zhu and co-workers[17] grafted two kinds of functional groups, thiol and octyl groups, onto the surface of alumina nanofibres using silane coupling agents. The thiol groups grafted onto nanofibres were used to adsorb heavy metal ions (Pb^{2+} and Cd^{2+}) while the octyl group grafted nanofibers efficiently adsorbed organic pollutants from dilute aqueous solution. The structural advantage of nanofibres used as adsorbents may be two-fold. Firstly, the large pore size and volume can improve the accessibility of the sorption sites to the adsorbates from the bulk solution, and secondly, the large interparticle voids of nanofibres ensure that the contaminated solution flows through the sorption bed easily.

Besides the applications as catalyst and advanced adsorbent, the alumina nanofibres can also be used to fabricate ceramic membranes. Ke *et al.*[15], coated either alumina or titanate nanofibres onto a porous ceramic substrate, in order to fabricate a new kind of high-performance ceramic membrane. In this arrangement, the layer of randomly oriented alumina nanofibers acts as the separation layer. When compared with traditional ceramic membranes fabricated using the aggregated naoparticles as the separation layer, the new membrane supported a high flux while still maintaining good selectivity. The performance of the membrane was tested by filtering 60 nm latex spheres with the proposed application being to separate the pathogens, such as the common cold virus, from the blood of humans. Following this work, Ke *et al*. reported a new method[62] in which the separation layer of

ceramic membranes was fabricated in the pores of a ceramic substrate by an in situ synthesis method rather than the coating method previously used. The proposed membrane was utilised for the separation of bio-species on an industrial scale in order to illustrate its ability to effectively retain bio-molecules at relatively high fluxes.

Recently, a new filter composed by coating a layer of alumina nanofibre on a microglass fibre backbone was developed to remove microbiological agents in aqueous environments[63,64]. Its inventors claimed that the novel alumina nanofibre filter exhibited potential for removal and retention of viral aerosols. While the physical removal efficiency of the new filter was lower than conventional filters, its pressure drop was much lower due to smaller drag force produced by the nanofibre surfaces.

2.5 SUMMARY AND IMPLICATIONS

In this chapter, the synthesis of boehmite nanofibres by wet chemical methods was discussed. The earliest synthesis of this material could be traced to 1960s, and recent progress has proved that the preparation of boehmite nanofibres could be achieved in various synthetic systems, utilising various aluminum precursors. The morphology and aspect ratio of these nanofibres could be controlled by adjusting synthetic parameters including pH and temperature, or adding various surfactants.

The formation mechanism of boehmite nanofibers as previously reported by different authors was also discussed. The main formation mechanism of boehmite nanofibres is due to the preferential growth along a specific direction of boehmite nanocrystallites. This usually results from the interaction of the unique structure of the boehmite nanofibres with solvent molecules.

The chapter also discussed the interesting properties of alumina nanofibers which are (i) the excellent dispersibility in liquid solutions of their hydrate counterpart (boehmite, AlOOH), (ii) large average pore size and pore volume and (iii) high thermal stability. It was

noted that the properties of alumina nanofibre are mainly derived from the behaviour of aggregated nanofibres, which may be influenced by their preparation procedures.

The synthesis of nanocomposites based on alumina nanofibres and the application of these composites are still in an early development stage. While only a few studies exist, they clearly demonstrate the superiority of nanocomposites based on alumina nanofibers. The successful application of these materials may only be realised once they are further developed. Using alumina nanofibers as building block to fabricate complex functional materials is a challenge faced by chemists, and also provides future research opportunities to further develop advanced catalyst, adsorbent, and new ceramic materials very higher performance.

2.6 REFERENCE AND NOTES

(1) Kasuga, T.; Hiramatsu, M.; Hoson, A.; Sekino, T.; Niihara, K. *Adv. Mater.* **1999**, *11*, 1307.

(2) Tang, B.; Zhuo, L.; Ge, J.; Wang, G.; Shi, Z.; Niu, J. *Chem. Commun.* **2005**, *2005*, 3565.

(3) Tang, B.; Zhuo, L.; Ge, J.; Niu, J.; Shi, Z. *Inorg. Chem.* **2005**, *44*, 2568.

(4) Wang, X.; Li, Y. *J. Am. Chem. Soc.* **2002**, *124*, 2880.

(5) Misra, C. *Industrial Alumina Chemicals*; American Chemical Society: Washingtion, DC, 1986.

(6) Marquez-Alvarez, C.; Zilkova, N.; Perez-Pariente, J.; Cejka, J. *Catal. Rev.* **2008**, *50*, 222.

(7) Guzman-Castillo, M. L.; Lopez-Salinas, E.; Fripiat, J. J.; Sanchez-Valente, J.; Hernandez-Beltran, F.; Rodriguez-Hernandez, A.; Navarrete-Bolanos, J. *J. Catal.* **2003**, *220*, 317.

(8) Schwarz, J. A.; Contescu, C.; Contescu, A. *Chem. Rev.* **1995**, *95*, 477.

(9) Trueba, M.; Trasatti, S. P. *Eur. J. Inorg. Chem.* **2005**, *2005*, 3393.

(10) Iler, R. K. *J. Am. Ceram. Soc.* **1964**, *47*, 339.

(11) Philipse, A. P.; Nechifor, A.-M.; Patmamanoharan, C. *Langmuir* **1994**, *10*, 4451.

(12) Cortright, R. D.; Dumesic, R. R. D. J. A. *Nature* **2002**, *418*, 964.

(13) Zhu, H. Y.; Riches, J. D.; Barry, J. C. *Chem. Mater.* **2002**, *14*, 2086.

(14) Shen, S.; Hidajat, K.; Yu, L. E.; Kawi, S. *Adv. Mater.* **2004**, *16*, 541.

(15) Ke, X.; Zhu, H.; Gao, X.; Liu, J.; Zheng, Z. *Adv. Mater.* **2007**, *19*, 785.

(16) Shen, S. C.; Ng, W. K.; Chen, Q.; Zeng, X. T.; Chew, M. Z.; Tan, R. B. H. *J. Nanosci. Nanotechno.* **2007**, *7*, 2726.

(17) Yang, D.; Paul, B.; Xu, W.; Yuan, Y.; Liu, E.; Ke, X.; Wellard, R. M.; Guo, C.; Xu, Y.; Sun, Y.; Zhu, H. *Water Research* **2010**, *44*, 741.

(18) Bugosh, J. *J. Phys. Chem.* **1961**, *65*, 1789.

(19) Yan, Z.; Zhao, Y.; Li, X.; Li, N.; Bai, X.; Qiu, S.; Yu, W. *Mater. Lett.* **2006**, *60*, 2937.

(20) Pancholi, A.; Stoleru, V. G.; Kell, C. D. *Nanotechnology* **2007**, *18*, 215607.

(21) Guo, B.; Yim, H.; Luo, Z.-P. *J. Aerosol. Sci.* **2009**, *40*, 379.

(22) Jha, H.; Kikuchi, T.; Sakairi, M.; Takahashi, H. *Nanotechnology* **2008**, *19*, 359603.

(23) Li, D.; Xia, Y. *Adv. Mater.* **2004**, *16*, 1151.

(24) Liu, S.; Wehmschulte, R. J.; Burba, C. M. *J. Mater. Chem.* **2003**, *13*, 3107.

(25) Zhen, L.; Wang, W.-S.; Xu, C.-Y.; Shao, W.-Z.; Qin, L.-C. *Mater. Lett.* **2008**, *62*, 1740.

(26) Bugosh, J.; Bown, R. L.; McWhorter, J. R.; Sears, G. W.; Sippel, R. J. *Ind. Eng. Chem. Prod. Res. Dev.* **1962**, *1*, 157.

(27) Buining, P. A.; Pathmamanoharan, C.; Bosboom, M.; Jansen, J. B. H.; Kekkerkerker, H. N. W. *J. Am. Ceram. Soc.* **1990**, *73*, 2385.

(28) Buining, P. A.; Pathmamanoharan, C.; Jansen, J. B. H.; Kekkerkerker, H. N. W. *J. Am. Ceram. Soc.* **1991**, *74*, 1303.

(29) Kuang, D.; Fang, Y.; Liu, H.; Frommen, C.; Fenske, D. *J. Mater. Chem.* **2003**, *13*, 660.

(30) Mathieu, Y.; Lebeau, B.; Valtchev, V. *Langmuir* **2007**, *23*, 9435.

(31) Shen, S. C.; Chen, Q.; Chow, P. S.; Tan, G. H.; Zeng, X. T.; Wang, Z.; Tan, R. B. H. *J. Phys. Chem. C* **2007**, *111*, 700.

(32) Zhu, H. Y.; Gao, X. P.; Song, D. Y.; Bai, Y. Q.; Ringer, S. P.; Gao, Z.; Xi, Y. X.; Martens, W.; Riches, J. D.; Frost, R. L. *J. Phys. Chem. B* **2004**, *108*, 4245.

(33) Park, H.; Yang, S. H.; Jun, Y.-S.; Hong, W. H.; Kang, J. K. *Chem. Mater.* **2007**, *19*, 535.

(34) Kaya, C.; He, J. Y.; Gu, X.; Butler, E. G. *Microporous Mesoporous Mater.* **2002**, *54*, 37.

(35) Zhu, H. Y.; Gao, X. P.; Song, D. Y.; Ringer, S. P.; Xi, Y. X.; Frost, R. L. *Microporous Mesoporous Mater.* **2005**, *85*, 226.

(36) Gan, Z.; Ning, G.; Lin, Y.; Cong, Y. "Heat-induced Transformation between Nanospheres and Nanofibers of Boehmite"; Nano/Micro Engineered and Molecular Systems, 2006, Zhuhai.

(37) He, T.; Xiang, L.; Zhu, S. *Langmuir* **2008**, *24*, 8284.

(38) Buining, P. A.; Philipse, A. P.; Lekkerkerker, H. N. W. *Langmuir* **1994**, *10*, 2106.

(39) Excluded volume:. *In liquid state theory, the 'excluded volume' of a molecule is the volume that is inaccessible to other molecules in the system as a result of the presence of the first molecule.*

(40) Buining, P. A.; Lekkerkerker, H. N. W. *J. Phys. Chem.* **1993**, *97*, 11510.

(41) Wierenga, A.; Philipse, A. P.; Lekkerkerker, H. N. W. *Langmuir* **1998**, *14*, 55.

(42) Zhang, J.; Liu, S.; Lin, J.; Song, H.; Luo, J.; Elssfah, E. M.; Ammar, E.; Huang, Y.; Ding, X.; Gao, J.; Qi, S.; Tang, C. *J. Phys. Chem. B* **2006**, *110*, 14249.

(43) Martinez, A.; Prieto, G.; Rollan, J. *J. Catal.* **2009**, *263*, 292.

(44) Zhao, Y.; Frost, R. L.; Martens, W. N.; Zhu, H. *Langmuir* **2007**, *23*, 9850.

(45) Sing, K. S. W.; Everett, D. H.; Haul, R. A. W.; Moscou, L.; Pierotti, R. A.; Rouquerol, J.; Siemieniewska, T. *Pure & Appl. Chem.* **1985**, *57*, 603.

(46) Gevert, B. S.; Ying, Z.-s. *J. Porous. Mater.* **1999**, *6*, 63.

(47) Ying, Z.-S.; Gevert, B.; Otterstedt, J.-E.; Sterte, J. *Appl. Catal. A: General* **1997**, *153*, 69.

(48) Ishikawa, T.; Ohashi, R.; Nakabayashi, H.; Kakuta, N.; Ueno, A.; Furuta, A. *J. Catal.* **1992**, *134*, 87.

(49) Horiuchi, T.; Osaki, T.; Sugiyama, T.; Masuda, H.; Horio, M.; Suzuki, K.; Mori, T.; Sago, T. *J. Chem. Soc. Faraday Trans.* **1994**, *90*, 2573.

(50) Khahil, K. M. S. *J. Catal.* **1998**, *178*, 198.

(51) Graf, C.; Vossen, D. L. J.; Imhof, A.; Blaaderen, A. v. *Langmuir* **2003**, *19*, 6693.

(52) Zhao, Y.; Martens, W. N.; Bostrom, T. E.; Zhu, H. Y.; Forst, R. L. *Langmuir* **2007**, *23*, 2110.

(53) Zhao, Y.; Frost, R. L.; Martens, W. N.; Zhu, H. Y. *J. Therm. Anal. Calorim.* **2007**, *90*, 755.

(54) Zhao, Y.; Frost, R. L.; Martens, W. N. *J. Phys. Chem. C* **2007**, *111*, 5313.

(55) Zhao, Y.; Frost, R. L. *J. Colloid and Interface Sci.* **2008**, *326*, 289.

(56) Yang, J.; Frost, R. L.; Yuan, Y. *Thermochim Acta* **2009**, *483*, 29.

(57) Wu, N.-L.; Wang, S.-Y.; Rusakova, I. A. *Science* **1999**, *285*, 1375.

(58) Yem, H. S.; Kim, K. D.; Kim, J. N.; Choa, Y.-H.; Kim, H. T. *J. Ind. Eng. Chem.* **2007**, *13*, 644.

(59) Garcia-Dieguez, M.; Pieta, I. S.; Herrera, M. C.; Larrubia, M. A.; Alemany, L. J. *J. Catal.* **2010**, *270*, 136.

(60) Park, I. S.; Kwon, M. S.; Kim, N.; Lee, J. S.; Kang, K. Y.; Park, J. *Chem. Commun.* **2005**, *2005*, 5667.

(61) Torncrona, A.; Sterte, J.; Otterstedt, J.-E. *J. Mater. Chem.* **1995**, *5*, 121.

(62) Ke, X.; Shao, R.; Zhu, H.; Yuan, Y.; Yang, D.; Ratinac, K. R.; Gao, X. *Chem. Commun.* **2009**, *2009*, 1264.

(63) Tepper, F.; Kaledin, L. Nanosize electropositive fibrous adsorbent, 2005; Vol. US 6,838,005.

(64) Li, H.-W.; Wu, C.-Y.; Tepper, F.; Lee, J.-H.; Lee, C. N. *J. Aerosol. Sci.* **2009**, *40*, 65.

Chapter 3:

Fabrication of macro-mesoporous zirconia-alumina materials with a 1D hierarchical structure

3.1 INTRODUCTION

Inorganic metal oxides with macroporous frameworks usually possess very high relative pore volume and low apparent densities. Such materials are potentially useful in applications such as catalysis[1,2], separation technology[3] and biomaterials engineering[4-6]. For example, in macroporous catalysts the diffusion rate of small molecules can approach rates comparable to those in open medium[7], and thereby greatly improve catalytic activity due to the enhanced diffusion of reactants and products[8].

The use of organic templates, such as latex spheres or block-copolymers to control the structure of inorganic solids has proven to be a very successful strategy when fabricating such a material[9-11]. However, with these techniques there is a need to remove the organic space fillers by calcination that usually occurs in flowing air at high temperature. This results in the emission of template decomposition gases and requires a large amount of energy, which on an industrial scale, may restrict its application due to stringent emissions regulations and financial constraints. The high temperature required to remove the template may also cause structural collapse due to phase transformation and crystal growth. This is especially problematic for some transition metal oxides, such as ZrO_2.

All these drawbacks could be addressed by using a 1D nanomaterial as a hard template, specifically AlOOH (boehmite) nanofibres. This is because the AlOOH nanofibres can be highly dispersed in liquid solutions forming a gel-like network (3D network)[12], which is readily accessible for the infiltration of active components or even small nanocrystallites.

This allows the network to bear an extremely large loading on the surface, and theoretically allows for an even distribution of active components when compared with other traditional supports. After separation from liquid solution, nanocomposites can be stacked together with a very high relative pore volume due to their 1D architecture. Because of these large loading ratios, the properties of the active components will not be compromised by the interaction with alumina support after calcination[13]. Based on this consideration and given the good textural stability of alumina, using alumina nanofibres as hard template highlights a new opportunity to fabricate macroporous frameworks of some transition metal oxides with enhanced thermal and mechanical stability.

In this work, we investigated the synthesis of a series of ZrO_2/Al_2O_3 nanocomposites using boehmite nanofibres as sustainers. Our interest in zirconia stems from its attractiveness as a catalyst and catalyst support which is used in many industrial processes[14-16]. It is also an important ceramic material exhibiting enhanced corrosion, oxidation resistance[17], fracture toughness[18], abrasion resistance[19], and excellent biocompatibility when used in medical applications[20,21]. A nanocomposite with controllable morphology and enhanced structural stabilities may exhibit greater potential in applications in the fields mentioned above. All samples were prepared by depositing various amounts of zirconium species onto a three dimensional framework, spontaneously formed by dispersing wet boehmite nanofibres in butanol, and followed by calcinations at 500^{o}C for 3 hours. The morphological evolutions of as-synthesised nanocomposites were observed as the molar ratio X, where X= 100*Zr/(Al+Zr), was increased from 5 % to 50 % and at high zirconia percentage the macroporous framework of ZrO_2 was successfully synthesised as extremely long ZrO_2/Al_2O_3 composite nanorods with a new core-shell structure, where a layer of tetragonal zirconia nanocrystallites shell was supported on long bundles of alumina nanofibres. The structures and physicochemical properties of resultant nanocomposites were characterised by means of XRD, SEM, TEM, FT-IR, IES, and the N_2 adsorption/desorption isotherms. The formation

of such a structure was examined by the combination of SEM and two *in-situ* techniques, hot-stage Raman and infrared emission spectroscopy (IES).

3.2 EXPERIMENTAL SECTION

Materials. Boehmite fibres were synthesised by steam-assisted solid wet-gel method according to previous reports[22]. Butanol was purchased from Ajax Finechem and zirconium (IV) butoxide (80 wt. % in 1-butanol) was purchased from Aldrich. All these chemicals were used as received.

Nanocomposite preparation. 1D zirconia-boehmite nanocomposites were synthesised by the deposition of a zirconia species onto the boehmite nanofibres. In a typical procedure, 0.39 g of boehmite nanofibres was added to 0.20g of deionised water which was then dispersed into 20 ml of butanol with stirring. This mixture was then stirred for 24 hours to ensure complete dispersion of the nanofibers. During the stirring process, the white suspension was transformed into a translucent gel with relatively high viscosity. Zirconium (IV) butoxide was dissolved into the resultant mixture according to the molar ratios X=100*Zr/(Al+Zr) = 5%, 10%, 15%, 30%, with stirring for 5~10 min. The synthesis procedure for the nanocomposite with molar ratio X= 50% was slightly different. Since the hydrolysis of zirconium butoxide consumes water, the 0.39g of boehmite nanofibres were added with 0.40g deionised water for these samples while the other procedures were kept the same as mentioned above. Subsequently, the viscous fluids were transferred into autoclaves for hydrothermal treatment at 170 ^{o}C for 24 hours. After cooling to room temperature, the resulting nanocomposites were separated by centrifugation (if the products were too sticky to transfer, acetone was added to enable the transfer), and then without any washing the samples were dried at 80 ^{o}C for 1 day, and labelled as Zr-m, where m is molar percentage of Zr. The calcined samples are labelled as Zr-"m"-T, where T is calcined temperature.

The preparation of a pristine ZrO_2 solid was accomplished by hydrolysis of zirconium butoxide dissolved in butanol with addition of a stoichiometric excess water. The resultant

precipitate was calcined at 500 ^{o}C for 3 hours. The Al_2O_3 nanofibre sample was obtained by calcining neat boehmite nanofibres at 500 ^{o}C for 3 hours. These two materials would be used as reference materials to which a comparison can be made in the subsequent characterisation.

Characterisation. *XRD* patterns were collected on a PANalytical X'Pert PRO X-ray diffractometer (radius: 240.0 mm). Incident X-ray radiation was produced from a line-focused PW3373/10 Cu X-ray tube, operating at 40kV and 40mA, providing a $K\alpha_1$ wavelength of 1.540596 Å. The incident beam passed through a 0.04 rad Soller slit, a ½ divergence slit, a 15mm fixed mask, and a 1° fixed antiscatter slit. After interaction with the sample, the diffracted beam was detected by an X'Celerator RTMS detector, which was set in scanning mode, with an active length of 2.022mm. Diffraction patterns for the samples were collected over a range of 3~ 75^{o} 2θ. *Surface Area Analysis* based on N_2 adsorption/desorption techniques were analysed on a Micrometrics Tristar 3000 automated gas adsorption analyser. Samples were pretreated at 200^{o}C under the flow of N_2 for a minimum of 5 h on a Micrometrics Flowprep 060 degasser. *SEM micrographs* were obtained on a FEI QUANTA 200 scanning electron microscope operating at 30kV accelerating voltage with a 2.5 spot size. The samples were dried at room temperature and coated with gold under vacuum conditions in an argon atmosphere ionization chamber to increase surface conductivity. *FT-IR emission spectroscopy* was carried out on a Nicolet spectrometer but modified by replacing the IR source with an emission cell. The description of the cell and principles of the emission experiment have been published elsewhere[23]. *FT-IR spectroscopy* was obtained using a Nicolet 380 FT-IR spectrometer. Samples were characterised in the form of a KBr disc which was prepared by mixing of sample with KBr at ratio of 1 % (w/w), grinding into a fine powder and compressing into discs. *Transmission electron microscopy was* carried out on a Phillips Tecnai F20 TEM. The instrument was equipped with a Field Emission Gun source operating at a High Tension of 200 kV. *Hot-stage Raman spectroscopy* were recorded on a Renishaw 1000 Raman microscope system. The spectra were excited by a He-Ne laser (633 nm) at a resolution of 2 cm^{-1} and measured at elevated temperatures on a

Linkam thermal stage (Scientific Instruments Ltd, Waterfield, Surrey, England). Repeated acquisition was accumulated for 20 times with 10 s exposure time to improve the signal to noise ratio, and the 520.5 cm^{-1} line of a silicon wafer was used to calibrate spectra.

3.3 RESULTS AND DISCUSSION

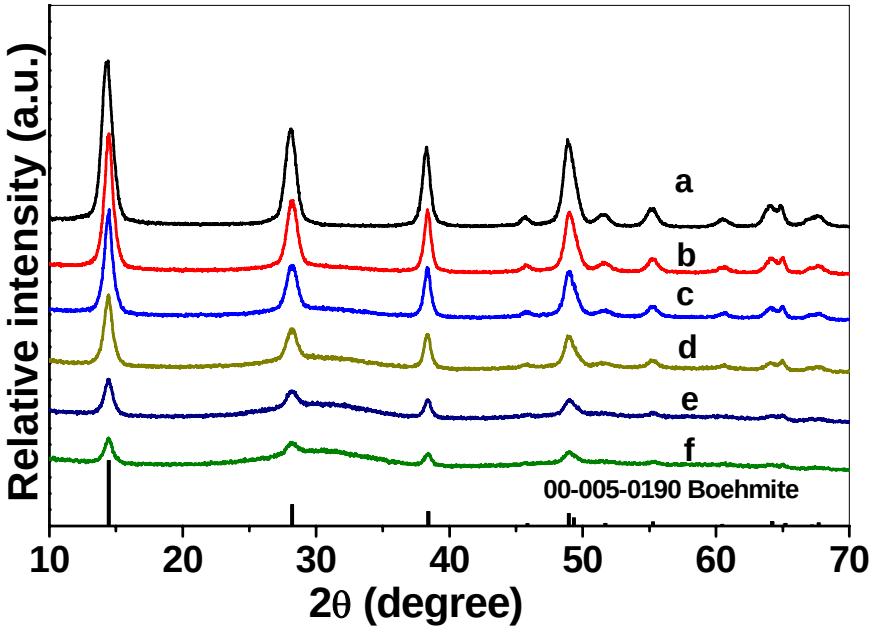

Figure 1. XRD patterns of composite nanofibres (a) pristine boehmite nanofibres, (b) Zr-5 (Zr%=5 mol%), (c) Zr-10 (Zr%=10 mol%), (d) Zr-15 (Zr%=15 mol%), (e) Zr-30 (Zr%=30 mol%), (f) Zr-50 (Zr%=50 mol%)

X-Ray Diffraction. X-Ray Dffraction is used to characterise crystalline phases of the zirconia on boehmite nanofibres. XRD signal of pristine boehmite nanofibres matches the peak positions of orthorhombic AlOOH (γ-AlOOH, JCPDS 00-005-0190). For as-synthesised nanocomposites, when the Zr molar percentage is below 5%, the XRD patterns of samples are almost identical to that of pristine boehmite nanofibres. When the Zr percentage increases above 10%, a broad feature between 2θ=20~ 37° can be observed, which is ascribed to the diffractions of amorphous material, likely zirconia, since the intensity of this "hump" increases with increasing zirconia content, while the diffraction peaks corresponding to the boehmite nanofibres are weakened gradually.

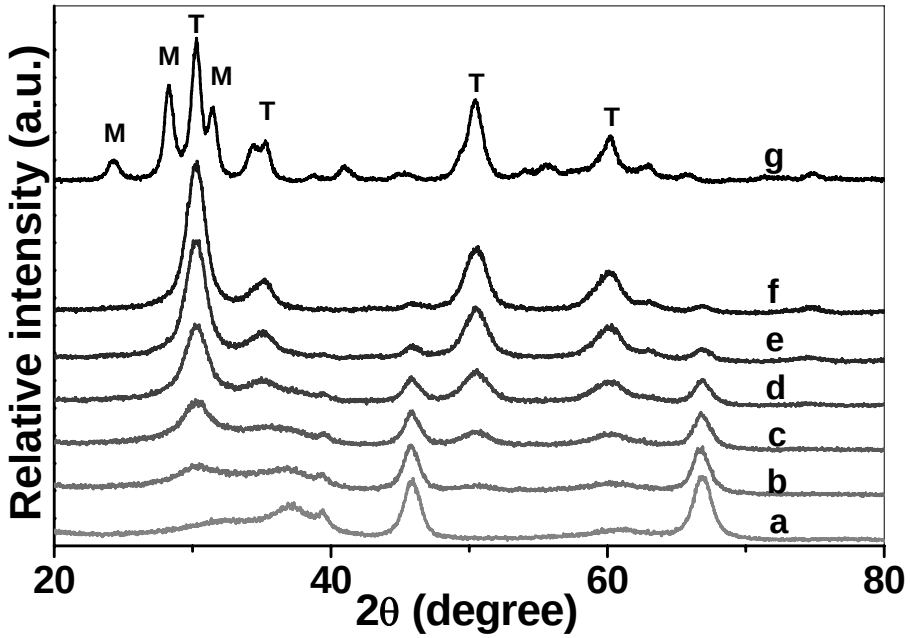

Figure 2. Powder XRD patterns of a) Al_2O_3 nanofibres; b) Zr-5-500; c) Zr-10-500; d) Zr-15-500; e) Zr-30-500; f) Zr-50-500; g) Pristine ZrO_2 (M and T represent monoclinic ZrO_2 and tetragonal ZrO_2, respectively)

The XRD patterns for the nanocomposites calcined at 500°C are given in Figure 2. It is evident that the nanocomposites based on boehmite nanofibres transform into nanocomposites containing γ-Al_2O_3 during calcination, which is consistent with the previous literature[24]. In addition, it can also be observed that with increasing zirconium content, the intensities of the diffraction peaks of γ-Al_2O_3 gradually decrease and become almost undetectable at 50 mol% Zr. This is due to the relative concentration of the alumina decreasing as well as the inherently poor intensity of peaks of the alumina[25]. As compared with pristine γ-Al_2O_3 nanofibres, the nanocomposite with 5% molar ratio shows a broadened peak at ca. 30°, which increases in intensity with increasing zirconia content, and can be confidently identified as the (101) plane of tetragonal zirconia when Zr molar percentage is above 15 %. No peak corresponding to monoclinic zirconia is observed in the patterns for all these nanocomposites. However, when pristine zirconia is calcined under the same

conditions as the other nanocomposites, a small proportion of monoclinic zirconia is observed in addition to the tetragonal phase. This indicates that the transformation from the metastable tetragonal phase to the monoclinic phase is retarded when zirconium species are incorporated onto the surface of the alumina nanofibres.

The results of Rietveld refinements of the XRD data for these ZrO_2/Al_2O_3 nanocomposites are summarized in Table 1. The lattice parameters determined in this work show that the lattice constant of cubic γ-Al_2O_3 slightly increases with the addition of small amount of zirconium. In agreement with some literature reports[26], this indicates that Zr ions could be accommodated into the alumina structure. In contrast, the lattice constant of the tetragonal zirconia seems to be unchanged as the Zr percentage varies from 15 % to 50 %. However, as compared with pristine zirconia, the cellages of tetraganol zirconia in the as-synthesised nanocomoposites do exhibit a decrease in tetragonality (c/a), which shows the impregnation of aluminium atoms is not possible past an initial amount[27].

It is well known that monoclinic ZrO_2 is stable from room temperature up to 1000^{o}C, with it transforming into the tetragonal phase above 1170^{o}C[28]. Stabilized tetragonal zirconia can exist at ambient temperature, when prepared using certain methods, such as adding divalent or trivalent oxides into the pristine oxide, or simply preparing it by the low temperature calcination of zirconyl nitrate or precipitating it from zirconium aqueous solution under alkaline conditions. Therefore, the occurrence of high temperature phase has been accounted for by the formation of a solid solution[29,30] and possibly as a result of the increased stability from the small size crystallites i.e., that the tetragonal zirconia is favoured below a critical crystal size $\approx$300 nm[31].

Table 1. Lattice parameters evolvement of γ-Al_2O_3 phase and tetragonal zirconia phase for the calcined sample with various Zr/Al molar ratios

Sample	γ-Al_2O_3 phase (cubic)			Zirconia nanocrystallite (tetragonal)		
	a[Å]	b[Å]	c[Å]	a[Å]	b[Å]	c[Å]
Al_2O_3 nanofibres	7.918±6	7.918±6	7.918±6	—	—	—
Zr-5-500	7.929±8	7.929±8	7.929±8	—	—	—
Zr-10-500	—	—	—	—	—	—
Zr-15-500	—	—	—	3.603±3	3.603±3	5.15±3
Zr-30-500	—	—	—	3.601±3	3.601±3	5.13±3
Zr-50-500	—	—	—	3.601±2	3.601±2	5.12 ±1
Pristine ZrO_2	—	—	—	3.590±4	3.590±4	5.20±2

Table 2. Crystallite dimension in (101) direction of tetragonal phase for pristine zirconia and zirconia deposited on alumina nanofibres with various zirconia content (The data were derived from X-ray diffraction patterns)

Sample name	Peak position (2θ)	FWHM (2θ)	Crystallite dimensions(nm)
Pristine ZrO_2	30.25	0.92	9.0
Zr-100-500	30.22	1.73	4.8
Zr-50-500	30.22	2.01	4.1
Zr-20-500	30.26	2.56	3.2
Zr-10-500	30.42	4.00	2.1

The crystal sizes of tetragonal zirconia for all the samples including the pristine zirconia and ZrO_2 - Al_2O_3 nanocomposites were calculated by the Scherrer equation and are listed in

Table 2. As the zirconium molar percentage in the nanocomposite is increased from 10 % to 50 %, there is a resulting increase of crystal size from 2.1 nm to 4.8 nm in (101) direction, smaller than that of the pristine zirconia, which is 9.0 nm. These results also elucidate the role of the alumina nanofibres in helping to stabilize the tetragonal zirconia through a reduction of the crystallite size.

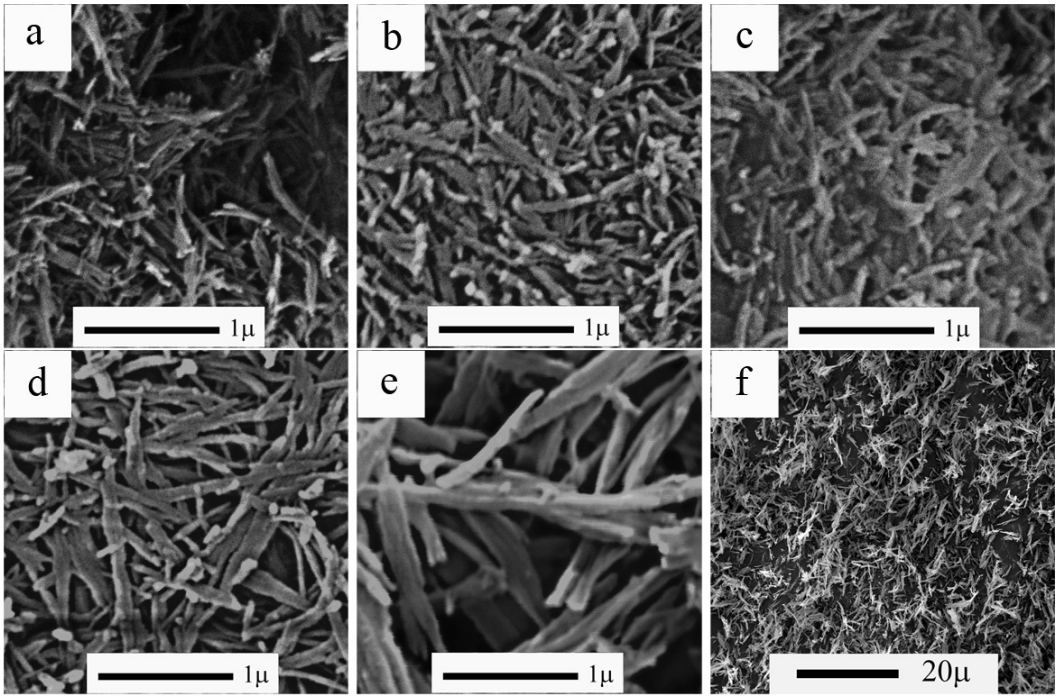

Figure 3. SEM images of 1D ZrO_2/Al_2O_3 nanocomposites obtained by calcination at 500°C: a) Zr-5-500; b) Zr-10-500; c) Zr-15-500; d) Zr-30-500; e) Zr-50-500; f) Zr-50-500 at a larger scale

Particle morphology is investigated by SEM and is illustrated in Figure 3. It can be observed that these nanocomposites undergo a macroscale morphological evolution with increasing Zr molar percentage. The zirconia species appear to be dispersed on single or small bundle of nanofibres. The continuity of zirconia coverage and the apparent structural integrity of the 1D-nanocomposite fibres gradually increase as the zirconium content increases. As the Zr molar percentage is varied from 5 % to 15 %, the diameter of these 1D

nanocomposites grows larger. A conspicuous change occurs when the Zr molar percentage is above 30%, the materials become extremely long and broad nanorods, which are *ca*. 100 nm in width and average 1 micron in length for Zr-30-500 and 130 nm in width and average 2 microns in length for Zr-50-500. By convention, for a nano-fibrous material, which consists of randomly stacked nanofibres, the resultant large intercrystallite voids are referred to as the porosity of such a material. Therefore, with the diameter of nanocomposite increasing, the inter-particle voids resulting from specific morphology of 1D nanomaterials are consequently extended. When the Zr molar percentage is above 30%, macropores in the range of 200 nm to 400 nm can be clearly observed (Figure 3d). Especially for sample prepared with 50 mol% Zr, a distinct macroporous framework is fabricated from extremely long nanorods which are formed by the incorporation of several nanorods along the direction of its length (Figure 3f). This porous structure model is also supported by the results of N_2 adsorption/desorption experiments.

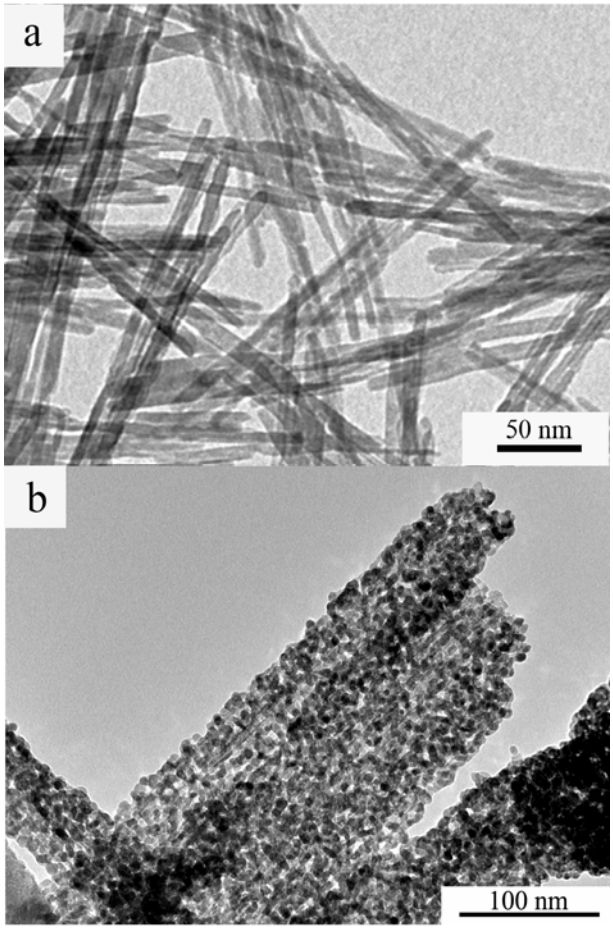

Figure 4. TEM image for γ-Al_2O_3 nanofibres and the 1D nanocomposite with 50 mol% Zr

Representative TEM images for γ-Al_2O_3 nanofibres and the 1D nanocomposite with 50 mol% Zr are shown in Figure 4. The γ-Al_2O_3 nanofibres are very thin and relatively short around 10~ 20 nm in diameter and 100~ 200 nm in length. However, the structure for the sample with 50 mol% Zr is significantly different: a great number of zirconia nanocrystallites can be easily identified by their dark contrast in the TEM, as a result of electron density contrast between Al and Zr[32]. The zirconia crystallites are about 5 nm, in agreement with calculations from XRD. These small nanoparticles, with interconnected architectures, form a relatively large porous nanorod.

Typical TEM bright field and dark field images of this sample show more information on its structure. As the (400) diffraction spot of γ-Al_2O_3 is selected for imaging, the corresponding dark-field micrograph (Figure 5c) illustrates the location of alumina nanofibres, exhibiting relatively large bright areas with fibrous morphology that is congruent with a group of nanofibres connected together. Nevertheless, the imaged electron beam which is diffracted off the (400) diffraction plane of alumina is required to pass through the layer of zirconia, and is also diffracted by this layer. This causes visible diffraction lines from the zirconia and some mottling of the image can also be observed in Figure 5c. In contrast, when the dark-field image is taken using a tilt whose alignment is confluent with a diffraction spot of zirconia, a set of bright spots owing to the zirconia nanocrystallites can be observed (Figure 5d), which also qualitatively indicates that the distribution of zirconia nanocrystallites is uniform and that the alumina is relatively less crystalline. These two dark-field images strongly suggest that the alumina nanorod core comprised of several oriented alumina nanofibers is encompassed by layered zirconia nanocrystallites.

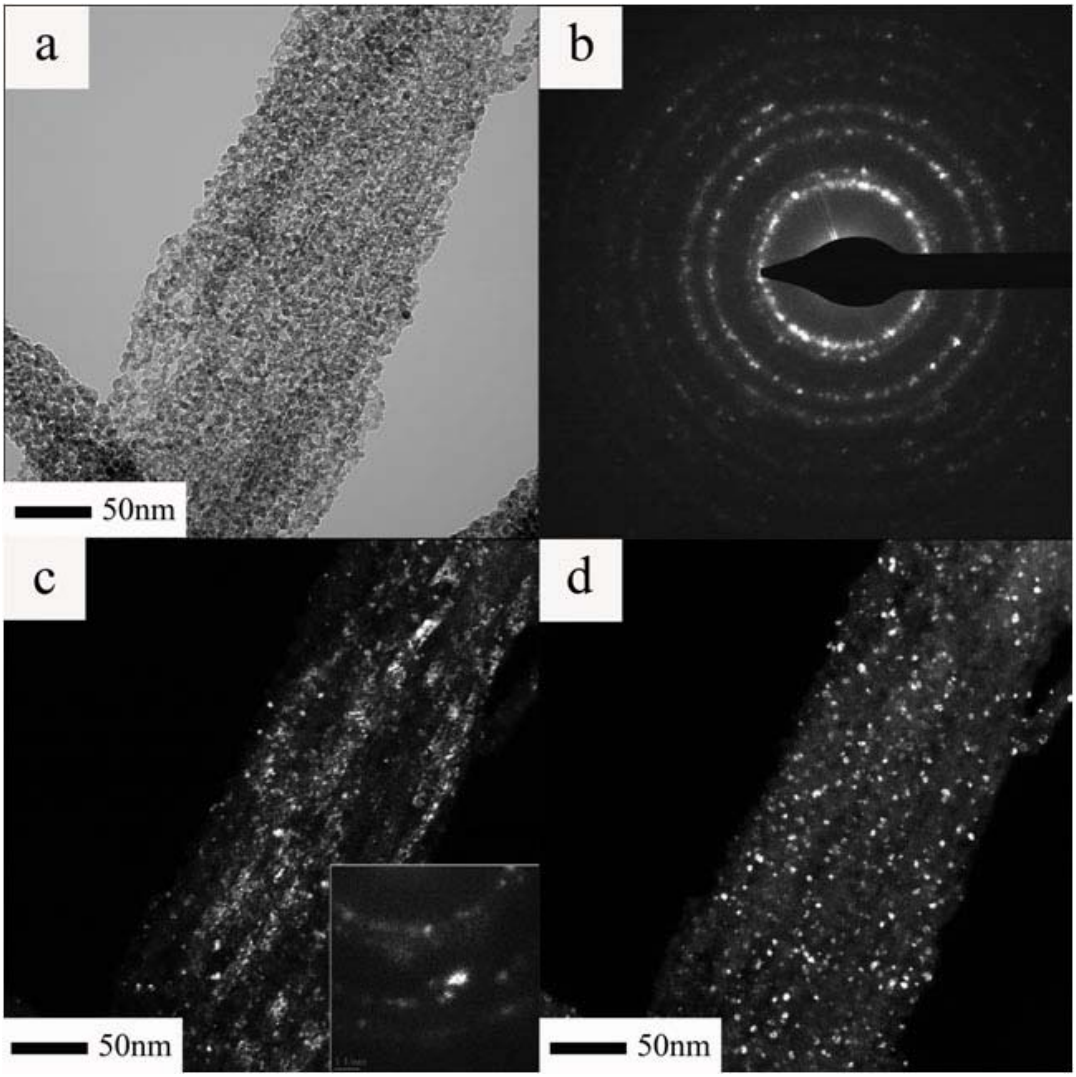

Figure 5. (a) Typical conventional TEM bright field, (b) the select-area electron diffraction pattern taken from this area, (c) the dark field image using the intensity of the (400) diffraction spot of γ-Al_2O_3 (shown as inset image) and (d) the dark field by selecting one of the diffraction rings of zirconia for imaging

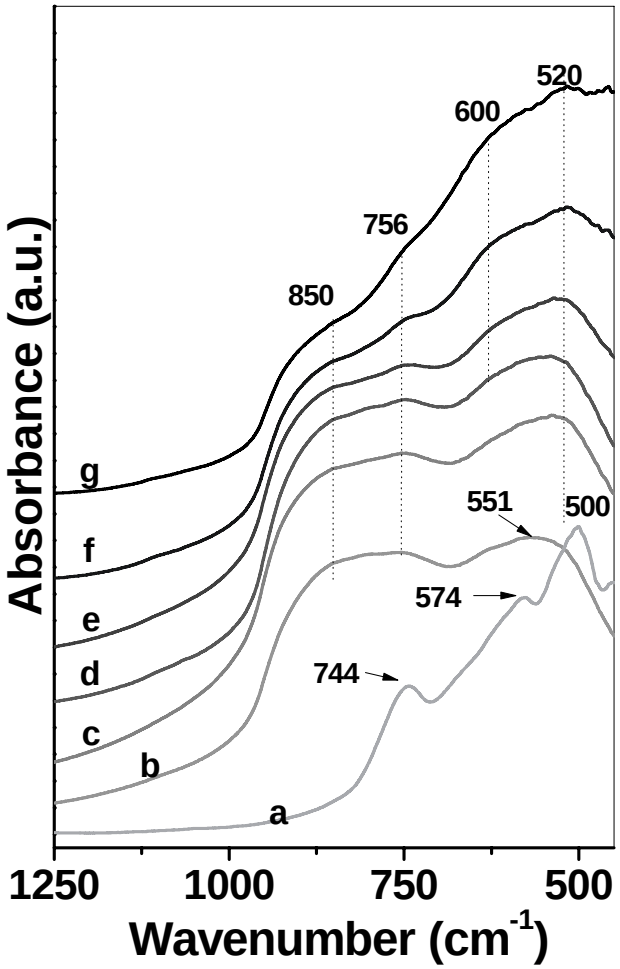

Figure 6. FT-IR spectra of a) pristine ZrO_2, b) γ-Al_2O_3 nanofibres, c) Zr-5-500, d) Zr-10-500, e) Zr-15-500, f) Zr-30-500, g) Zr-50-500

Figure 6 shows the IR spectra of the samples calcined at 500 ºC in the 1250 ~ 450 cm^{-1} range. The pristine ZrO_2 exhibits three peaks at 500, 574 and 744 cm^{-1}. The first band is characteristic of the tetragonal phase of zirconia, while the latter two bands are attributed to the monoclinic phases of zirconia[33] which concurs with the XRD results of pristine zirconia. The pristine γ-Al_2O_3 nanofibres exhibit three broad peaks: at 551, 756, and 850 cm^{-1}. In the literature on transition aluminas prepared by heating treatment of boehmite[34,35], the broad band with maximum absorbance around 551 cm^{-1} has been assigned to AlO_6 stretching mode, and the other two broad features (756 and 850 cm^{-1}) result from AlO_4 stretching.

The broad and unresolved feature of these bands are typical of a complex and disordered crystallographic structure of γ-Al_2O_3, which makes an unambiguous investigation of the impact of zirconia on the Al-O vibrations impossible. Indeed, at low Zr molar percentage, the nanocomposites show similar spectra to γ-Al_2O_3. However, when the Zr molar percentage is higher than 15 %, significant differences can be observed, for example, a strong band generated at 520 cm^{-1} and the appearance of a broad shoulder centered at 600 cm^{-1}. According to the literature, the bands of tetragonal phase of zirconia shift if there are differences in structural parameters, especially differences in the force constants for Zr-O bonds and related bond angles[36] caused by an addition of divalent or trivalent ions. Therefore, the band at 520cm^{-1} is attributed to the characteristic wavenumber shift of the tetragonal zirconia from 500 cm^{-1} resulting from the variation in its tetragonality caused by the interaction between alumina and zirconia species. In addition, a similar shoulder at 600cm^{-1} has been observed for tetragonal zirconia in zirconia-rich glass phase, such as ZrO_2-Y_2O_3[37], ZrO_2-SiO_2[38] system. In this work, the tetragonal zirconia in the ZrO_2-Al_2O_3 system also gives rise to this band; therefore this band presumably corresponds to Zr-O-Al stretching vibration.

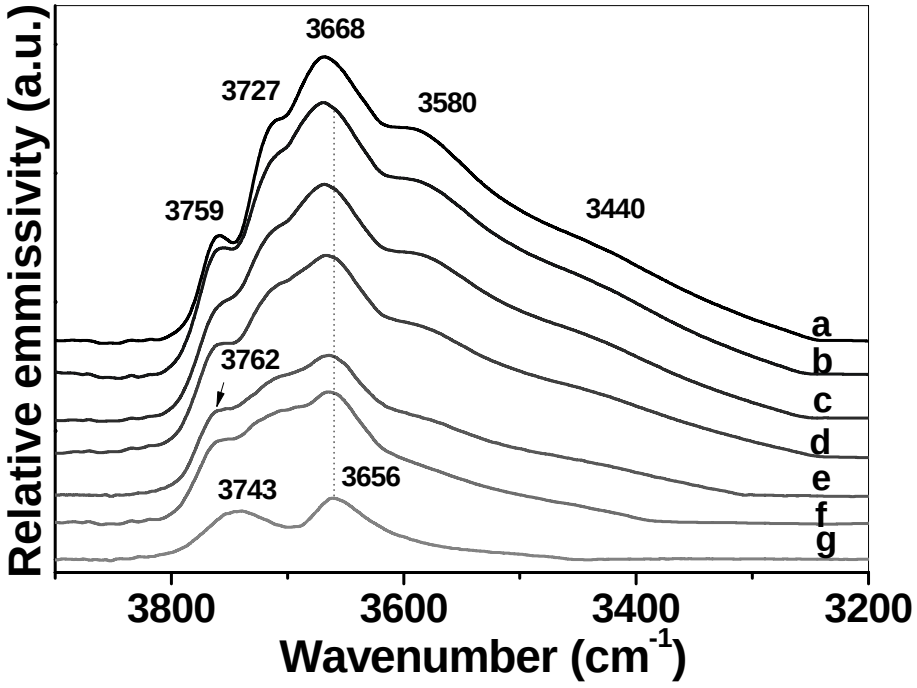

Figure 7. Infrared emission spectra in the region of OH stretching obtained at 400ºC. a) γ-Al_2O_3 nanofibres, b) Zr-5-500, c) Zr-10-500, d) Zr-15-500, e) Zr-30-500, f) Zr-50-500, g) pristine ZrO_2

Figure 7 shows the Infrared Emission spectra (IES) for these nanocomposites in the hydroxyl stretching region. The spectrum for γ-Al_2O_3 nanofibres presents 5 typical bands which have been attributed to the different coordination (tetrahedral or octahedral) of the surface aluminium cations bonded to the hydroxyl group[39]. The two bands located at higher wavenumber, i.e. at 3759 and 3727 cm^{-1} correspond to isolated hydroxyl groups coordinated to one tetrahedral Al^{3+} and octahedral Al^{3+}, respectively. The bands at 3668 and 3580 cm^{-1} are attributed to the hydroxyl groups coordinated to two Al^{3+} ions with two subtypes: an octahedral aluminium ion with a tetrahedral aluminium ion and two octahedral aluminium ions respectively. The band located at the lowest wavenumber corresponds to hydroxyl group coordinated to three Al^{3+} ions, i.e. two octahedral and one tetrahedral alumina[40]. Spectra of pristine ZrO_2 shows two hydroxyl stretches, located at 3743, and 3656 cm^{-1} which have been assigned to hydroxyl groups coordinated to two and three Zr^{4+} ions, respectively[41].

For ZrO_2/Al_2O_3 nanocomposites, the intensities of the hydroxyl bands corresponding to alumina decrease with increasing Zr molar percentage, indicating the alumina hydroxyls are sequentially replaced. At low Zr molar percentage, the spectra of nanocomposites is very similar to that of γ-Al_2O_3, with the five types of alumina hydroxyl group being observed. This result is consistent with pervious literature reports[26]. However, from low to high Zr molar percentage, there is a gradual band shift from 3668 to 3656 cm^{-1}, indicating the surface alumina hydroxyls have been replaced by the tri-bridged OH group of zirconia. It should be noted that the hydroxyl band at 3765 cm^{-1}, assigned to isolated hydroxyl group coordinated to one Zr^{4+} happens to coincide with the band for the isolated hydroxyl group coordinated to one tetrahedral Al^{3+}. Therefore, the band at 3762cm^{-1} should be assigned to isolated hydroxyl group of zirconia for these nanocomposites[41,42]. Moreover, a broad shoulder in the 3692~ 3742 cm^{-1} range remains until a Zr concentration of 50 mol%, and may correspond to several different types of hydroxyl stretching deriving from alumina species interacted with Zr ions, which leads to the formation of a practically unresolvable profile.

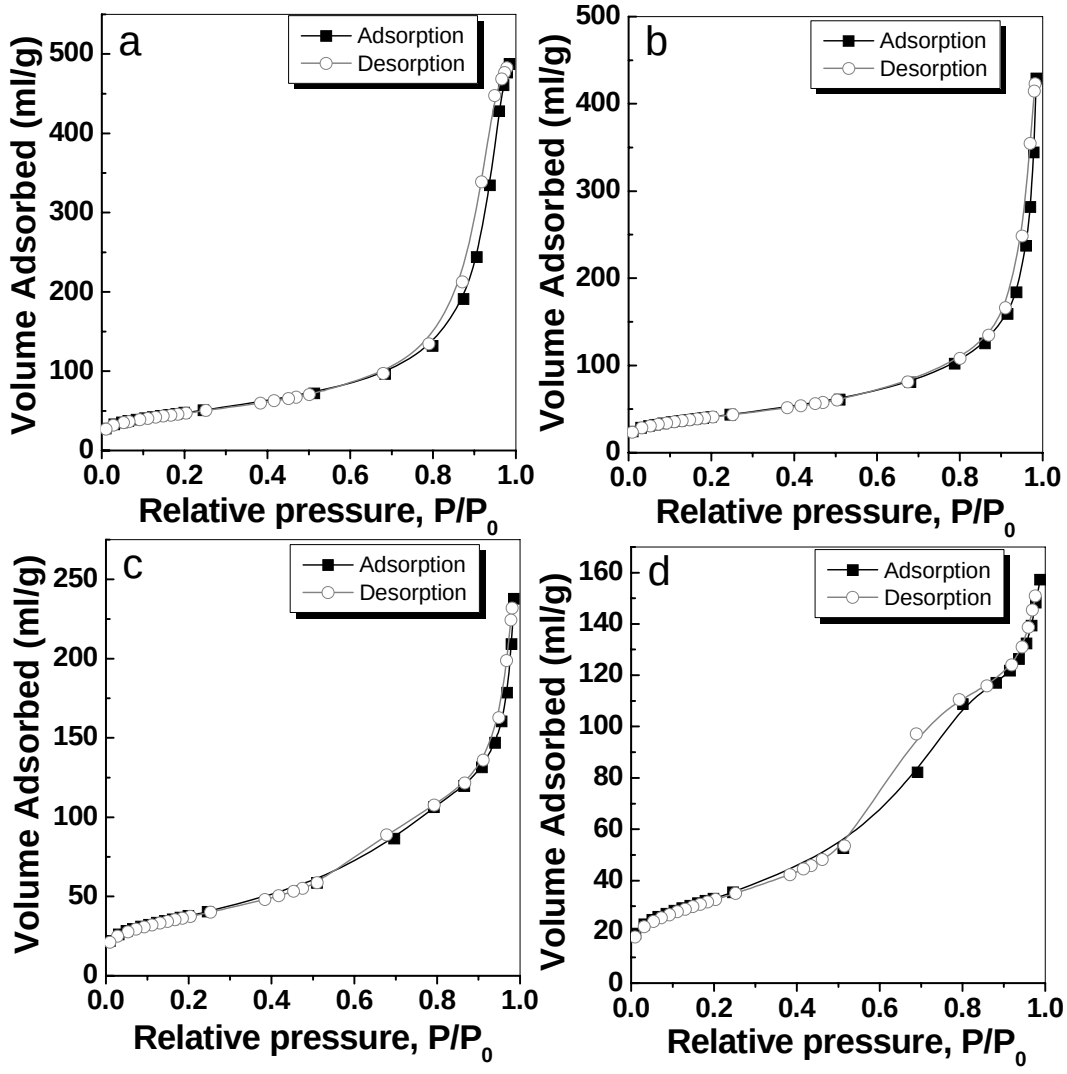

Figure 8. Nitrogen adsorption and desorption isotherms for some representative samples with various Zr molar percentage. a) γ-Al_2O_3 nanofibres, b) Zr-15-500, c) Zr-30-500, d) Zr-50-500

The surface area and pore structures of the samples are investigated by nitrogen adsorption-desorption isotherms. Figure 8 shows representative results to illustrate the textural changes as Zr content increase. Pristine alumina nanofibres and all samples with Zr molar percentage up to 15 % exhibit non-reversible adsorption-desorption isotherms with a hysteresis loop characteristic of capillary condensation, meaning the samples have a mesoporous nature. However, a distinct behavior can be perceived by the comparison of hysteresis loops. The hysteresis loop of the pristine alumina nanofibre falls within the H3

and H4 categories, which is typical of slit-type pores generated from the interparticle porosity of plate or fiber-like morphology[43]. The hysteresis loop for the Zr-15-500 sample exhibits a loop closer to that of the H3 destination, which shows a higher slope. According to Sing's study[44], H4 loop is attributed to narrow slit-like pores in the samples. Therefore, such transformations in a hysteresis loop reflect the increase in the mean size of the slit-like pore.

As the Zr molar percentage increases to 50 %, the isotherm takes a shape resembling a combination of Type II and IV adsorption. The adsorption branch of isotherm exhibits a capillary condensation step centred at relative pressure of about 0.67. Furthermore, at higher relative pressures, the nitrogen uptake dramatically increases and such tendency is sustained throughout the entire pressure range. The desorption branch coincides with the adsorption branch until the relative pressure is lower than 0.8, where a hysteretic loop typical of a H2 was observed. This type of hysteresis is indicative of bottle ink pore networks[45]. This pore network is formed from the zirconia nanocrystallites, which has been confirmed by TEM (Figure 4). As the isotherm is a combination of type II and IV absorption, it can be inferred that the nanocomposite material contains both meso- and macropores.

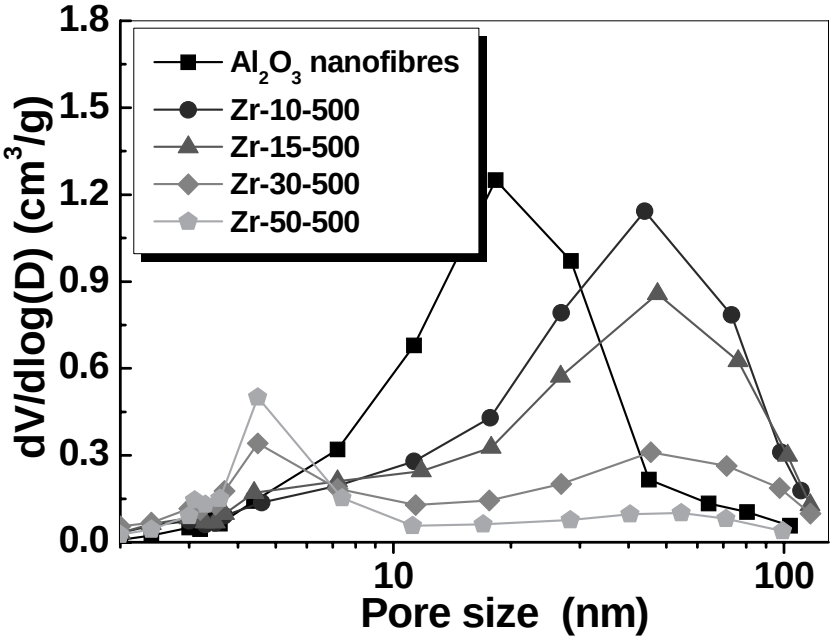

Figure 9. Pore size distributions for samples with various Zr molar percentage

Figure 9 illustrates the pore size distributions of representative samples. Alumina nanofibres have a wide pore size distribution from 1 nm to 100 nm, which is a characteristic feature of pores corresponding to the intercrystallites voids constituted by nanofibres. All nanocomposite samples show two pore distributions: one is 2-10 nm in size while the other is 10-100 nm in size. The former distribution is attributed to the pores formed by incorporation of zirconia nanocrystallites and the latter is assigned to those formed due to the 1D morphology of as-synthesised nanocomposites. It can be observed, with increasing the zirconia content, the number of 2-10 nm pores increases due to the increase of zirconia nanocrystallites, but surprisingly the number of 10-100 nm pores exhibits a decreasing tendency. When considered in light of the SEM results (Figure 3), this is because the inter-particle voids of the as-synthesised 1D nanocomposites have gradually extended to macropores where the majority of the distribution exceeds the measurable range for N_2 physisorption. With increasing Zr content and the increase in length of fibrous nanocomposites, the number of large pores in the 10-100 nm range gradually decreases,

which also results in a decrease in the average pore size and pore volume because these values are only calculated from the pores in the 2-100 nm range (Table 3).

Table 3. Pore structures of γ-Al_2O_3 nanofibres and as-synthesised nanocomposites

Sample	BET surface area(m^2/g)	Average pore size (nm)	Pore volume (cm^3/g)
γ-Al_2O_3 nanofibres	171	17.59	0.754
Zr-5-500	154	25.96	0.997
Zr-10-500	156	20.79	0.811
Zr-15-500	147	18.00	0.663
Zr-30-500	137	10.76	0.368
Zr-50-500	120	8.13	0.243
ZrO_2	44	17.60	0.196

Formation mechanism. In this work, we use thin boehmite (AlOOH) nanofibres as a hard-template to fabricate a series of ZrO_2/Al_2O_3 1D nanocomposites with an extremely large range of Zr content from 5 mol% to 50ml%. Zirconia is deposited on boehmite nanofibres by the hydrolysis of zirconium butoxide followed by calcination at 500 ^oC. It is also demonstrated that when Zr content is above 30 mol%, the as-synthesised nanocomposites form a new class of 1D nanorods with large aspect-ratios and the resultant nanorods can easily construct into macro-meso porous materials without the use of space filler or pore-regulating agents.

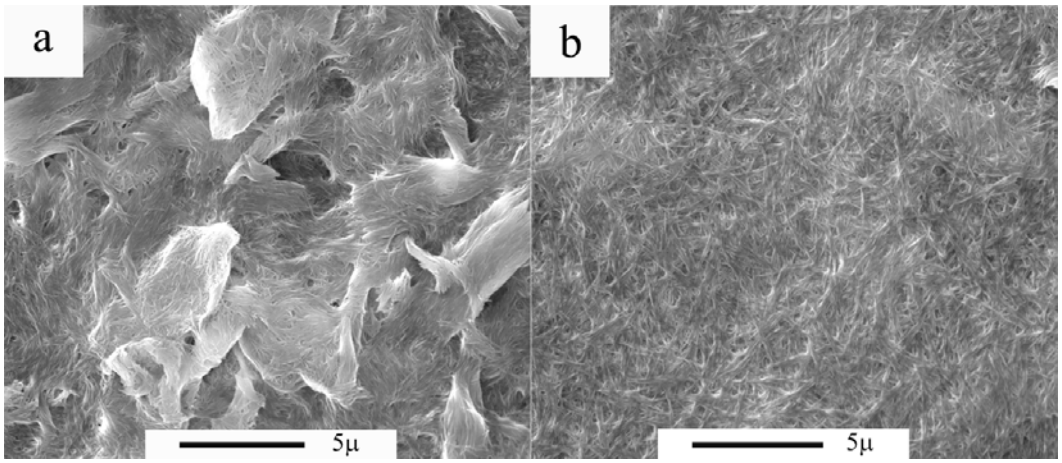

Figure 10. SEM images of thin films made from a) Dry boehmite nanofibres butanol suspension and b) wet boehmite nanofibres gel

Our experiments show that the addition of water to boehmite nanofibres before their dispersion into butanol is essential to form the desired structure. Dry boehmite nanofibres can also be dispersed into butanol but without the formation of a viscous dispersion, while only wet boehmite nanofibres disperse into butanol forming a viscous translucent gel. To investigate the differences in the dispersive state, these two fluids were made into thin films on glass slides by the doctor-blade method. The two thin films were observed via SEM. As shown in Figure 10, the film made from dry boehmite nanofibres butanol suspension is stacked by large, uneven particles, indicating the dry boehmite nanofibres dispersed in butanol are flocculated aggregations. However, the film made from the wet boehmite nanofbre gel is woven by numerous, evenly distributed, long bundles of boehmite nanofibres suggesting that a three-dimensional open grid is formed in gel-like fluid by cross-linked long bundles. The mixture is also viscous because of this[46]. These long bundles are very similar to the morphology of as-synthsized ZrO_2/Al_2O_3 composite nanorods with Zr percentage >30%.

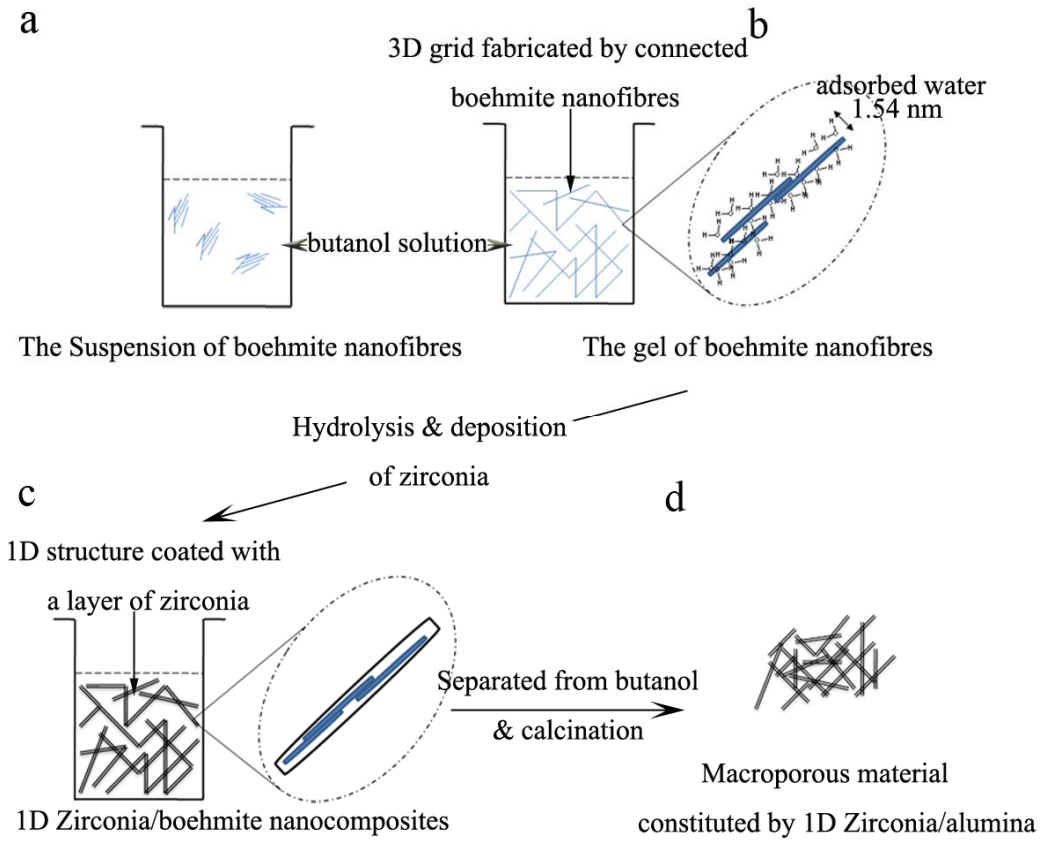

Figure 11. Schematic illustration of the formation mechanism of 1D zirconia/alumina nanocomposites and the macroporous material constituted by their 1D nanostructure: a) boehmite nanofibres are stabilized in butanol solution by forming an aggregated structure. b) 3D grid is formed by connected boehmite nanofibres. c) Zirconium butoxide is exclusively hydrolysed on the surface of boehmite nanofibres. d) 1D structure is maintained after separation and naturally packed into a macroporous material

Accordingly, the formation process is illustrated in Figure 11. It is worth mentioning here that since butanol is a hydrophobic alcohol, the pre-adsorbed water on boehmite nanofibres will be immobilized on hydroxyl surface of boehmite crystallites in butanol dispersion. Obviously, such long bundles are directly formed from linear boehmite nanofibres which should be connected (or confined) by a thin layer of water (Figure 11b). Subsequently, amorphous zirconia is precipitated onto the framework with the hydrophobicity of butanol directing the hydrolysis of zirconium butoxide onto the outer-surface of the boehmite

nanofibres, rather than in the bulk liquid phase. The long bundle of boehmite nanofibres is completely wrapped by a layer of amorphous zirconia at high Zr molar percentage, forming a new class of 1D nanocomposite (Figure 11c). Further, after separation from liquid phase, a macroporous framework with surface properties close to that of pristine zirconia will be inherently formed by the stacking of these nanorods as Zr molar higher than 30%.

XRD results identified that the hydrolysis of zirconium butoxide around the outside of a long bundle generates an amorphous zirconia layer which further stabilizes the boehmite bundles. However, the stronger interaction should also be generated during calcination with the phase transition of both species. This procedure is traced by two *in-situ* techniques, infrared emission spectra and hot-stage Raman.

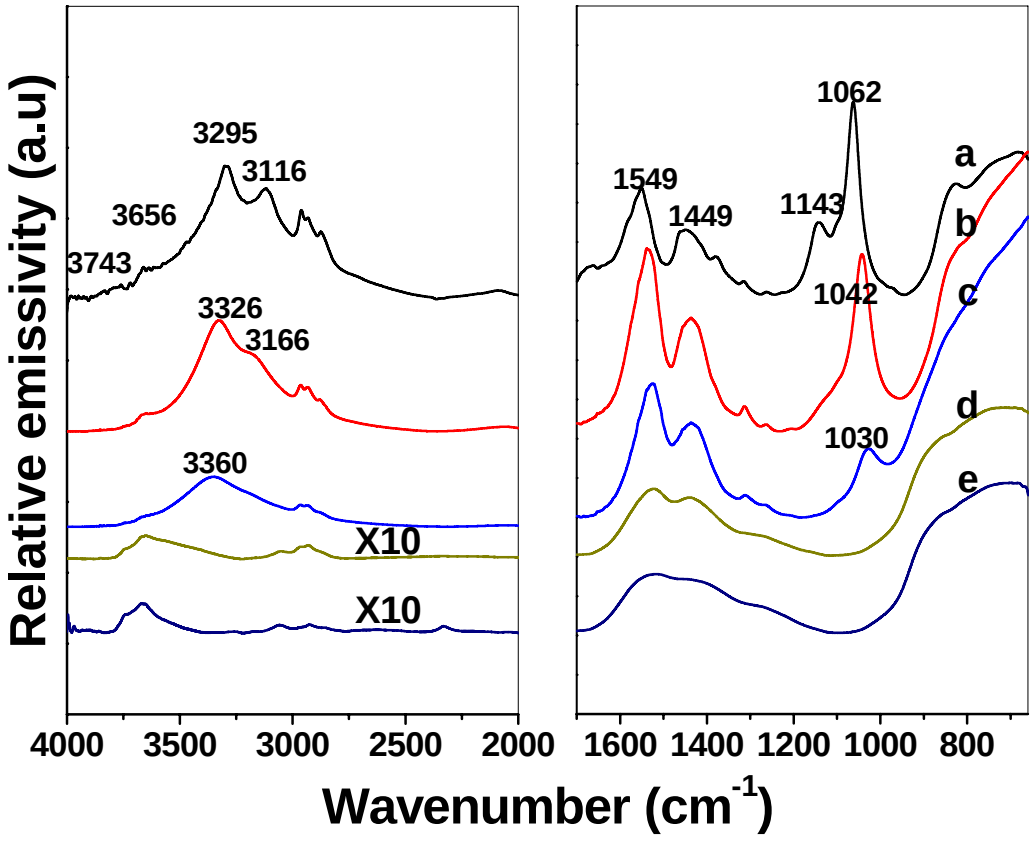

Figure 12. Infrared emission spectra of the Zr-50 characterised at a) 100°C; b) 300°C; c) 400°C; d) 450°C; e) 500°C

The infrared emission spectra of Zr-50 are collected over the range 100^{o}C~ 500^{o}C. The spectra obtained at 100 ^{o}C (Figure 12a) shows that the two strong bands at 3116 and 3295 cm^{-1} correspond to symmetric and antisymmetric stretching vibration of OH group of boehmite, and the intense bands at 1062 and a shoulder at 1143 cm^{-1} have been attributed to the symmetric and antisymmetric bending modes of Al-O-H[35]. In addition to the vibration from well crystallized boehmite, two tiny humps at 3656 and 3743 cm^{-1} are attributed to the hydroxyl groups from the amorphous zirconia gel. The two broad peaks centered at 1549 and 1449 cm^{-1} are tentatively ascribed to the ν_{as}COO- vibrations and ν_{s}COO- vibrations, which may indicate the butanol is chemsorbed on the surface of amorphous zirconia and reversibly changes to carboxyl group[47,48]. These two carboxyl vibrations give a difference of $\Delta \approx 100$ cm^{-1}. Unidentate coordination gives rise to a much larger difference between the antisymmetric and symmetric carboxylic frequencies (Δ=380~450 cm^{-1}), and chelating bidentate coordination lead to much smaller frequency differences of about 40~70 cm^{-1}. Thus, the bond existing between the carboxylic group and the zirconium centre is a bridged kind of bonding where two metal centers are coordinated to one carboxylic group[49].

During the heating process, the symmetric and antisymmetric stretching vibrations of boehmite hydroxyl group completely disappear by 450^{o}C, indicating the boehmite nanocrystallites transformed into γ-Al_2O_3. Although the boehmite crystallites remain until 400 ^{o}C, the shifts of the stretching mode towards low frequency and the bending vibration towards higher frequency suggest that the effect of hydrogen bonding is gradually weakened, indicating that dehydration takes place from 100^{o}C. At relatively high temperatures from 200^{o}C to 300^{o}C, the condensation of aluminium hydroxyl groups proceeds, which occurs not only between the adjacent lamellar plane of boehmite single crystals but also between the tightly contacted nanofibres in a single bundle which enhances the structural stability of nanocomposites.

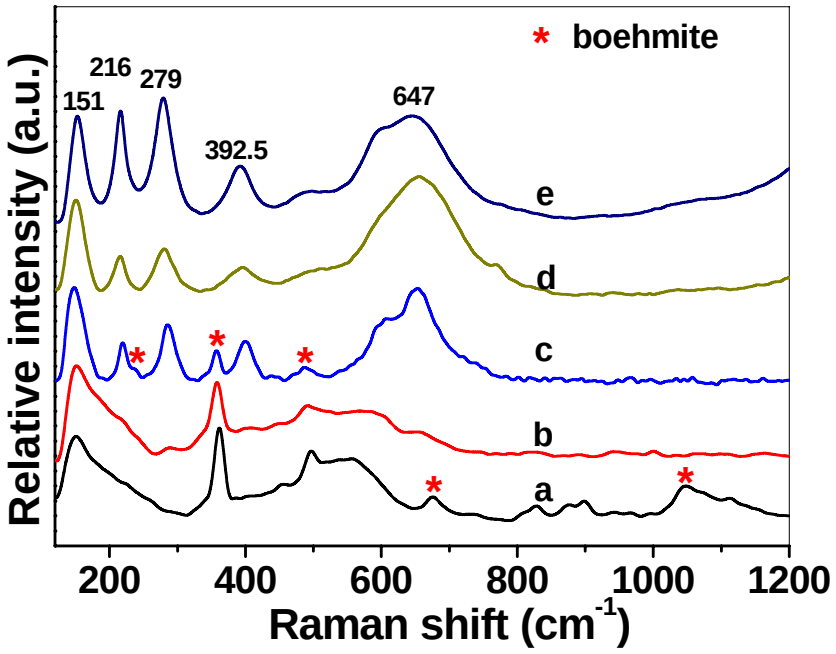

Figure 13. *In-situ* hot-stage Raman spectra of Zr-50 characterised from 100°C to 500°C: a) 100°C, b) 300°C c) 400°C d) 450°C e) 500°C

In-situ hot-stage Raman spectra of Zr-50 are also characterised over the same temperature range to IES. The sample characterised at 100°C shows four dominant Raman bands at 360, 496, 673, 1045 and 1286 cm^{-1}, which belong to the boehmite nanocrystallites. The strong band at 360cm^{-1} is assigned to the vibration of fully symmetric A_g mode, in which all aluminium and oxygen atoms move parallel to the b-axis of crystallography. The bands at 495 and 673 cm^{-1} originate from a doubly degenerate mode of the AlO_6 octahedron[24], while the band at 1045 cm^{-1} corresponds to the scissoring vibration of surface OH groups[50]. The deposited zirconium species generates two broad humps at 100~ 300 cm^{-1} and 400~ 650 cm^{-1}, which should be attributed to hydrated zirconia. The extremely large bandwidths also indicate a large range of bond lengths indicative of low crystallinity.

For the spectra collected at 300 °C, a broad band at 647 cm^{-1} is due to amorphous zirconia gel. Once this amorphous gel is heated to 400°C the bands of crystalline zirconia appear. Since the γ-Al_2O_3 is featureless in this Raman region[51], the bands for boehmite totally

disappear at 450°C indicating the phase transition from boehmite to γ-Al_2O_3 appears to have completed at this temperature, which is consistent with IES results. Although at this temperature, the the positions of the band in this work are slightly different from the results in the literature for pristine tetragonal zirconia (which is given in parentheses): 647 (639), 392 (472), 279 (312), 216 (269), 151 (150)[52,53] these five predominant Raman bands should be attributed to the tetragonal zirconia, because the monoclinic zirconia belongs to monoclinic P21/c space group which has four molecules per unit cell predicting about 18 Raman active modes. Cubic zirconia belongs to the Fm3m space group, only one molecule per unit cell and generates one F_{2g} Raman active mode, while tetragonal zirconia belongs to the P42/nmc space group, with two molecules per unit cell having six Raman active modes[54]. It is well known that the Raman frequencies are very sensitive to the structure and band distance, especially for the metal oxide stretching modes. The shift of Raman bond to higher wavenumbers corresponds to the shortening of metal oxygen distance while the shift to lower wavenumbers indicates the lengthening of such distance[55]. Therefore, the variation of Raman bands of tetragonal zirconia may result from the change of tetragonality, while also revealing the strong support-coating interaction between zirconia nanocrystallites and the γ-Al_2O_3.

Advantages of the technique. Compared with a gel formed by nanoparticles, the network in boehmite nanofibres gel structure can be more easily conserved and consolidated as 1D nanocomposite. This is largely due to the random linkages between two orientated nanofibres can generate stronger interactions resulting from longer-range contact when compared to that of isotropic nanoparticles. Therefore, there is no need for specific techniques during the preparation steps such as freeze-drying or supercritical drying. This indicates that it is amenable to commercial scale-up.

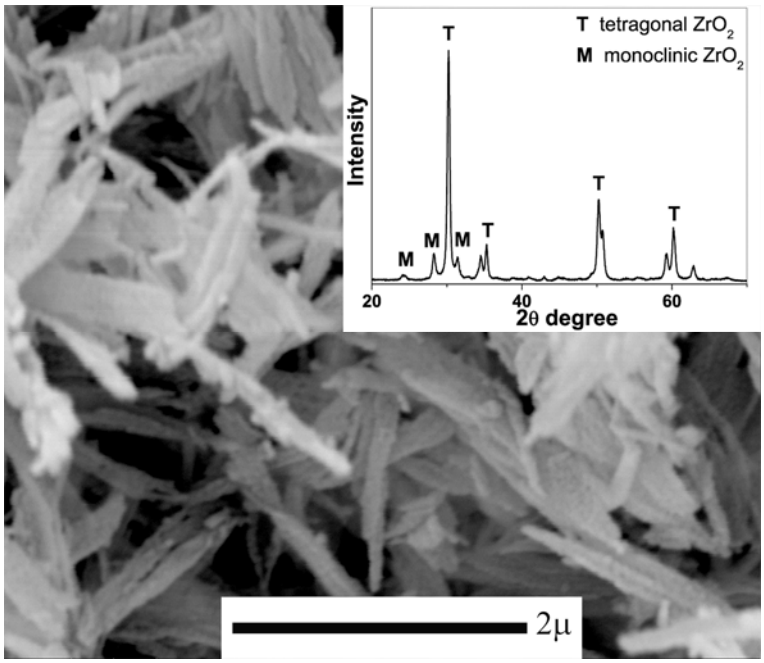

Figure 14. SEM image and XRD pattern for the sample with 50 % Zr molar percentage after calcination at 1000 °C

Besides the benefit of a facilitated synthesis, compared with traditional macroporous materials, as-synthesised 1D nanocomposite also provides high thermal stability to the structure at the calcination temperature. This is illustrated in figure 14 by SEM image and XRD pattern (inset image). After calcination at 1000°C, for the sample with 50 % Zr molar percentage, the calculation from the XRD pattern shows that the crystallite size of tetragonal zirconia dramatically increases at such high temperature and that at this temperature there is also the formation of some monoclinic zirconia. However, the alumina nanofibres maintained their morphology irrespective of crystallite growth and phase change of the zirconia, which is not achievable by a hierarchical material constructed from a pristine oxide. Moreover, after calcination at 1000°C for 3 hours, the resultant material still possesses a relatively large surface area mainly determined by crystal size of zirconia (Table 4).

Table 4. Structure change for the sample with 50 % Zr molar percentage after calcining at 500 °C, 750 °C and 1000 °C for 3 hours

Sample name	Crystallite dimensions(nm) in (101) direction	BET surface area(m^2g^{-1})	Pore volume (cm^3/g)[b]
Zr-50-500	4.8	120	0.243
Zr-50-750	7.2	73	0.200
Zr-50-1000	21.4	28 [a]	0.113

[a] The surface area mainly contributed from the meso-pores formed by ZrO_2 nanocrystallites

[b] Macro-pores fabricated by the 1D nanocomposites are not detectable by N_2 physisorption

Inhibition to ZrO_2 crystal growth

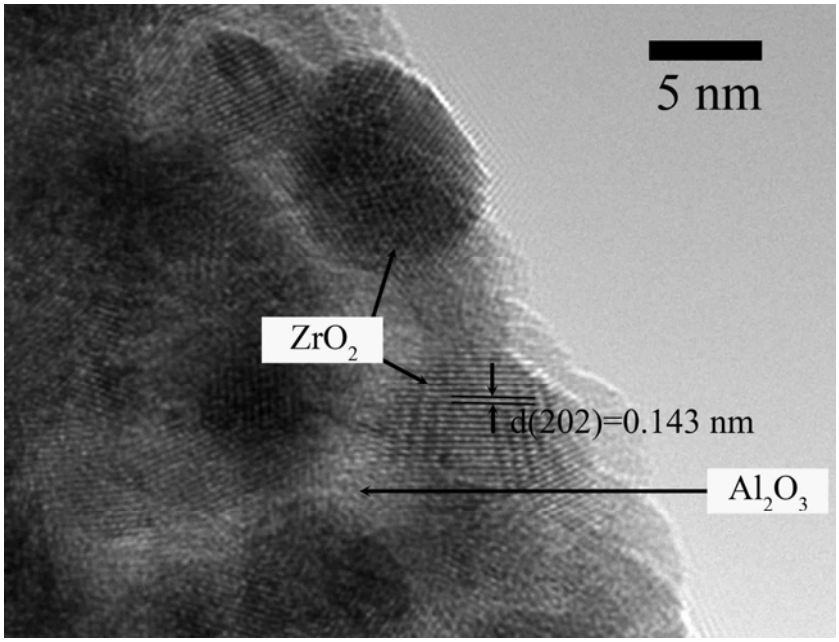

Figure 15. HRTEM image showing the embedment of ZrO_2 nanocrystallites on Al_2O_3 nanofibres

An interesting phenomena occurring in this work is that the crystal size of zirconia for nanocomposites was much smaller than that of pristine zirconia prepared under the same

conditions. This can be attributed to two factors: the strong metal oxide - γ-alumina interaction effect[56] and the large "out-surface" of alumina nanofibres. The strong interaction between γ-alumina and zirconia nanocrystallite is derived from the diffusion of zirconia to the γ-Al_2O_3 support, which can be illustrated by the change of lattice parameters of γ-Al_2O_3 in Table 1. More importantly, the HRTEM image (Figure 15) for the sample with 50 mol% Zr shows that zirconia nanocrystallites are embedded on γ-Al_2O_3 support. This is a strong evidence to illustrate their strong interaction effect. The embedment of nanocrystallites on alumina support restricts advancing of crystal boundaries of zirconia, resulting in smaller crystal size for nanocomposites. Moreover, the zirconia nanocrystallites are evenly separated on the large out-surfaces of alumina nanofibres due to the strong interaction effect. The relatively large distance between each zirconia nanocrystallite also prevents the coarsing of zirconia.

3.4 CONCLUSION

In this Chapter, the synthesis of a series of 1D ZrO_2/Al_2O_3 nanocomposites with various Zr molar percentages from 5% to 50% was described. We demonstrated that zirconia macroporous materials can be fabricated using alumina nanofibres as hard-templates rather than using any space filler or pore-regulating agents. The incorporation of a great amount of zirconia nanocrystallites onto an alumina nanofibres framework also contributed new mesopores in the material, which results in a large surface area. In addition, the macroporous structures can be maintained irrespective of crystallite growth and phase change of zirconia when heated to 1000 °C.

The formation mechanism of the 1D ZrO_2/Al_2O_3 nanocomposite and relative zirconia macroporous material are proposed. When wet boehmite nanofibres are dispersed into butanol, these nanofibres link together to build up a 3D network on which a large amount zirconia (Zr molar percentage achieve 50%) can be deposited to prepare the 1D nanocomposite fibres. A macroporous material is naturally formed by the stacking of these

large 1D nanocomposite fibres. An effective and green approach is offered to create a novel zirconia macroporous material with large surface area and high thermal stability.

3.5 REFERENCE AND NOTES

(1) Landau, M. V.; Shter, G. E.; Titelman, L.; Gelman, V.; Rotter, H.; Grader, G. S.; Herskowitz, M. *Ind. Eng. Chem. Res.* **2006**, *45*, 7462.

(2) Giani, L.; Crstiani, C.; Groppi, G.; Tronconi, E. *Appl. Catal. B: Environ.* **2006**, *62*, 121.

(3) Gestel, T. V.; Vandecasteele, C.; Buekenhoudt, A.; Dotremont, C.; Luyten, J.; Leysen, R.; Bruggen, B. V. d.; Maes, G. *J. Membr. Sci.* **2002**, *207*, 73.

(4) Ozin, G. A. *Acc. Chem. Res.* **1997**, *30*, 17.

(5) Xu, H. H. K.; Quinn, J. B.; Takagi, S.; Chow, L. C. *Biomaterials* **2004**, *25*, 1029.

(6) Yuan, Z.; Su, B. *J. Mater. Chem.* **2006**, *16*, 663.

(7) Rolison, D. R. *Science* **2003**, *299*, 1698.

(8) Yu, J.; Yu, J. C.; Leung, M. K.-P.; Ho, W.; BeiCheng; Zhao, X.; Zhao, J. *J. Catal.* **217**, *217*, 69.

(9) Holland, B. T.; Blanford, C. F.; Stein, A. *Science* **1998**, *281*, 538.

(10) Davis, S. A.; Burkett, S. L.; Mendelson, N. H.; Mann, S. *Nature* **1997**, *385*, 420.

(11) Zhang, B.; Davis, S. A.; Mann, S. *Chem. Mater.* **2002**, *14*, 1369.

(12) Wierenga, A.; Philipse, A. P.; Lekkerkerker, H. N. W. *Langmuir* **1998**, *14*, 55.

(13) Korhonen, S. T.; Airaksinen, S. M. K.; Banares, M. A.; Krause, A. O. I. *Appl. Catal. A: Gen.* **2007**, *333*, 30.

(14) Korhonen, S. T.; Banares, M. A.; Fierro, J. L. G.; Krause, A. O. I. *Catal. Today* **2007**, *126*, 235.

(15) Persson, K.; Ersson, A.; Colussi, S.; Trovarelli, A.; Jaras, S. G. *Appl. Catal. B: Environ.* **2006**, *66*, 175.

(16) Lefferts, L.; Seshan, K.; Mojet, B.; Ommen, J. v. *Catal. Today* **2005**, *100*, 63.

(17) Miao, X.; Ben-Nissan, B. *J. Mater. Sci.* **2000**, *35*, 497.

(18) Choi, S. R.; Bansal, N. P. *Ceram. Int.* **2005**, *31*, 39.

(19) Holand, W.; Rheinberger, V.; Apel, E.; Ritzberger, C.; Rothbrust, F.; Kappert, H.; Krumeich, F.; Nesper, R. *J. Eur. Ceram. Soc.* **2009**, *29*, 1291.

(20) Kim, H.-W.; Shin, S.-Y.; Kim, H.-e.; Lee, Y.-M.; Chung, C.-P.; Lee, H.-H.; Rhyu, I.-C. *J. Biomater. Appl.* **2008**, *22*, 485.

(21) Chevalier, J.; Gremillard, L. *J. Eur. Ceram. Soc.* **2009**, *29*, 1245.

(22) Shen, S. C.; Ng, W. K.; Chen, Q.; Zeng, X. T.; Chew, M. Z.; Tan, R. B. H. *J. Nanosci. Nanotechno.* **2007**, *7*, 2726.

(23) Kloprogge, J. T.; Frost, R. L. *Phys. Chem. Chem. Phys.* **1999**, *1*, 1641.

(24) Shen, S. C.; Chen, Q.; Chow, P. S.; Tan, G. H.; Zeng, X. T.; Wang, Z.; Tan, R. B. H. *J. Phys. Chem. C* **2007**, *111*, 700.

(25) Li, G.; Li, W.; Zhang, M.; Tao, K. *Catal. Today* **2004**, *93-95*, 595.

(26) Jr, A. C. F.; Souza, K. R.; Camorim, V. L. D. L.; Cardoso, M. B. *Phys. Chem. Chem. Phys.* **2003**, *5*, 1932.

(27) Muller, E.; Oestreich, C.; Klemm, V.; Brendler, E.; Ferkel, H.; Riehemann, W. *Part. Part. Syst. Charact.* **2002**, *19*, 169.

(28) Jaenicke, S.; Chuah, G. K.; Raju, V.; Y, T. N. *Catal. Surv. Asia* **2008**, *12*, 153.

(29) Dongare, M. K.; Sinha, A. P. B. *J. Mater. Sci.* **1984**, *19*, 49.

(30) Scott, H. G. *J. Mater. Sci.* **1975**, *10*, 1527.

(31) Garvie, R. C. *J. Phys. Chem.* **1965**, *69*, 1238.

(32) Mokarl, T.; Sztrum, C. G.; Salant, A.; Rabani, E.; Banin, U. *Nature Mater.* **2005**, *4*, 855.

(33) Monte, F. d.; Larsen, W.; Mackenzie, J. D. *J. Am. Ceram. Soc.* **2000**, *83*, 628.

(34) Boumaza, A.; Favaro, L.; Ledion, J.; Sattonnay, G.; Brubach, J. B.; Berthet, P.; Huntz, A. M.; Roy, P.; Tetot, R. *J. Solid State Chem.* **2009**, *182*, 1171.

(35) Priya, G. K.; Padmaja, P.; Warrier, K. G. K.; Damodaran, A. D.; Aruldhas, G. *J. Mater. Sci. Lett* **1997**, *16*, 1584.

(36) Lee, S. W.; Sr, R. A. C. *J. Mater. Sci.* **1988**, *23*, 2951.

(37) Liu, D. W.; Perry, C. H.; Ingel, R. P. *J. Appl. Phys.* **1988**, *64*, 1413.

(38) Saha, S. K.; Pramanik, P. *J. Non-Cryst. Solids* **1993**, *159*, 31.

(39) Knozinger, H.; Ratnasamy, P. *Catal. Rev. Sci. Eng.* **1978**, *17*, 31.

(40) Turek, A. M.; Wachs, I. E. *J. Phys. Chem.* **1992**, *96*, 5000.

(41) Jung, K. T.; Bell, A. T. *J. Mol. Catal. A: Chem.* **2000**, *163*, 27.

(42) Cerrato, G.; Bordiga, S.; Barbera, S.; Morterra, C. *Appl. Surf. Sci.* **1997**, *115*, 53.

(43) Martinez, A.; Prieto, G.; Rollan, J. *J. Catal.* **2009**, *263*, 292.

(44) Sing, K. S. W.; Everett, D. H.; Haul, R. A. W.; Moscou, L.; Pierotti, R. A.; Rouquerol, J.; Siemieniewska, T. *Pure & Appl. Chem.* **1985**, *57*, 603.

(45) Kruk, M.; Jaroniec, M. *Chem. Mater.* **2001**, *13*, 3169.

(46) Pierre, A. C.; Pajonk, G. M. *Chem. Rev.* **2002**, *102*, 4243.

(47) Nakamoto, K. *Infrared and Raman Spectra of Inorganic and Coordination Compounds part B*; Wiley: New York, 1997.

(48) Tocchetto, A.; Glisenti, A. *Langmuir* **2000**, *16*, 6173.

(49) Deacon, G. B.; Phillips, R. J. *Coord. Chem. Rev.* **1980**, *33*, 227.

(50) Martens, W. N.; Frost, R. L.; Bartlett, J.; Kloprogge, J. T. *J. Mater. Chem.* **2001**, *11*, 1681.

(51) Vuurman, M. A.; Wachs, I. E. *J. Phys. Chem.* **1992**, *96*, 5008.

(52) Li, M.; Feng, Z.; Xiong, G.; Ying, P.; Xin, Q.; Li, C. *J. Phys. Chem. B* **2001**, *105*, 8107.

(53) Li, C.; Li, M. *J. Raman Spectrosc.* **2002**, *33*, 301.

(54) Sekulic, A.; Furic, K. *J. Mater. Sci. Lett.* **1997**, *16*, 260.

(55) Jehng, J.-M.; Wachs, I. E. *Chem. Mater.* **1990**, *3*, 100.

(56) Kwak, J. H.; Hu, J.; Mei, D.; Yi, C.-W.; Kim, D. H.; Peden, C. H. F.; Allard, L. F.; Szanyi, J. *Science* **2009**, *325*, 1670.

Chapter 4:

Sulfated 1D zirconia-alumina core-shell nanocomposites: a novel superacid catalyst with hierarchically macro-mesoporous nanostructure

Sulfated zirconia was first prepared and characterised by Hino *et al.* in 1979[1]. This catalyst is defined as a superacid because the acid strength of sulfated zirconia measured on the basis of its changing the color of a Hammett indicator at pK_a≤-14.52, is estimated to be H_0 ≤-16.04, and was considered 10000 times stronger than 100 % perchloric or sulfuric acid which is H_0 <-11.9. The solid superacid catalysts represent a new class of acid catalysts, because they can carry out reactions involving very strong acid site under mild temperatures[2,3]. They possess distinct advantages in catalyst separation and reactive-system maintenance, compared with traditional liquid catalysts such as HF and H_2SO_4 which cannot satisfy the stringent environmental restriction on waste disposal.

Several zirconium precursors have been reported for the preparation of sulfated zirconia, usually, the catalyst is prepared by first precipitating the hydroxide of zirconium which, after washing and drying, subsequently is treated with a solution of H_2SO_4 and followed by calcination. In the preparation procedures, the pH of precipitation of the hydroxide step[4], and the calcination temperature[5,6] are found to be particularly important for a high catalytic activity. The optimised calcination temperature is found at 600^{o}C~ 650^{o}C to give the highest intrinsic activity[5] corresponding to the formation of theoretical monolayer coverage by the sulfated species. Moreover, the treatment with other sulfurous species, such as $(NH_4)_2SO_4$, SO_2, H_2S, and SO_3 also promotes the catalytic activity[7]. Morterra and Cerrato[8] investigated the relationship between the crystal phase of zirconia and their exhibited catalytic activity,

and proposed that (i) the sulfation process usually occurs irrespective of sulfating agent; (ii) the zirconia must be tetragonal phase in the final catalyst while the catalyst as monoclinic zirconia is almost inactive; (iii) the catalyst must be activated by calcination at temperatures T≥ 800K at this temperature, the surface sulfates on tetragonal zirconia are corresponding to the structure 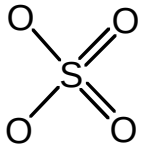 , in which the two S=O oscillators almost form at right angles to each other.

Pristine sulfated zirconia appears as a very promising solid acid catalyst for the replacement of the commercial acid catalyst; however, the catalyst is known to suffer significant deactivation in practical applications, possibly due to sulfur leaching or reduction at mild temperatures, active phase transformation from tetragonal phase to monoclinic phase, or the formation of coke on the surface of catalyst.

Mounting the sulfate zirconia on an alumina support[6] was proposed to constitute a more stable catalyst capable of resisting deactivation. However, it is hard to attain a high loading of zirconium species on this support because the particle aggregation during preparation and sintering during calcinations can sufficiently decrease the specific surface area, resulting in negative effect on catalytic activity[9]. Unfortunately, a small loading of zirconia cannot give rise to the highly active tetragonal zirconia[6,10].

Gao reported[11,12] that sulfated zirconia promoted by a small amount of alumina by co-precipitation exhibited excellent catalyst activity and also improved stability at the temperature higher than 250^{o}C for n-butane hydroisomarization. The roles of alumina were investigated by Goodwin Jr. and coworkers[13]. The increase in activity for n-butane isomerization was attributed to a significant increase in the concentration of active sites. Addition of Al_2O_3 also results in the formation of smaller crystallites of ZrO_2 which stabilize the active tetragonal phase of ZrO_2. The presence of smaller crystallite sizes of the tetragonal

phase of ZrO_2 after Al_2O_3-promotion affects the total surface area, sulfur content and the number of active sites.

However, the samples prepared by co-precipitation or sol-gel method have an inherent drawback. During the preparation of ZrO_2/Al_2O_3 nanocomposite, as a result of the homogeneous distribution of Zr and Al at atomic level, the addition of only a small fraction of aluminum by these methods will result in a significant elevation of calcination temperature for the phase transformation from the resultant amorphous precipitate to tetragonal ZrO_2 nanocrystallites. For example, as reported in Gao's papers [11,12], the addition of 15 mol% Al_2O_3 in the synthesis of Al_2O_3-promoted sulfated zirconia resulted in an amorphous material after calcination at 650 ^oC. The crystallizing temperature of this material had to be elevated to 750 ^oC to achieve tetragonal structure of zirconia, given the relatively low activity of the amorphous zirconia solid acid[14]. Nevertheless, things did not go as desired, such a high calcination temperature not only decomposed the sulfate species, but also resulted in a low surface area in this material[12]. Moreover, the increase of calcination temperature in such high temperature regions will bring about not only extremely large amounts of energy waste but also expensive investment in thermal insulation on an industrial scale.

In the previous chapter, we synthesised a series of 1D $ZrO_2@Al_2O_3$ nanocomposites. Tetragonal zirconia nanocrystallites were supported on long bundles of alumina nanofibres forming extremely long ZrO_2/Al_2O_3 composite nanorods with a new core-shell structure when the Zr molar percentage was > 30%. Naturally, the resultant materials are a hierarchically macro-mesoporous zirconia material: the evenly distributed ZrO_2 nanocrystallites result in mesoporous zirconia with large surface areas, while the stacking of such nanorods gives rise to a new kind of macroporous material. The stabilised and highly dispersed tetragonal zirconia nanocrystallites observed on 1D $ZrO_2@Al_2O_3$ nanocomposites and the unique property of tetragonal zirconia in catalytic application provide intense incentive to us to develop these nanocomposites into a series of novel catalysts. In this work,

these 1D ZrO_2@Al_2O_3 nanocomposites were developed as a series of 1D superacids with the Zr molar percentage X=100*Zr/ (Al+Zr) from 2 % to 50 % via sulfating procedure, followed by calcining at 650^oC.

Benzoylation of toluene with benzoyl chloride is an important strong acid-catalysed reaction for the manufacture of aromatic ketones, which are of important intermediates in the fine-chemical and pharmaceutical industries. The performances of many other solid acids, including zeolite[15], Nafion-H on silica[16], heteropolyacids[17] and some solid superacid[18] such as SO_4^{2-}/γ-Al_2O_3, SO_4^{2-}/ZrO_2 have been evaluated for this reaction. On sulfated zirconia, the product of the benzoylation of toluene with benzoyl chloride is a mixture of p-, o- and m-methylbenzophenone (scheme 1). The catalytic performances of the as-synthesised nanocomposites were tested for this reaction. The structure and physicochemical properties of the catalysts were characterised by means of XRD, IES, SEM equipped with EDX, ^{27}Al MAS NMR and the N_2 adsorption/desorption isotherms.

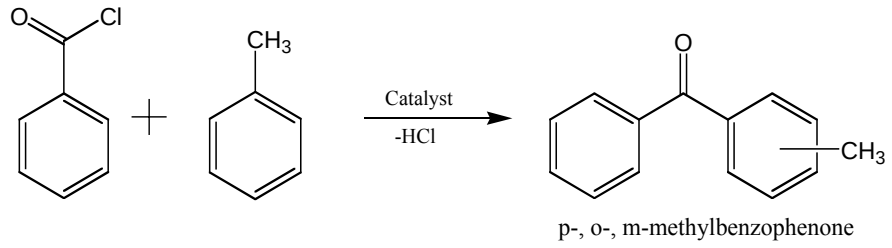

Scheme 1. Benzoylation of toluene with benzoyl chloride

4.1 EXPERIMENTAL SECTION

Materials: Boehmite fibres were synthesised by steam-assisted, solid wet-gel method as described in the literature[19]. Butanol was purchased from Ajax Finechem and zirconium (IV) butoxide solution (80 wt. % in 1-butanol) was purchased from Aldrich. All these chemicals were used as received.

Nanocomposite preparation: 1D zirconia-boehmite nanocomposites were synthesised by deposition of zirconia species on the boehmite nanofibres. In a typical procedure, 0.39 g boehmite nanofibres was added with 0.20g deionised water and then dispersed into 20 ml butanol under vigorous stirring. Zirconium (IV) butoxide was dissolved into the resultant mixture solution according to the Zr molar percentage X=100*Zr/(Al+Zr)= 2%, 5%, 10%, 15%, 30%, with stirring for 5 min. The nanocomposite with 50 % of Zr molar percentage was synthesised by the same procedure as mentioned above, except that 0.39g boehmite nanofibres was added with 0.40g deioned water, as the hydrolysis of additional zirconium butoxide consumes more water. Subsequently, the solutions were transferred into autoclaves for hydrothermal reaction at 170^{o}C for 24 hours. After cooling to room temperature, the resulting nanocomposites were separated by centrifugation, and then dried at 80^{o}C for 1 day.

Catalyst preparation: To prepare 1D superacids, as-synthesised 1D ZrO_2-boehmite nanocomposites with various Zr molar percentage were precalcined at 300^{o}C for 3 hours and re-dispersed into a 0.5 M H_2SO_4 solution (15 ml/g). After 30 min, the samples were separated by centrifugation and dried at 80^{o}C for 24 h, followed by calcination at 650^{o}C in air for 3 h. These sulfated 1D nanocomposites were labelled as S-Zr-"m", where m is Zr molar percentage.

For comparison, sulfated zirconia and sulfated alumina were chosen as reference catalysts. Sulfated zirconia was prepared according to the procedures in the literature[11,20]: Amorphous $Zr(OH)_4$ was prepared by dropwise addition of aqueous ammonia into a zirconyl solution until pH 9. After washing and drying, the sample was immersed in a 0.5 M H_2SO_4 solution for 30 min followed by separation from liquid phase. Without washing, the sulfated zirconia was dried at 80^{o}C and calcined at 650^{o}C in air for 3 h. The resulting catalyst was labelled as SZ. Sulfated alumina was prepared by immersing boehmite nanofibres into a 0.5 M H_2SO_4 solution for 30 min followed by separation from liquid phase. The sample was dried at 80^{o}C for 24 h, calcined at 650^{o}C for 3 h and labelled as SA-F.

Characterisation: *XRD patterns* were collected on a PANalytical X'Pert PRO X-ray diffractometer (radius: 240.0 mm). Incident X-ray radiation was produced from a line-focused PW3373/10 Cu X-ray tube, operating at 40kV and 40mA, providing a $K\alpha_1$ wavelength of 1.540596 Å. The incident beam passed through a 0.04 rad Soller slit, a ½ divergence slit, a 15mm fixed mask, and a 1° fixed antiscatter slit. After interaction with the sample, the diffracted beam was detected by an X'Celerator RTMS detector, which was set in scanning mode, with an active length of 2.022mm. Diffraction patterns for the samples were collected over a rage of 3~ 75^o 2θ. *Surface Area Analysis* based on N_2 adsorption/desorption techniques were performed on a Micrometrics Tristar 3000 automated gas adsorption analyser. Samples were pretreated at 200°C under the flow of N_2 for a minimum of 5 h on a Micrometrics Flowprep 060 degasser. *SEM micrographs* were obtained on a FEI QUANTA 200 scanning electron microscope operating at 30kV accelerating voltage with a 2.5 spot size. The samples were dried at room temperature and coated with gold under vacuum conditions in an argon atmosphere ionization chamber to increase surface conductivity. *FT-IR emission spectroscopy* was carried out on a Nicolet spectrometer modified by replacing the IR source with an emission cell. The description of the cell and principles of the emission experiment have been published elsewhere[21]. *Solid-state ^{27}Al MAS NMR spectra* were obtained from Varian Driver spectrometer operating at a resonance frequency of 104.26 Hz with a recycling time of 0.5 s. The spinning frequency was no less than 7 KHz. *Transmission electron microscopy was* carried out on a Phillips Tecnai F20 TEM. The instrument was equipped with a Field Emission Gun source operating at a High Tension of 200kV.

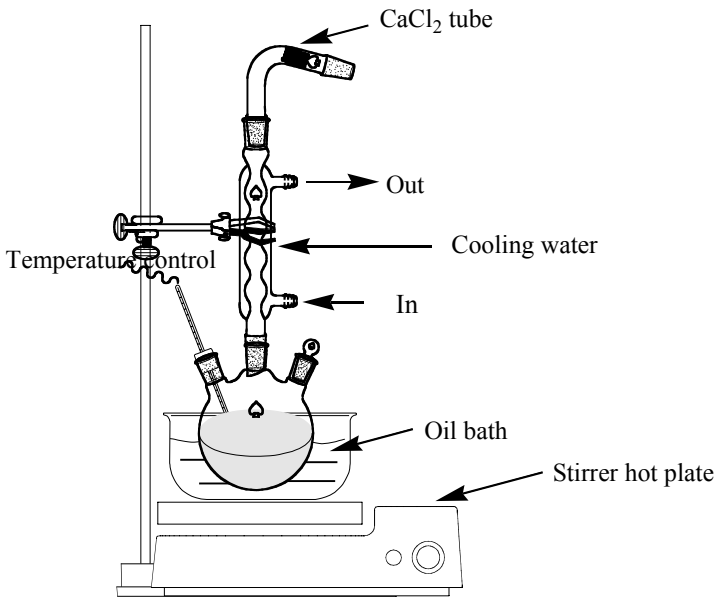

Scheme 2. Schematic diagram of catalytic reactor for Benzoylation of toluene with benzoyl chloride

Benzoylation reaction: Benzoylation of toluene with benzoyl chloride was used to investigate the catalytic activity of a series of 1D nanocomposite superacids. The reaction was carried out in a round-bottom flask equipped with a reflux condenser connecting with a $CaCl_2$ tube which is used to keep the reaction system free of moisture (Scheme 2). Before reaction, all catalysts were freshly calcined at 500 ^oC for 2.5 hours and cooled down to ambient temperature in an argon atmosphere in order to remove the adsorbed water molecules on the surfaces of the catalysts. 0.4 ml benzoyl chloride, 8 ml toluene and 0.2 g catalysts were charged into the reactor which was heated to reflux (*ca*. 110^oC) in an oil bath under magnetic stir. Samples were collected at some specific intervals and immediately analysed by gas chromatography. Quantitative results were obtained by comparing the results with the calibration from synthetic mixtures. Since toluene was in excess, the yields of methylbenzophenone were based on the benzoyl chloride added into the reaction.

4.2 RESULTS

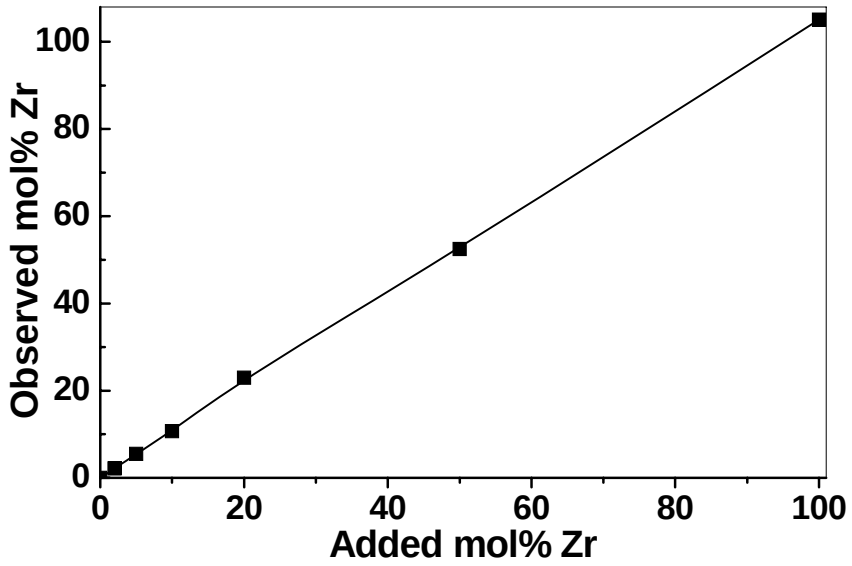

Figure 1. Observed Zr percentage in samples as a function of nominal Zr percentage

The overall compositions of all the 1D nanocomposites prepared with various Zr/Al molar ratios were examined by EDX equipped on SEM. The area selected was approximately 0.04 mm^2 at each run, and at least five different spots were selected for each sample to get an average value of the composition. As shown in Figure 1, the observed Zr percentage is equal to the nominal molar ratio, indicating all of zirconium precursor were precipitated from the mixture solution and deposited on the boehmite nanofibres.

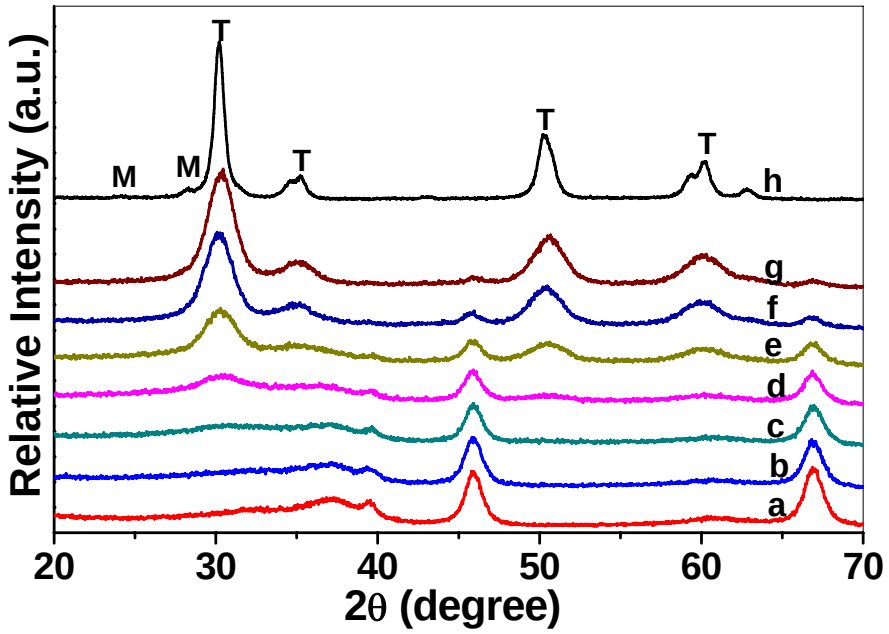

Figure 2. XRD patterns for the sulfated 1D zirconia-alumina nanocomposites, alumina nanofibres and zirconia obtained by calcining at 650°C for 3 h. (a) sulfated alumina nanofibres (b) S-Zr-2, (c) S-Zr-5, (d) S-Zr-10, (e) S-Zr-15, (f) S-Zr-30, (g) S-Zr-50 and (h) sulfated zirconia. M and T represent monoclinic phase and tetragonal phase, respectively. The patterns in (H) underwent a 0.6-fold Y-scale reduction

The XRD patterns of the sulfated 1D zirconia-alumina nanocomposites obtained by calcining at 650°C for 3 h are shown in Figure 2. The phase of sulfated alumina nanofibres illustrates the γ-Al_2O_3 structure. The peaks at 45.8 and 66.8 °2θ correspond to the diffractions from (400) and (440) planes of γ-Al_2O_3. For pristine sulfated zirconia, a small portion of the monoclinic phase presents, along with the tetragonal phase. The peaks at 30.2, 35.3, 50.3 and 60.1 °2θ are attributed to the diffractions of (101), (110), (112) and (211) planes of tetragonal zirconia while the peaks at 24.5, 28.2 °2θ are the diffractions from (-110) and (-111) planes of monoclinic zirconia. In contrast, for these sulfated 1D nanocomposites, as Zr molar percentage is higher than 10 %, the nanocrystallites of tetragonal zirconia can be detected by the appearance of a broadened peak at ca. 30°. The intensity of this diffraction as well as others for tetragonal zirconia increase with the corresponding increase in the percentage of zirconia, but no peak corresponding to monoclinic zirconia is present in the patterns for these

nanocomposites. Meanwhile, the diffraction peaks for γ-Al_2O_3 gradually decrease and become undetectable at 50 mol% of Zr due to the reduction of relative concentration of the γ-Al_2O_3 and its inherrently poor intensity.

The primary crystallite size of the tetragonal zirconia in these samples (including the pristine sulfated zirconium and 1D ZrO_2/Al_2O_3 superacid) are calculated by the Scherrer equation and listed in Table 1. It can be observed that the increase of Zr molar percentage from 10 % to 50 % results in the increase of crystal size from 2.1 nm to 4.5 nm in (101) direction, which are much smaller than that of the pristine sulfated zirconium at 12 nm. As we previously reported in Chapter 3, the alumina nanofibres can retard the crystallite-size growth of zirconia and therefore retard the transformation of zirconia from a metastable tetragonal phase to a monoclinic phase because metastable tetragonal zirconia is stable in small crystal size.

Table 1. Crystallite dimension in (101) direction for sulfated tetragonal zirconium and that deposited on alumina nanofibres with various zirconia content (The data were derived from X-ray diffraction patterns)

Sample name	Peak position (^{o}2θ)	FWHM (^{o}2θ)	Crystallite dimensions(nm)
Sulfated zirconium	30.14	0.684	12.0
S-Zr-50	30.28	1.832	4.5
S-Zr-30	30.12	2.086	3.9
S-Zr-15	30.34	3.057	2.7
S-Zr-10	30.38	4.000	2.1

Figure 3 shows the ^{27}Al MAS NMR spectra of the sulfated 1D nanocomposites. Although it is possible that some spectral components cannot be distinguished due to peak broadening, some species can be clearly identified via fitting procedures, as shown in Figure 4. The

intense signal at *ca*. 5 ppm corresponds to octahedral aluminium Al_{octa} sites (AlO_6), while the relatively weak resonances at around 67 ppm indicated the presence of tetrahedral aluminium Al_{tetra} sites (AlO_4)[22]. These two resonances correspond to the two coordination states of Al in γ-Al_2O_3 crystal structure[23,24], which complements XRD results of these nanocomposites. Therefore, the alumina phase in S-Zr-50 can be confidently identified as γ-Al_2O_3. For all the samples, the resonance peaks corresponding to the AlO_6 are remarkably asymmetric, and a tail in spectra from 0 to -25 ppm can be observed. The tail could be due to the presence of new Al octahedral sites, namely $Al_{octa\text{-}O\text{-}S}$ or $Al_{octa\text{-}O\text{-}Zr}$, where S or Zr is located in the second coordination shell of aluminium[25]. In addition, with the increase in Zr content, a resonance between two main peaks centred at about 37 ppm becomes more pronounced. This component has been assigned to penta-coordinated aluminium Al_{penta} sites (AlO_5)[26].

It is worth mentioning here that, in this work, γ-Al_2O_3 is prepared via the phase transformation of boehmite phase which only contains octahedral aluminium Al_{octa} sites (AlO_6). Obviously, both of AlO_4 and AlO_5 sites are created by the dehydration and dehydroxylaton of AlO_6 at elevated temperature. In Table 2, the relative percentages of the AlO_4, AlO_5 and AlO_6 are listed for the sample with increasing Zr molar percentages. It shows that the AlO_5 sites increase at the expense of both AlO_6 and AlO_4 sites, and the AlO_6 site decreased more rapidly than the AlO_4 site. The enhancement of AlO_5 sites with the increase in Zr molar percentages suggests that the penta-coordinated aluminium site is correlated to the surface interaction of zirconia with alumina. Nevertheless, it is worth mentioning that the percentage of AlO_5 sites was not directly affected by the Zr content. For the sample S-Zr-10, the percentage of AlO_5 sites is slightly lower than that for the samples S-Zr-2 and S-Zr-5. Presumably, this is because at 10 mol% of Zr content, zirconia species transferred into tetragonal nanocrystallites and the Al-O-Zr sites reduced due to the aggregation of zirconia species. Therefore, it is possible that when zirconia species is in a highly dispersed state (S-Zr-2, S-Zr-5), the samples possess more AlO_5 sites.

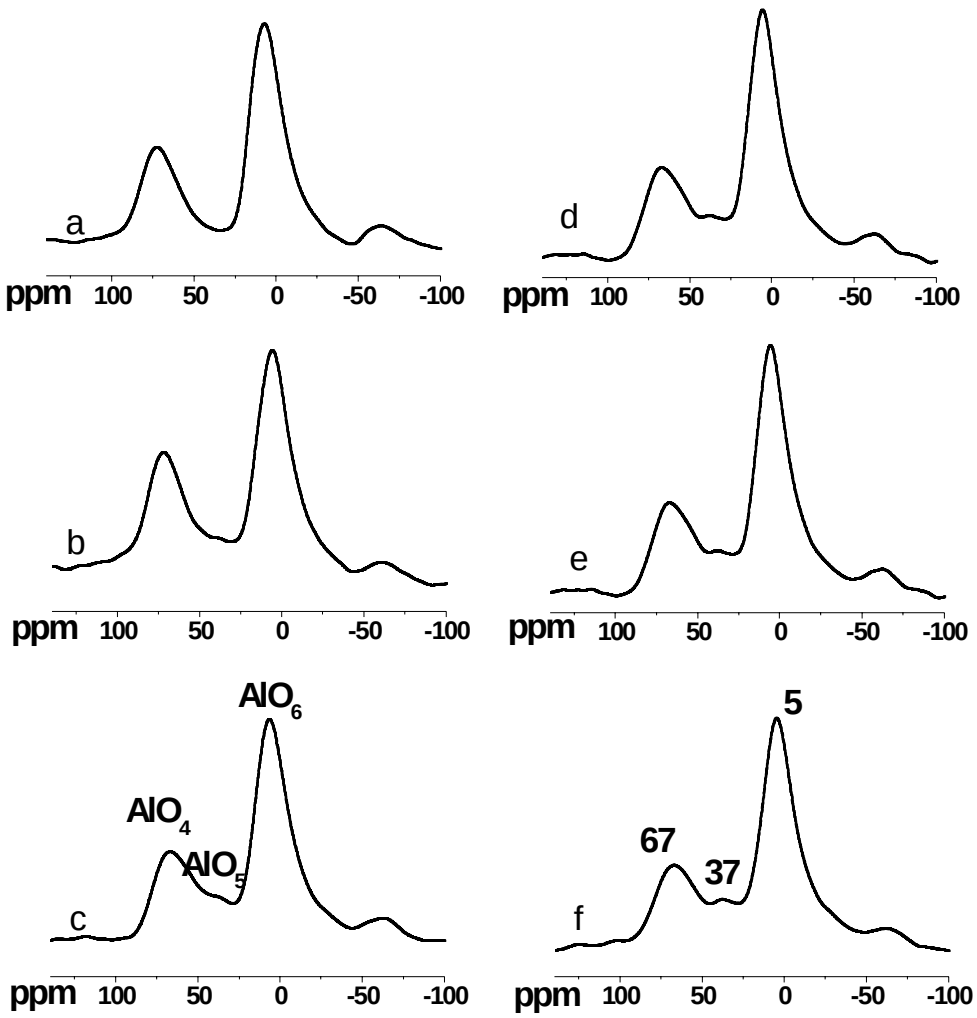

Figure 3. ^{27}Al MAS NMR spectra of sulfated pristine alumina nanofibres and 1D ZrO_2/Al_2O_3 nanocomposites obtained by calcination at 650°C: (a) SA-F; (b) S-Zr-2; (c) S-Zr-5; (d) S-Zr-10; (e) S-Zr-15; (f) S-Zr-30

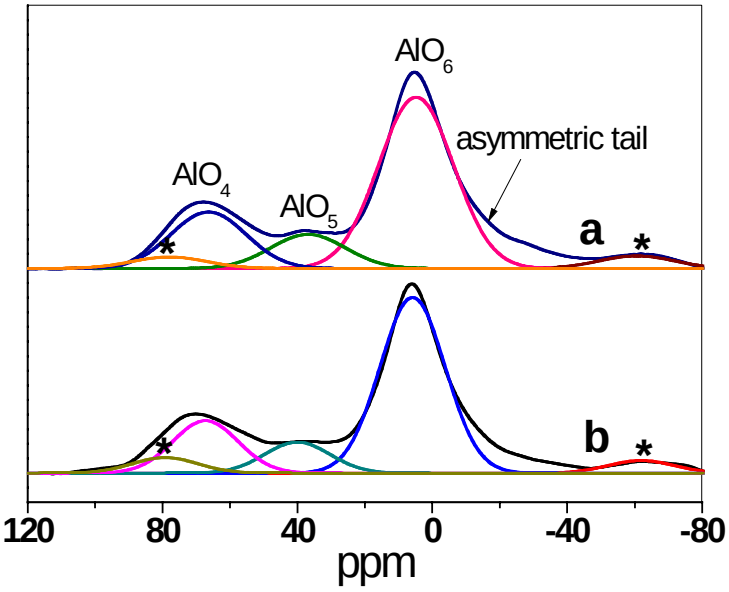

Figure 4. Separated components of (a) S-Zr-30; and (b) S-Zr-50 obtained by spectrum fitting procedure. *quadrupolar sideband

Table 2. The relative percentages of the AlO_4, AlO_5 and AlO_6 species for the nanocomposites with various Zr content (obtained by spectrum simulation procedure)

Sample name	AlO_6	AlO_5	AlO_4
SA-F	74.8%	0	25.2%
S-Zr-2	65.9%	6.7%	27.4%
S-Zr-5	66.1%	10.5%	23.4%
S-Zr-10	68.3%	7.6%	24.1%
S-Zr-15	67.1%	11.8%	21.2%
S-Zr-30	63.2%	13.8%	23.0%
S-Zr-50	62.1%	14.6%	23.3%

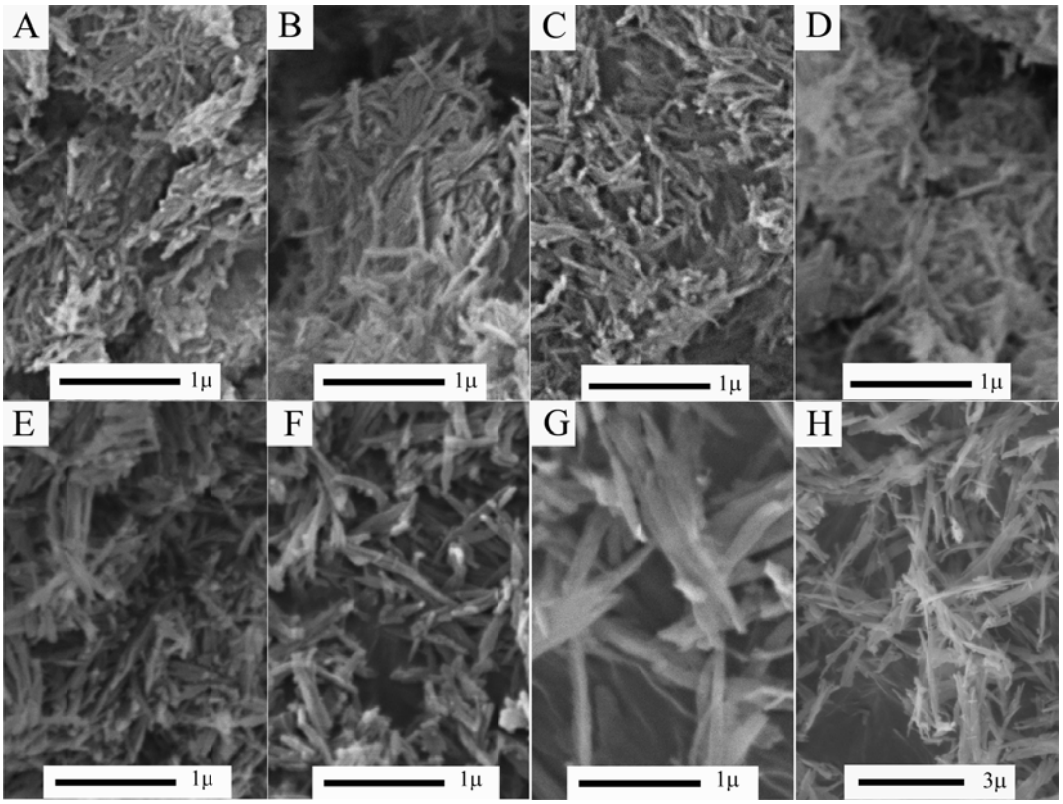

Figure 5. SEM images of sulfated pristine alumina nanofibres and 1D ZrO_2/Al_2O_3 nanocomposites obtained by calcination at 650°C: A) SA-F; B) S-Zr-2; C) S-Zr-5; D) S-Zr-10; E) S-Zr-15; F) S-Zr-30; G) S-Zr-50; H) S-Zr-50 at a larger scale

Particle morphology is investigated by SEM (See Figure 5). The image for sulfated pristine alumina nanofibres shows many entangled worm-like particles. The 1D morphology of this material generates large inter-particle voids, which are referred to as porosity of this material. Importantly, after the sulfating procedure and calcination, the material also maintains its morphology and the fibrous morphology can be clearly observed from SEM images for all the sulfated catalyst. This structural stability is probably a result of the starting material, boehmite nanofibres, being relatively stable in sulfuric acid solution. As reported in last chapter, this nanostructure is constituted by a singular or small bundle of nanofibres as a hard template and is further fixed by the zirconia shell. This zirconia shell is essential to maintain the integrity of the 1D nanocomosites fibres. Therefore, short and thin nanofibres formed at low zirconia coverage and relatively large nanorods are observed when Zr

percentage is higher than 15 %. The porosity and pore volumes of these nanocomposites are dependent on the diameter and length of their constituted nanorods. Consequently, with the increase of Zr molar percentage, the macroporous framework resulting from specific morphology of 1D nanomaterials are also gradually extended.

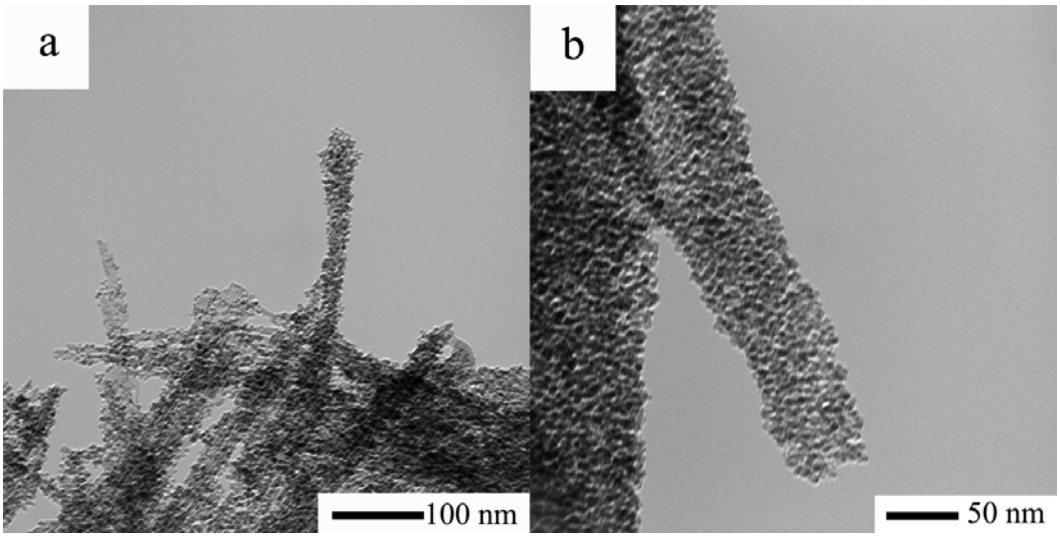

Figure 6. TEM image for a) S-Zr-30 and b) S-Zr-50 superacid

The transmission electron microscopy (TEM) images of S-Zr-30 and S-Zr-50 are illustrated in Figure 6. Such superacids exhibit a novel fibrous morphology where sulfated tetragonal zirconia looks like irregular squares covering the alumina bundles. It can be observed that even at 30 mol % Zr content the sulfated tetragonal zirconia is still insufficient to cover the entire outer surface of alumina bundles while only at 50 mol % of Zr the bare alumina bundles are fully covered, indicating that the outer surface of alumina bundles can bear an extremely large Zr content.

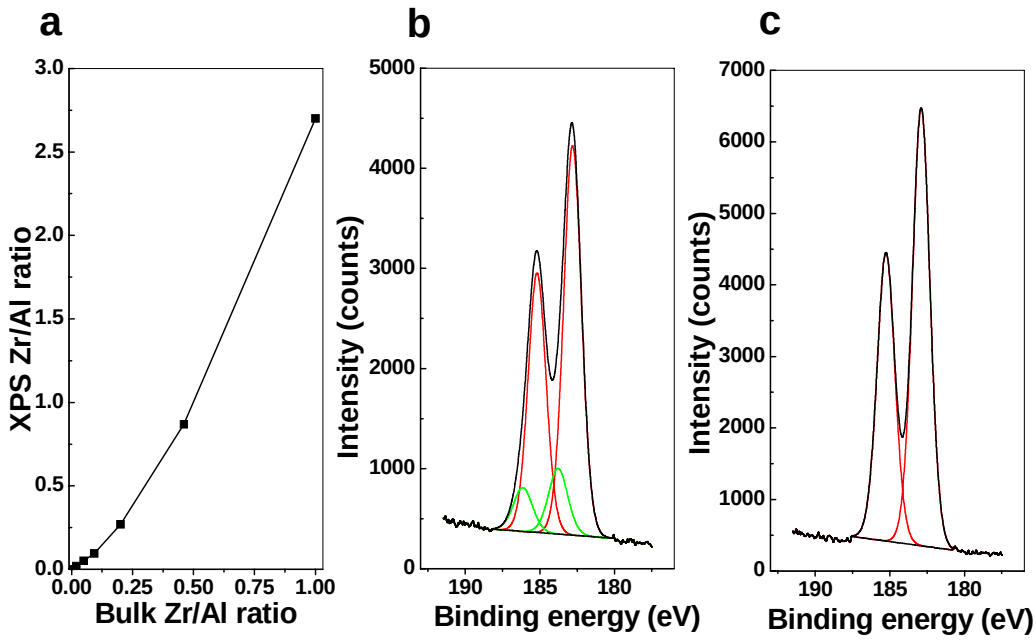

Figure 7. XPS results a) XPS surface Zr/Al molar ratio as a function of bulk Zr/Al molar ratio, b) Zr 3d XPS spectra of S-Zr-30 and c) Zr 3d XPS spectra of S-Zr-50

XPS analysis of pristine sulfated zirconia and all ZrO_2/Al_2O_3 nanocomposites was investigated and all samples were measured after crushing. Figure 7a shows the Zr/Al XPS surface atomic ratios as a function of the corresponding overall ratios measured by EDX. When Zr molar percentage is equal to or less than 15%, the XPS ratios are very close to the bulk ratios. Above this value, the XPS surface ratio gradually becomes much higher than bulk ratio. Especially for the S-Zr-50, of which the bulk Zr/Al molar ratio is 1:1, the XPS surface ratio is close to 3:1, indicating that the Zr species is concentrated on the outer surface of alumina nanobundles.

In addition, for S-Zr-50, the $Zr3d_{5/2}$ photopeak is centred at binding energy of 182.9 eV (Figure 7c), and only one chemical environment of Zr could be detected, which is same with the result for pristine sulfated zirconia reported in the literature[27]. The interaction between the ZrO_2 species and Al_2O_3 support can only be detected when Zr molar percentage is lower than 30 %, and the Zr3d photopeaks can be decomposed into two components (Figure 7b). The binding energy of $Zr3d_{5/2}$ for one component is same as pristine sulfated zirconia, and

the other exhibits a displacement for the bonding energies of $Zr3d_{5/2}$ of 0.9 eV, to about 183.8eV. This displacement has been associated with the formation of Zr-O-Al-type bonds[28]. The ratio of latter component increased with the decreasing of zirconium content, which is summarised in Table 3.

Table 3. The binding energies of $Zr3d_{5/2}$ photopeak corresponding to two kinds of Zr species and their relative ratio in XPS spectra

Sample	Zr $3d_{5/2}$			
	ZrO_2	Percentage	Zr-O-Al	Percentate
S-Zr-50	182.9	100 %	———[a]	———[a]
S-Zr-30	182.9	85 %	183.8	15 %
S-Zr-15	182.9	63 %	183.8	37 %
S-Zr-10	182.9	63 %	183.8	37 %
S-Zr-5	183.0	60 %	183.8	40 %
S-Zr-2	183.0	52 %	183.8	48 %

[a] Cannot be detected by XPS

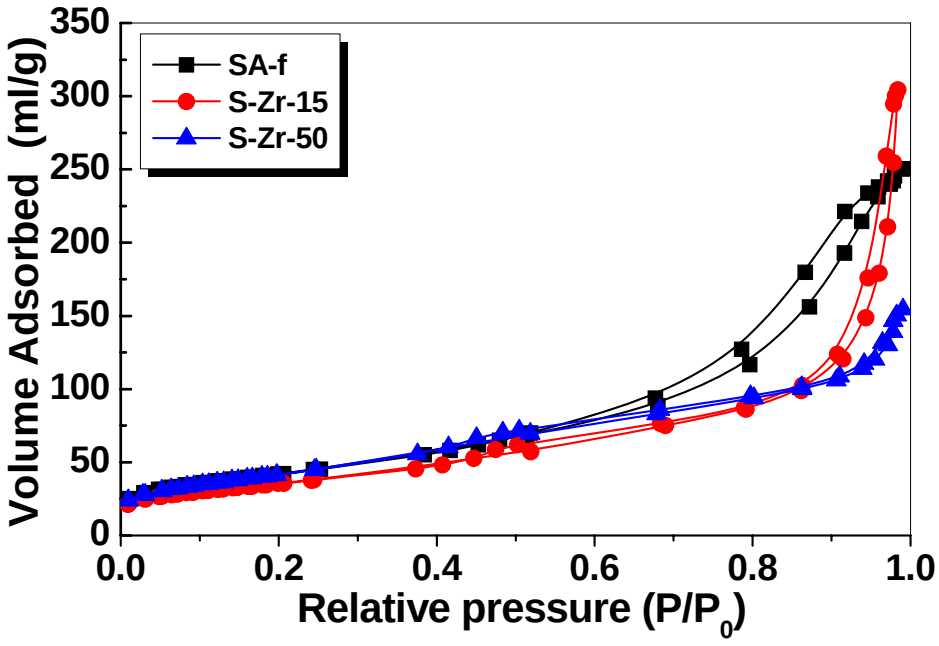

Figure 8. Nitrogen adsorption and desorption isotherms for some representative samples with various Zr content

The BET surface areas and pore structure of these catalysts are determined by nitrogen adsorption-desorption isotherms. Figure 8 shows those for representative samples to illustrate the textural changes with the increase of the Zr molar percentage. Accordingly, all the isotherms show a type IV characteristic feature of isotherm, which indicates the samples examined are full of mesopores[29]. For S-Zr-50, the isotherms at high P/P_0 show a type II characteristic feature, which is often obtained with a macroporous material. The hysteresis of the three samples seems quite different. The hysteresis loop of the sulfated alumina nanofibre falls within H3 and H4 categories, which, according to Sing's study[30], should be a result of slit-like pores constructed by plate-like particles. However this sample has the morphology of nanofibres. Therefore, the arrangement of nanofibres must also give rise to this kind of loop. The hysteresis for S-Zr-15 exhibits a loop with two steps: at high P/P_0 from 0.8 ~1.0, the hysteresis loop is close to H3, which show a higher slope ratio indicating wide slit-like pores; another step of hysteresis loop remains nearly horizontal over a wide range of P/P_0 from about 0.42 ~ 0.8, which is similar to the type H2 loop associated with bottle ink

pore or pore networks[31]. The former part is produced by the stacking of fibrous particles; the latter part is generated by the coating of zirconia nanocrystals and also observed for the sample S-Zr-50. For S-Zr-50, the adsorption branch and desorption branch overlapped at P/P_0 from 0.8~1.0, and its isotherm becomes a combination of type II and IV adsorption, indicating that the nanocomposite contains both mesopores and macropores[30].

The pore size distributions of as-synthesised nanocomposites, which are estimated from the adsorption branch of the isotherm, also changed with the increasing of Zr content. Sample SA-F has a wide pore-size distribution from 1 nm to 100 nm, which is the characteristic feature of pores arising from the inter-crystallite void constructed by nanofibres. All nanocomposites show two distributions from 1-8 nm and above 10 nm, respectively. The former distribution is attributed to the pores formed by incorporation of zirconia species and the latter one is assigned to those formed due to their 1D morphology. It can be observed that the distribution from 1-8 nm gradually increases, while the latter distribution is shrinking with the increasing of Zr content. At 50 mol% of Zr, pore size mainly distributes in the range from 2-8 nm, and the inter-particle void resulting from fibrous nanostructure are almost disappeared. This phenomenon was also observed in our previous work in last chapter and is due to the porous frameworks constructed when these 1D nanocomposites gradually expand, as the increase of Zr mol% enhances the structural integrity (length and diameter) of the resultant nanorods, leading most of macropores to exceed the measurable range for N_2 physisorption.

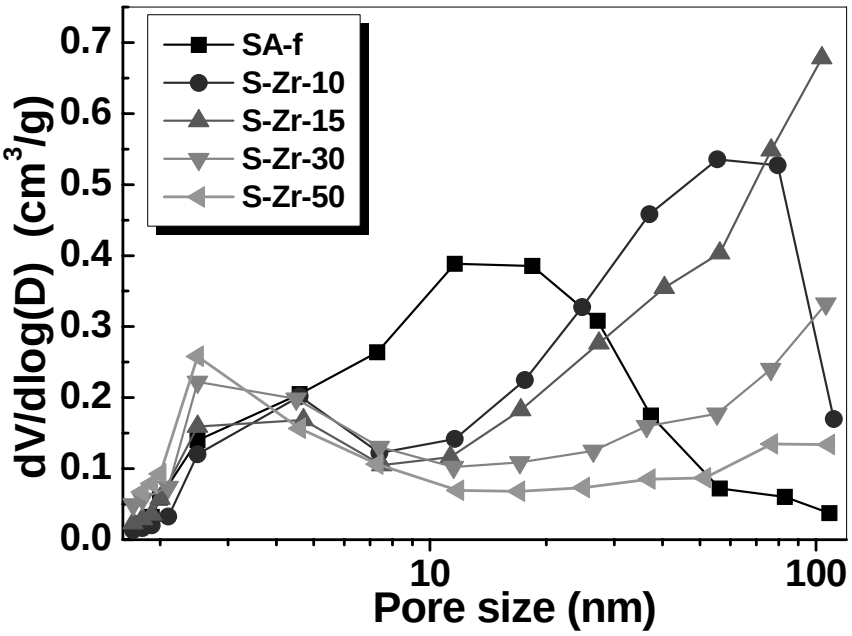

Figure 9. Pore size distributions for samples with various Zr content

The main textural parameters for sulfated samples after calcination at 650°C and original boehmite nanofibres are listed in Table 4. Many literature reports confirmed that loading even a small amount of zirconia on alumina would result in a decrease in surface area, and most prominently, when zirconia crystal phase began to occur, the surface area dramatically decreases below 100 m^2/g[6,10,32]. However, interestingly, in this work, samples with differing zirconia loading on alumina nanofibres actually maintained a relatively constant high specific surface area. The specific surface areas for all as-synthesised nanocomposites are from 125 to 154 m^2g^{-1}. In contrast, the pristine sulfated zirconia is about 88 m^2g^{-1}, similar to the reports in the litearture[33]. The sulfated alumina nanofibres exhibited a similar surface area, average pore size and pore volume to original boehmite nanofibres.

Table 4. Powder properties of the sulfated 1D ZrO_2/Al_2O_3 nanocomposites with various Zr molar percentage and sulfated alumina nanofibres obtained by calcination at 650°C

Sample	BET surface area($m^2g^{-1)}$	Average pore size (nm)	Pore volume (cm^3/g)
Boehmite nanofibres	158	13.32	0.525
SA-F	152	10.16	0.387
S-Zr-2	138	16.42	0.565
S-Zr-5	131	16.47	0.540
S-Zr-10	125	15.74	0.491
S-Zr-15	128	14.67	0.471
S-Zr-30	154	8.26	0.318
S-Zr-50	153	6.25	0.239
SZ	88	7.69	0.169

Figure 10 shows the Fourier transform infrared emission spectroscopy (IES) of sulfated ZrO_2/Al_2O_3 nanocomposite (S-Zr-50) from 50°C to 350°C. According to the literature, the surface sulfur complexes formed by the interaction of metal oxides with sulfate ions, after evacuation above 350°C, exhibit a strong band at 1382~1391cm^{-1} in mid-infrared spectroscopy which is assigned to S=O stretching vibration[11,34]. This band has a strong tendency to reduce its wavenumber with the adsorption of basic molecules such as H_2O. This wavenumber shift, corresponding to a decrease in the bond order of S=O covalent bond and an increase in the partial charge on oxygen atom[34], is associated with the acid strength of the catalyst, where larger wavenumber shifts correspond to higher acidity. Measuring the

wavenumber shift of S=O by infrared spectra is regarded as a recommended method to detect the relative acid strength of the sulfated oxide catalysts[11,12], because some traditional techniques, such as temperature-programmed desorption[35,36] and IR study of pyridine adsorption[37] inevitably misestimate the acidity of this kind of material.

Moreover, IES can measure the vibration wavenumbers of the samples *in-situ* at elevated temperature, which avoids the re-adsorption of water molecules on the surfaces of materials, just after dehydroxylation, due to exposure to air in either the quenching or infrared measurement step. As shown in Figure 10, the IES of S-Zr-50 at 50 ^{o}C shows S=O bonds vibration centred at 1350 cm^{-1} and a broad band near 1630 cm^{-1} corresponding to the bending vibrations of the surface water and hydroxyl group, which can be observed at the same time. As the heating temperature increases, the S=O bonds vibration become stronger and shifts from 1350 at 50 ^{o}C to 1391 cm^{-1} at 350 ^{o}C. At this temperature, the hydroxyl group bonding vibrations almost disappear. Notably, in this work, the band position corresponding to the stretching vibration of S=O bond of sulfated zirconia obtained at 350 ^{o}C agrees well with that of the same sample previously described in Gao‘s work[12] which was detected by infrared absorption spectroscopy at room temperature after evacuating at 350^{o}C. This indicates that this S=O wavenumber shift obtained by IES is due to the dehydrolysis of samples rather than the change of measuring temperature.

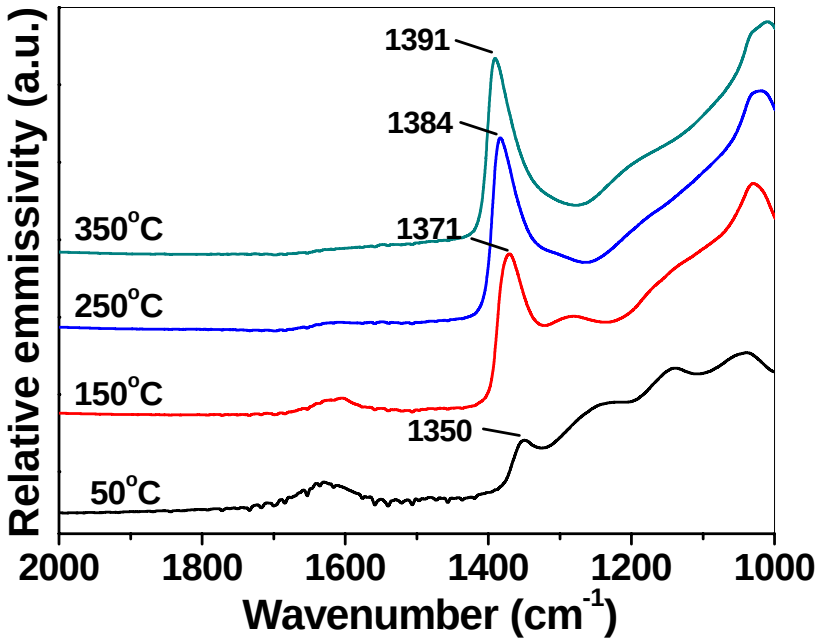

Figure 10. Infrared emission spectra of S-Zr-50 in the region 1000~ 2000 cm^{-1} from 50°C to 350°C at 100°C intervals

Obviously, the spectra obtained at 50°C represent the situation that the water is absorbed on the sulfated catalyst, and those obtained at 350°C correspond to the samples previously evacuated at 350°C. According to literature[11], the relative acid strength of sulfated 1D ZrO_2/Al_2O_3 nanocomposites with different Zr molar percentage can be detected by measuring the S=O shifts from 50°C to 350°C based on the IES results. The S=O stretching wavenumber, the bond order and partial charge on oxygen atom calculated according to formulations in the literature[34] for the series of sulfated ZrO_2/Al_2O_3 nanocomposites with different Zr molar percentage are presented in Table 5.

Although there is a slight deviation between this work and Gao's work due to the use of different experimental technology, it can be clearly observed that the S=O shifts of this series of samples increased with the increase of zirconia loading from 0 to 50%. On the other hand, when Zr content is 50%, the shift of S=O stretching is almost identical with that of the sulfated zirconia, indicating similar relative acid strength between S-Zr-50 and SZ. The

relative acid strengths are in the order of SA-F <S-Zr-2 <S-Zr-5 <S-Zr-10 <S-Zr-15 <S-Zr-30 < S-Zr-50 ≈SZ.

Table 5. Effect of Water Adsorption on S=O including Stretching Wavenumber, Bond Order and Partial Charge on Oxygen

Sample	S=O Wavenumber(cm^{-1})			Bond order		Partial charge on oxygen	
	B[a]	A[b]	Shift	B	A	B	A
SA-F	1378	1351	27	1.84	1.80	-0.16	-0.20
S-Zr-2	1380	1350	30	1.85	1.80	-0.15	-0.20
S-Zr-5	1382	1350	32	1.85	1.80	-0.15	-0.20
S-Zr-10	1384	1350	34	1.86	1.80	-0.14	-0.20
S-Zr-15	1387	1350	37	1.86	1.80	-0.14	-0.20
S-Zr-30	1389	1350	39	1.86	1.80	-0.14	-0.20
S-Zr-50	1391	1350	41	1.86	1.80	-0.14	-0.20
SZ	1391	1350	41	1.86	1.80	-0.14	-0.20
SZ[c]	1392	1352	40	1.87	1.80	-0.13	-0.20

[a] Before water adsorption; measured at 350°C

[b] After water adsorption; measured at 50°C

[c] Date from Gao's work in Ref 12.

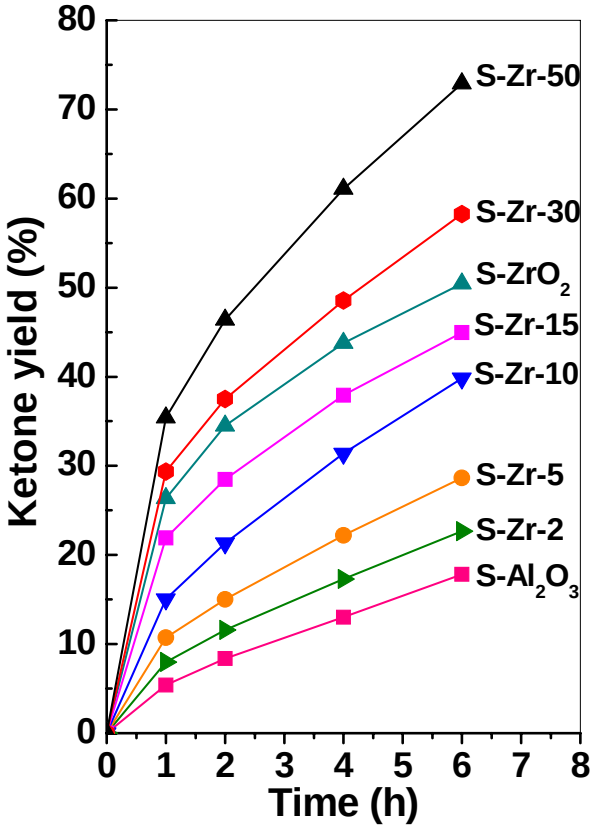

Figure 11. Benzoylation of toluene at 110°C

Benzoylation of toluene with benzoyl chloride is used to investigate the liquid acid-catalytic activity of as-synthesised 1D superacids. For all these nanocomposite catalysts, the products of the benzoylation reaction of toluene are a mixture of p-, o- and m-methylbenzophenone, respectively, which is 67~69% of p-methylbenzophenone, 27~ 29% of o-methylbenzophenone, and 3~ 4% of m-methylbenzophenone.

The catalytic activities of samples with different zirconia content are illustrated in Figure 11. The temperature of the reaction system is stabilised at 110 °C. From Figure 11, it can be observed that when Zr content is up to 5%, the ketone yield is less than 25% for 6 hours, but it is about 10 % higher than that of the sulfated pristine alumina nanofibres. As Zr content increases to 10%, the catalytic activity dramatically rises. The activity of the composite exceeds sulfated pristine zirconia at or above 30% Zr molar percentage. The overall tendency is that the catalytic activities increase with the increase in zirconia amount from 2%

to 50%. It is believed that benzoylation reaction only proceeds on the superacidic sites which are strong enough for the generation of the intermediate reaction, $PhCO^+$ cation[38]. Combined with IES results, catalytic performances unambiguously exhibit the correlation between acidities and activities. Thus, for these catalysts with similar surface areas, the stronger acidity present the higher the catalytic activity is. Taking the XRD results into account, tetragonal zirconia started to form until the Zr mol% was above 10%, and with increasing the Zr mol% the amount of tetragonal zirconia in the samples increased. This result, which coincides with the activities of samples, suggests the increase of tetragonal zirconia might be related to the enhancement of surface acidity of the catalyst.

4.3 DISCUSSION

In last chapter, we has investigated the formation mechanism of 1D ZrO_2/Al_2O_3 nanocomposites, and revealed that the tetragonal zirconia nanocrystallites evenly surround the long bundle of boehmite nanofibres forming a core-shell structure. In this work the sulfation process only inflicts a negligible effect on the fibrous morphology of these nanocomposites with this effect also being minimized by the increase of zirconium coverage. Therefore, these zirconia nanocomposites with hierarchically macro-mesoporous nanostructures successfully develop into a novel class of solid surperacid.

An interesting result of these as-synthesised nanocomposite catalysts is that their specific surface areas are maintained with Zr molar percentage varying from 2 % to 50 %. This is quite different from the published data, in which it was reported that loading a heavy metal oxide on a porous carrier will result in the significant decrease of specific surface areas for resulting composites, especially when the concentration of the loading species was high enough to generate some small independant nanocrystallites, and that the surface areas would severely decrease under 100 m^2/g. The reason for this phenomenon in traditional porous carriers is presumably because some of the nanocrystallites block the orifices of porous materials[39].

In this work, the zirconium species are loaded on the long bundle of alumina nanofibres composing a 1D core-shell structure with zirconium species concentrated on the outer-surface of these 1D nanocomposites. At high Zr percentage, the growth and distribution of tetragonal zirconia nanocrystallites on fibrous cores at elevated temperatures spontaneously forms a mesoporous layer with pore size from 1 nm to 10 nm rather than plugging the orifices as has been observed previously. These small zirconia nanocrystallites can provide a large specific surface area; therefore, in spite of the specific surface reduction caused by overlapping of the interface between zirconia nanocrystallites and alumina nanofibres, overall, the surface area of these nanocomposties will not significantly decrease. Indeed, it is confirmed by our experiments: at low Zr percentage, zirconia species are highly dispersed on the surface of γ-Al_2O_3 in a spontaneous process[40], and the surface area of nanocomposites slightly decreases due to the increase of apparent density; however, with the Zr content increasing so it is high enough to generate zirconia nanocrystallites, new surface is also generated by the occurrence of tetragonal zirconia nanocrystallites leading to the increase of the surface areas. At this situation, the materials can bear an extremely large loading ratios and their surface area and pore size seems to be independently modified. This can provide an effective approach to design a catalyst with a desired nanostructure. For instance, the existence of interconnected macroporous framework should efficiently transport guest molecules to the reactive sites, increase the resistance to sintering of this material at elevated temperatures and minimize the aggregation of zirconia nanocrystallites. As for this reaction, the catalytic performance is mainly determined by the acid strength and surface area of as-synthesised nanocomposites with no evidence showing that the pore size and porous framework exerted any effect on the catalytic performance. Since all of the nanocomposites catalysts possess similar surface areas, it leads us to conclude that the relationship between the acid strength and catalytic activity is such that the pristine sulfated alumina nanofibres only contributed lower activity, and that the increase in Zr percentage gradually increases the relative acid strength. Consequently, an increase in the catalytic activity of benzoylation of toluene was observed. It is worth mentioning that the acidity for the sample with 30 % Zr

molar percentage is slightly weaker than that of pristine sulfated zirconia, but compared with pristine sulfated zirconia, this sample possesses a larger surface area which is 154 m^2g^{-1}(reference catalyst is only 88 m^2g^{-1}). The smaller tetragonal nanocrystals of about 3.9 nm attached on alumina nanofibres can generate more eligible active sites for this catalytic reaction. Above this Zr molar percentage, the nanocomposite exhibits higher catalytic activity because of the enhancement of acid strength.

4.4 CONCLUSION

A series of sulfated ZrO_2/Al_2O_3 nanocomposites with fibrous morphology were synthesised as solid-superacid catalysts. The zirconium molar percentage was from 2 % to 50 %. Zr species is highly dispersed on alumina at Zr molar percentage up to 5 % and transferred into tetragonal zirconia nanocrystallites above 10 %. The surface Zr/Al molar ratios calculated from XPS results are higher than the bulk ratios when Zr molar percentage is above 15 %, and this is about 3 times as much as bulk value at 50 % of Zr molar percentage, suggesting an unambiguous core-shell structure formed. NMR results show that the interaction between zirconia species and alumina strongly correlates with pentacoordinated aluminium sites, which can also be detected by the dislocation of the bond energy 3d of the zirconium.

The acidity of the obtained superacids increases with Zr molar percentage, but the samples maintain an almost constant, large specific surface area due to their unique nanostructure. Benzolyation of toluene is investigated using these superacids. It is found that the catalytic activity of the catalyst is strongly related to the surface acidity of the catalyst. The amount of tetragonal zirconia and the resultant acidity of the catalyst increase with increasing Zr molar percentage. The sample with 50 % of zirconium molar percentage possesses the highest surface acidity equal to that of the pristine sulfated zirconia as well as the highest catalytic performance. The catalytic activity of as-synthesised nanocomposites with 30 % zirconium molar percentage surpasses that of the pristine sulfated zirconia due to the synergetic effect of the acid strength and enlargement of surface area.

4.5 REFERENCE AND NOTES

(1) Hino, M.; Kobayashi, S.; Arata, K. *J. Am. Chem. Soc.* **1979**, *101*, 6439.

(2) Hino, M.; Arata, K. *Chem. Lett.* **1979**, 1259.

(3) Hino, M.; Arata, K. *J.Chem.Soc., Chem. Commun.* **1979**, 1148.

(4) Farcasiu, D.; Li, J. Q. *Appl. Catal., A* **1998**, *175*, 1.

(5) Chen, F. R.; Coudurier, G.; Joly, J. F.; Vedrine, J. C. *J. Catal.* **1993**, *143*, 616.

(6) Huang, Y.-y.; Zhao, B.-y.; Xie, Y.-c. *Appl. Catal. A: Gen.* **1998**, *173*, 27.

(7) Jin, T.; Machida, M.; Yamaguchi, T.; TAnabe, K. *Inorg. Chem.* **1984**, *23*, 4396.

(8) Morterra, C.; Cerrato, G.; Pinna, F.; Signoretto, M. *J. Catal.* **1995**, *157*, 109.

(9) Djuricic, B.; Pickering, S.; Glaude, P.; Mcgarry, D.; Tambuyser, P. *J. Mater. Chem.* **1997**, *32*, 589.

(10) Sohn, J. R.; Seo, D. H. *Catal. Today* **2003**, *87*, 219.

(11) Hua, W.; Xia, Y.; Yue, Y.; Gao, Z. *J. Catal.* **2000**, *196*, 104.

(12) Gao, Z.; Xia, Y.; Hua, W.; Miao, C. *Top. Catal.* **1998**, *6*, 101.

(13) Kim, S. Y.; Lohitharn, N.; Jr., J. G. G.; Olindo, R.; Pinna, F.; Canton, P. *Catal. Commun.* **2006**, *7*, 209.

(14) Zhao, J.; Yue, Y.; Hua, W.; Gao, Z. *Catal. Lett.* **2007**, *116*, 27.

(15) Laidlaw, P.; Bethell, D.; Brown, S. M.; Hutchings, G. J. *J. Mol. Catal. A* **2001**, *174*, 187.

(16) Heidekum, A.; Harmer, M. A.; Hoelderich, W. F. *J. Catal.* **1999**, *188*, 230.

(17) Yadav, G. D.; Asthana, N. S.; Kamble, V. S. *Appl. Catal. A: Gen.* **2003**, *240*, 53.

(18) Arata, K.; Nakamura, H.; Shouji, M. *Appl. Catal. A: Gen.* **2000**, *197*, 213.

(19) Shen, S. C.; Ng, W. K.; Chen, Q.; Zeng, X. T.; Chew, M. Z.; Tan, R. B. H. *J. Nanosci. Nanotechno.* **2007**, *7*, 2726.

(20) Hino, M.; Arata, K. *J. Chem. Soc., Chem. Commum.* **1985**, *1985*, 112.

(21) Kloprogge, J. T.; Frost, R. L. *Phys. Chem. Chem. Phys.* **1999**, *1*, 1641.

(22) Moreau, S.; Gervais, M.; Douy, A. *Solid State Ionics* **1997**, *101-103*, 625.

(23) Guzman-Castillo, M. L.; Lopez-Salinas, E.; Fripiat, J. J.; Sanchez-Valente, J.; Hernandez-Beltran, F.; Rodriguez-Hernandez, A.; Navarrete-Bolanos, J. *J. Catal.* **2003**, *220*, 317.

(24) Shen, S. C.; Chen, Q.; Chow, P. S.; Tan, G. H.; Zeng, X. T.; Wang, Z.; Tan, R. B. H. *J. Phys. Chem. C* **2007**, *111*, 700.

(25) Iwamoto, R.; Fernandez, C.; Amoureux, J. P.; Grimblot, J. *J. Phys. Chem. B* **1998**, *102*, 4342.

(26) Bagshaw, S. A.; Pinnavaia, T. J. *Angew. Chem. Int. Ed.* **1996**, *35*, 1102.

(27) Younes, M. K.; Ghorbel, A. *J. Sol-Gel Sci. Techn.* **2003**, *26*, 677.

(28) Dalmaschio, C. J.; Mastelaro, V. R.; Nascente, P.; Bettini, J.; Zotin, J. L.; Longo, E.; Leite, E. R. *J. Colloid and Interface Sci.* **2010**, *343*, 256.

(29) Gregg, S. J.; Sing, K. S. W. The Physical Adsorption of Gases by Mesoporous Solids: The Type IV isotherm. In *Adsorption, Surface Area and Porosity*; Academic Press: London, 1982; pp 111.

(30) Sing, K. S. W.; Everett, D. H.; Haul, R. A. W.; Moscou, L.; Pierotti, R. A.; Rouquerol, J.; Siemieniewska, T. *Pure & Appl. Chem.* **1985**, *57*, 603.

(31) Sing, K. S. W.; Williams, R. T. *Adsorpt. Sci. Technol.* **2004**, *22*, 773.

(32) Li, G.; Li, W.; Zhang, M.; Tao, K. *Catal. Today* **2004**, *93-95*, 595.

(33) Canton, P.; Olindo, R.; Pinna, F.; Strukul, G.; Riello, P.; Meneghetti, M.; Cerrato, G.; Morterra, C.; Benedetti, A. *Chem. Mater.* **2001**, *13*, 1634.

(34) Jin, T.; Yamaguchi, T.; Tanabe, K. *J. Phys. Chem.* **1986**, *90*, 4794.

(35) Lee, J. S.; Park, D. S. *J. Catal.* **1989**, *120*, 46.

(36) Sikabwe, E. C.; Coelho, M. A.; Resasco, D. E.; White, R. L. *Catal. Lett.* **1995**, *34*, 23.

(37) Morterra, C.; Cerrato, G. *Phys. Chem. Chem. Phys.* **1999**, *1*, 2825.

(38) Xia, Y.; Hua, W.; Gao, Z. *Catal. Lett.* **1998**, *55*, 101.

(39) Rotter, H.; Landau, M. V.; Carrera, M.; Goldfarb, D.; Herskowitz, M. *Appl. Catal. B: Environ.* **2004**, *47*, 111.

(40) Xie, Y.-C.; Tang, Y.-Q. *Advances in Catalysis*; Academic Press: New York, 1990; Vol. 37.

Chapter 5:

Fabrication of macro-mesoporous titania-alumina core-shell nanocomposites with a 1D hierarchical structure

5.1 INTRODUCTION

Titania is regarded as one of the most important developing materials and has received considerable attention in numerous fields such as heterogeneous catalysis[1-4], solar energy conversion[5,6] and hazardous waste remediation[7,8]. However, its poor thermal stability and relatively low surface area of TiO_2 have impeded its practical applications. Several strategies have been developed to circumvent the drawbacks of TiO_2, such as synthesis of ZrO_2-TiO_2 mixed oxides[9] or TiO_2 pillared clays[10]. Preparing TiO_2/Al_2O_3 nanocomposites is a commonly used option to overcome the drawback of titania because Al_2O_3 is cheap and possesses good thermal stability and a large surface area.

In the last decade, TiO_2/Al_2O_3 nanocomposites have been commercially used as catalyst support for hydrotreatment of oil-derived feedstocks[11-15] with corresponding active components, such as CoMo or NiMo metal clusters. It is widely accepted that the structure of TiO_2 species existing on the surface of nanocomposites is of paramount importance for these applications[16,17]. The presence of surface TiO_2 structures fully covering the alumina species is essential for an increase of catalyst efficiency, because the active catalyst component dispersed on the TiO_2 surface will exhibit a higher intrinsic activity which is up to several times as much as they are supported on γ-Al_2O_3 surface[11,18]. In fact, some notable experiments even pointed out that the addition of 10 mol % alumina to the titania support reduced the catalytic activity to approximate that of catalysts supported on pristine

alumina[16,19]. To prepare ideal nanocomposites as catalyst support, the preparation method of this titania nanocomposites really need to be refined, with the goal of continuous improvement of surface properties and specific surface area[20-22].

Recent progress in catalyst preparation highlights a new research direction of the catalytic nanoarchitecture design in which the accessibility of reactant molecular to catalytic active centre is emphasised and should be included as an integral part of the catalyst design[23]. Particles with 1D morphology are regarded as an ideal building block for this purpose[24]. Because the stacking of 1D nanocomposites will generate large interparticle voids that allow the large organic molecules to diffuse rapidly to the active sites of catalyst, creating nanocomposites with 1D morphology will be a promising strategy to optimise catalyst structure. However, there is no documentation, to date, on the synthesis of nanocomposites with this specific morphology as well as with the appropriate surface properties.

In our previous chapter, we prepared a 1D ZrO_2/Al_2O_3 nanocomposite with a specific core-shell structure. The stacking of the resultant composite generates a hierarchically macro-mesoporous material: the evenly distributed ZrO_2 nanocrystallites on long bundles of alumina nanofibres formed a layer of mesoporous zirconia with relatively large surface areas while the aggregation of 1D nanostructure gave rise to a novel macroporous framework. The core-shell structure of 1D ZrO_2/Al_2O_3 nanocomposite minimised the exposed alumina surface at high Zr content, making the surface property of nanocomposites close to pristine ZrO_2. We further developed this material into a superacid catalyst by grafting sulphate ion on the surface of 1D nanocomposites. The catalyst with 50 % Zr molar percentage exhibited higher activity than that for the pristine sulphated zirconia by a factor of 1.4. The success of developing zirconia nanocomposites into a new class of superacid catalyst motivated us to adapt the synthetic strategy to the preparation of TiO_2/Al_2O_3 nanocomposites. In this work, a series of TiO_2/Al_2O_3 nanocomposites were synthesised with the Ti/Al molar ratio varied from 1 to 3. We modified our synthetic strategy allowing the 1D TiO_2/Al_2O_3 nanocomposites

to be prepared at relatively low temperatures, which may benefit the production of such materials on an industrial scale.

The morphologies of the resultant nanocomposites were investigated by SEM and the physicochemical properties of the resultant nanocomposites were characterised by means of XRD, UV-Visible, IES, and the N_2 adsorption/desorption isotherms. The hierarchical macro-mesoporous structures of TiO_2/Al_2O_3 nanocomposites have potential as catalyst support to overcome the diffusion problem and rapid deactivation of the catalyst suffered in some industrial process, such as hydrotreatment of heavy crude oil[12].

5.2 EXPERIMENTAL SECTION

Materials. Boehmite nanofibres were synthesised by steam-assisted solid wet-gel method according to previous reports[25]. Butanol was purchased from Ajax Finechem and Titanium (IV) butoxide was purchased from Aldrich. All these chemicals were used as received without further purification.

Nanocomposite preparation. A series of Titania-alumina nanocomposites were synthesised by a modified sol-gel method as we previously introduced. In a typical procedure, a gel-like dispersion of boehmite nanofibers was prepared following our previous work: a wet cake of boehmite nanofibers, prepared by adding 0.40g of deioned water to 0.39 g of boehmite nanofibers, was then dispersed into 20 ml of butanol by continuous stirring. This stirring was maintained for 24 hours to ensure the even dispersion of the nanofibers. Titanium butoxide was dissolved into the resultant butanol mixture according to the molar ratios X=Ti/Al= 1, 2, 3, respectively. The viscous fluids were heated at 80^{o}C for 24 hours, and followed by adding 10 ml of deionised water and aged at ambient temperature for 24 hours to enhance their hydrolysis. The resulting nanocomposites were separated by centrifugation and dried at 80 ^{o}C for 1 day without any washing. After calcination at 450^{o}C, these samples were labelled as Ti-"m"-T, where m is Ti/Al molar ratios and T is calcined temperature. For comparison, a sample with Ti/Al molar ratio =1 was prepared without

adding 10 ml of deionised water but by keeping other procedure the same as mentioned above. The sample was labelled as "a-Ti-1-450" after calcination at 450^{o}C.

Characterisation. *XRD analyses* were performed on a PANalytical X'Pert PRO X-ray diffractometer (radius: 240.0 mm). Incident X-ray radiation was produced from a line-focused PW3373/10 Cu X-ray tube, operating at 40kV and 40mA, providing a $K\alpha_1$ wavelength of 1.540596 Å. The incident beam passed through a 0.04 rad Soller slit, a ½ divergence slit, a 15mm fixed mask, and a 1° fixed antiscatter slit. After interaction with the sample, the diffracted beam was detected by an X'Celerator RTMS detector, which was set in scanning mode, with an active length of 2.022mm, and samples were analysed over a range of 3~ 75^{o} 2θ. *Surface Area Analysis* based on N_2 adsorption/desorption techniques were performed on a Micrometrics Tristar 3000 automated gas adsorption analyser. Samples were pretreated at 200 ^{o}C under the flow of N_2 for minimum 5 h on a Micrometrics Flowprep 060 degasser. *SEM image* was obtained on a FEI QUANTA 200 scanning electron microscope. The samples were dried at room temperature and coated with gold under vacuum conditions in an argon atmosphere ionisation chamber to increase surface conductivity. *FT-IR emission spectroscopy* was carried out on a Digilab FTS-60A spectrometer but modified by replacing the IR source with an emission cell. The description of the cell and principles of the emission experiment have been published elsewhere[26]. *UV-visible diffuse reflectance spectra* were obtained on a Cary 5000 UV-VIS-NIR scanning spectrophotometer equipped with a diffuse reflectance accessory. The absolute remittance $R\infty$ from the sample was measured. Relative remittance quantity $R'_{\infty}=R'_{\infty}(sample)/R'_{\infty}(reference)$ was used to calculate the Kubelk-Munk function defined as $F(R_{\infty})$. The spectra were recorded using $BaSO_4$ as reference.

5.3 RESULTS AND DISCUSSION

In chapter 3 and chapter 4, 1D nanocomposites of zirconia has been developed. The material was prepared by the hydrolysis of zirconium butoxide on the 1D framework of

linearly connected boehmite nanofibres dispersed in butanol solution. These frameworks spontaneously formed when the nanofibres adsorbed small amounts of water on their hydroxylated surface and had then been dispersed into a hydrophobic alcohol. The hydrolysis of zirconium butoxide occured only on the outside of the 1D framework of boehmite nanofibres by reaction with the absorbed water, to generate an amorphous layer of zirconia which affixes to the fibrous framework of the boehmite nanofibres. The loading ratio of zirconia was found to be extremely large, about 1:1 of Zr/Al molar ratio in our work, making the surface of nanocomposites similar to the pristine zirconia after calcination, and the fibrous cores of alumina transferred from boehmite nanofibres endows the materials with good mechanical and thermal stabilities.

The water absorbed on the surface of boehmite nanofibres is essential to form the framework of boehmite nanofibres as well as the hydrolysis of alkoxide. Its amount is limited for preparing an order distribution of boehmite nanofibres. Such an amount of water is relatively less for the sol-gel process of alkoxide, and the preparation of a fully hydrolysed amorphous layer was previously realised at elevated temperatures.

In the present study, to precipitate an amorphous titania layer over the 1D framework of boehmite nanofibers, the titanium butoxide hydrolysis can only be conducted at about or below 80^{o}C because titania hydrolysates are prone to crystallize into anatase phase at higher temperatures. However, at 80^{o}C, an amorphous titania layer prepared under lean water condition is not strong enough to maintain the 1D aforementioned frameworks and the composite structure fabricated by boehmite nanofibres will be cracked by the capillary pressure gradient generated during the drying step[27,28]. Therefore, to prepare a robust amorphous titania layer, the preparation approach is modified by a post-treatment step of adding excessive water to facilitate the hydrolysis and condensation of titania species, after the titanium species is deposited on the frameworks of boehmite nanofibres at 80^{o}C. The Ti/Al molar ratios are varied from 1 to 3 to determine a possible upper limit of the titania loading.

The SEM images of the product nanocomposites and pristine boehmite nanofibres are illustrated in Figure 1. The boehmite nanofibres (Figure 1a) are worm like particles about 200 nm ~500 nm in length, which are severely entangled together. The TiO_2/Al_2O_3 nanocomposites, with or without post treatment by the addition of 10 ml of deionised water to intensify hydrolysis of titania layer exhibit distinctly different morphology. Without post-treatment, the sample (a-Ti-1-450) shows an agglomerated morphology, where the titania and alumina nanofibers are compressed together forming a densified stacking. The samples with post treatment exhibit fibrous morphologies from 1 to 2 of Ti/Al molar ratios. The nanocomposite with 3 Ti/Al molar ratio shows an interesting morphology: titania microspheres which are braced by alumina nanofibers forming a unique titania networks. Therefore, all the samples prepared with post addition of water have low density and relatively high pore volume.

XPS is used to investigate the binding energies of the different element and Ti/Al surface atomic ratio of these nanocomposites. The results are summarized in Table 1. In XPS spectra, the Ti 2p and Al 2p binding energies are constant for all the nanocomposites as the Ti/Al molar ratio varied from 1 to 3. The Ti $2p_{1/2}$ and $2p_{2/3}$ appear as an unresolved doublet, whose peak positions are observed at 458.6±0.2 and 464.2±0.2 eV, indicating that the TiO_2 constitution in these nanocomposites. It should be noted here, for these nanocomposites, the overall Ti/Al molar ratios measured by Energy-Dispersive X-ray (EDX) microanalysis via SEM are identical to the added Ti/Al molar ratios. However, owing to the different morphologies of these nanocomposites, their Ti/Al XPS atomic ratios exhibit distinctive discrepancies to the bulk Ti/Al molar ratios detected by EDX. For the sample with densely aggregated morphology(Figure 1b), the XPS ratio is the same as the overall ratio detected by EDX, whereas for the samples with 1D composite morphology, external surface enrichment of Ti can be observed, and the Ti/Al XPS ratio significantly achieves to 6:1 as the bulk ratio is merely 2. Nevertheless, it is somewhat surprising that the titania microspheres braced by

alumina nanofibres, possessing the highest bulk Ti/Al molar ratio of 3, exhibits the lowest Ti/Al XPS ratio of only 0.59.

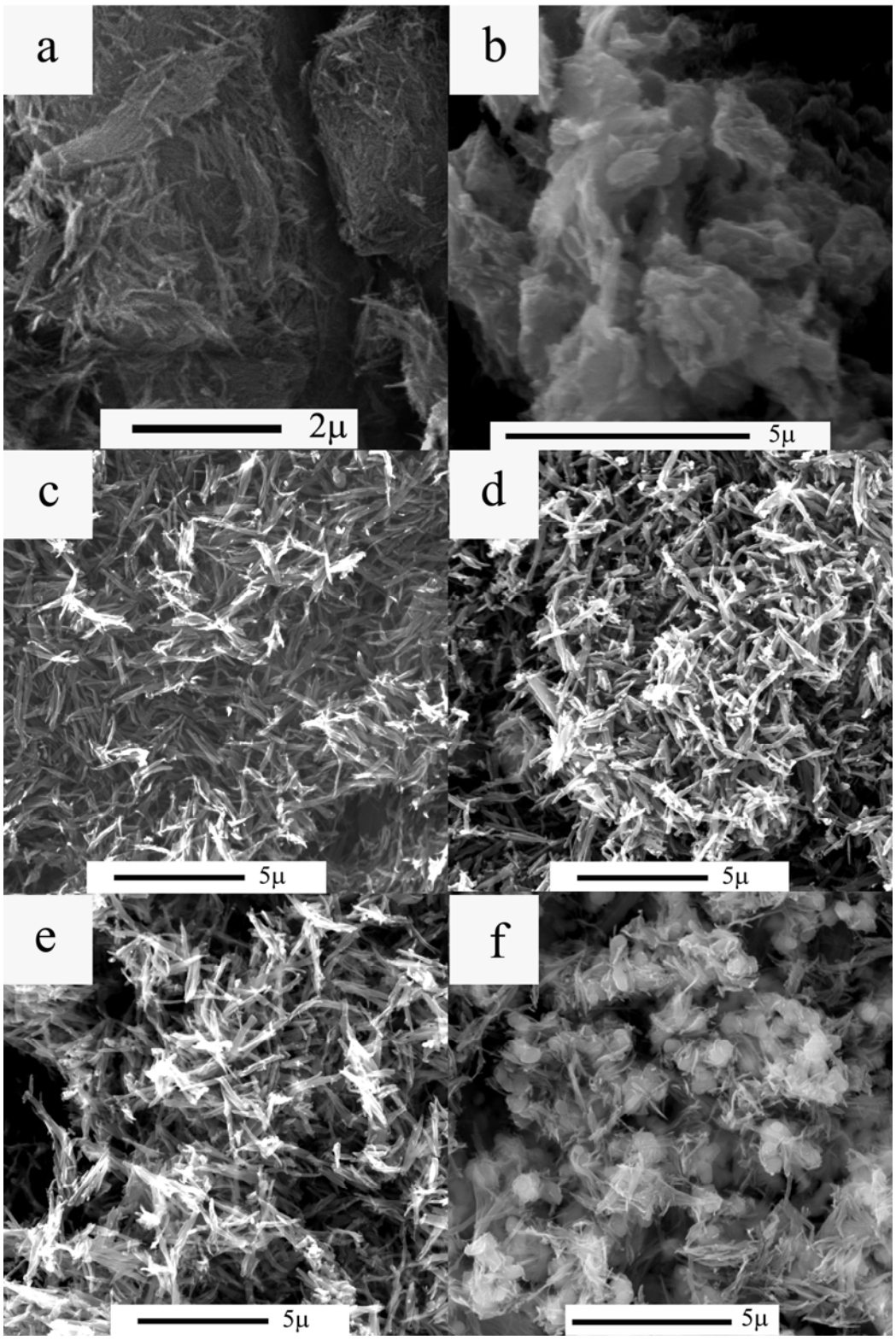

Figure 1. SEM images of a) boehmite nanofibres b) a-Ti-1-450 c) Ti-1-450 d) Ti-1.5-450 e) Ti-2.0-450 f) Ti-3.0-450

Table 1. XPS binding energies for all the nanocomposites and their Ti/Al molar ratios measured by EDX and XPS respectively

Sample name	Ti $2p_{3/2}$	Al 2p	Ti/Al (EDX)	Ti/Al (XPS)
a-Ti-1-450	458.7	74.5	1.04	0.92
Ti-1-450	458.5	74.3	1.02	1.80
Ti-1.5-450	458.5	74.5	1.45	2.30
Ti-2.0-450	458.6	74.4	2.03	5.94
Ti-3.0-450	458.6	74.5	2.98	0.59

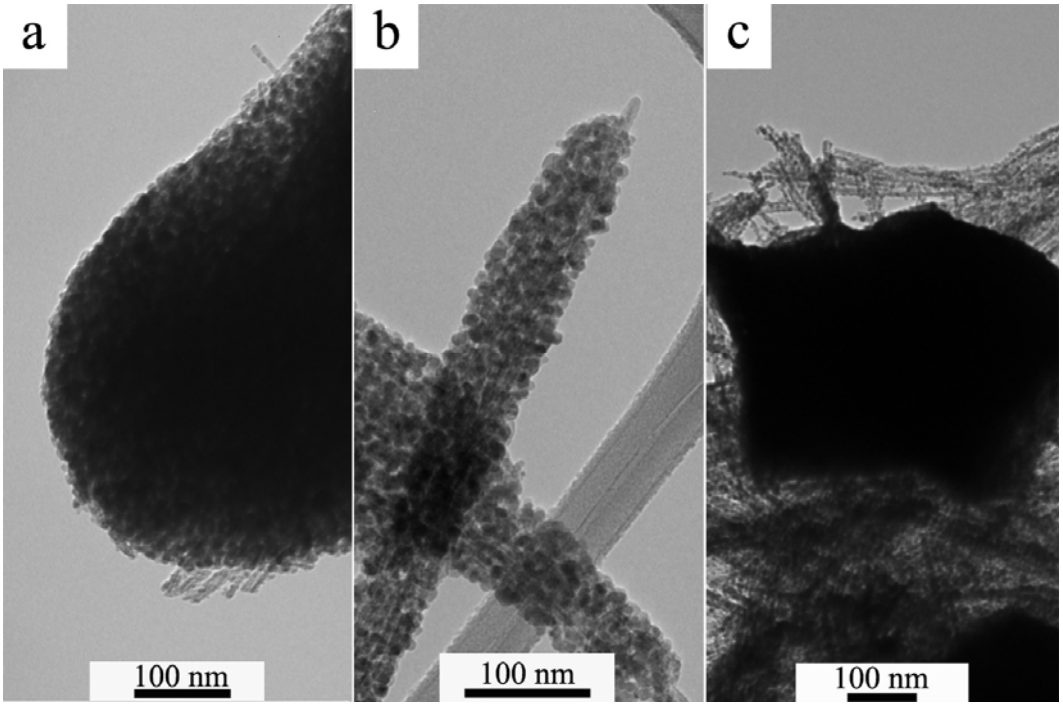

Figure 2. TEM image for the nanocomposites with different morphologies a) densely aggregated morphology (a-Ti-1-450) b) 1D nanostructure (Ti-2-450) c) titania microsphere (Ti-3-450)

TEM images of representative samples are shown in Figure 2. The deviation of Ti/Al molar ratio between the XPS and EDX measurements could be illustrated by their TEM observation. As shown in Figure 2, for the densely aggregated sample, the Ti species and alumina nanofibres are apt to be evenly distributed, leading to the XPS Ti/Al molar ratio, and the EDX Ti/Al molar ratio are almost the same. However, for the sample with 1D morphology, a layer of titania nanocrystallites is deposited on the outer-surface of alumina bundles forming a porous nanorod, therefore the XPS Ti/Al molar ratio is dramatically higher than that measured by EDX. For the sample Ti-3-450, the titania is not distributed evenly and a superior fraction aggregates into microspheres which are surrounded and segregated by the alumina nanofibres. Therefore, although its bulk Ti/Al molar ratio is about 3, the Ti/Al molar ratio measured by XPS is only 0.59.

The processes for the formation of the nanocomposites with various morphologies are summaried in Scheme 1. The synthesis starts by preparing a gel-dispersion by dispersing wet boehmite nanofibres in butanol solution. Following this, the hydrolysis of titanium butoxide at 80^{o}C forms an amorphous titania layer covering the long bundles of boehmite nanofibers and the amount of precipitated titania depends on the amount of water adsorbed on boehmite nanofibres. Subsequently, a stiff 1D-nanocomposite structure is synthesised by the post addition of water, which can be regarded as separated controls for the hydrolysis and condensation of titanium species. It should be emphasized here that the boehmite nanofibres are able to stabilize the emulsion of water in hydrophobic alcohol, therefore, titania microspheres are generated by the reaction between the un-hydrolysed titanium species and microsphere of water in butanol when the Ti/Al molar ratio is about 3.

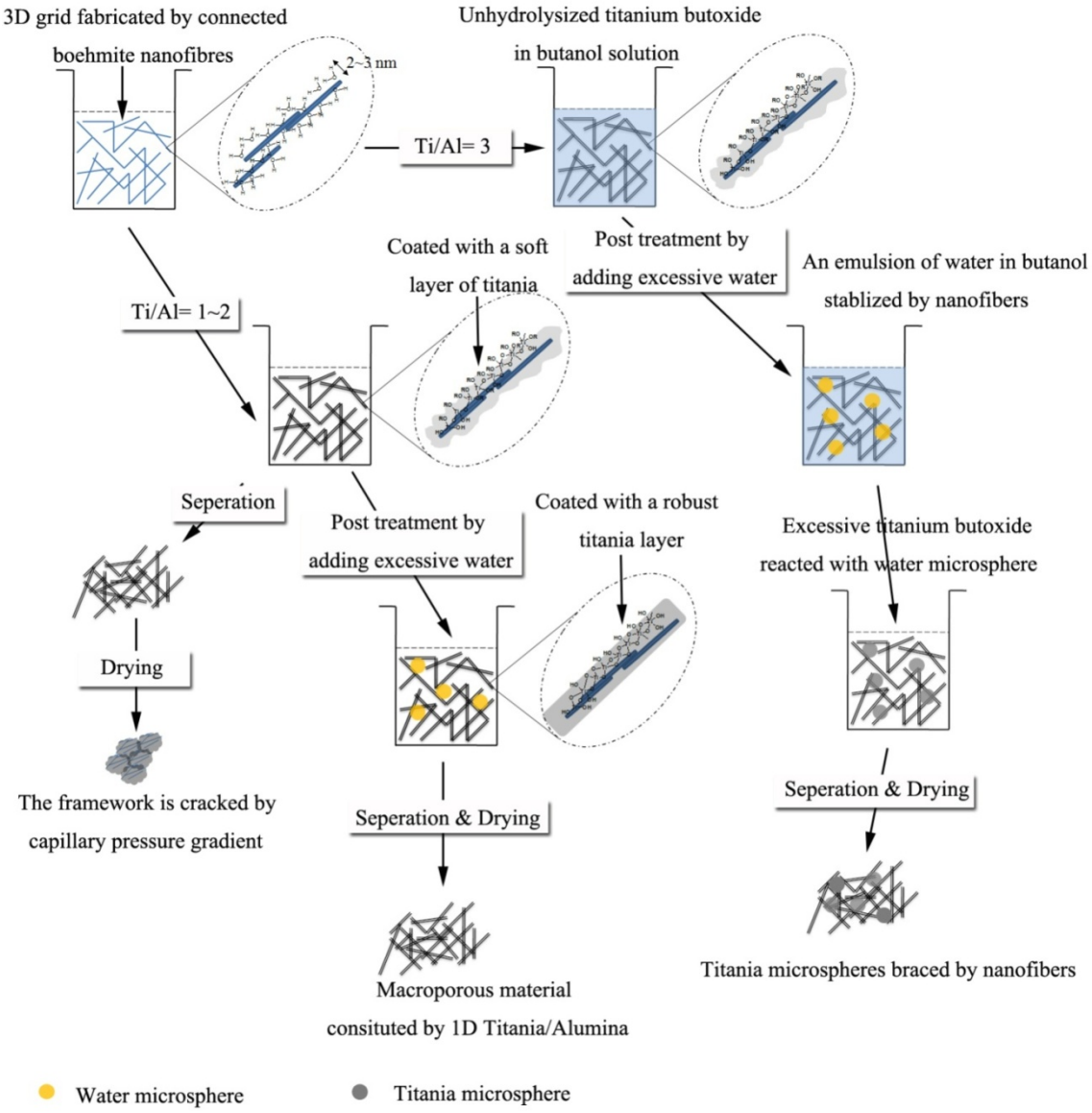

Scheme 1. Schematic for Formation of TiO_2/Al_2O_3 with different morphologies

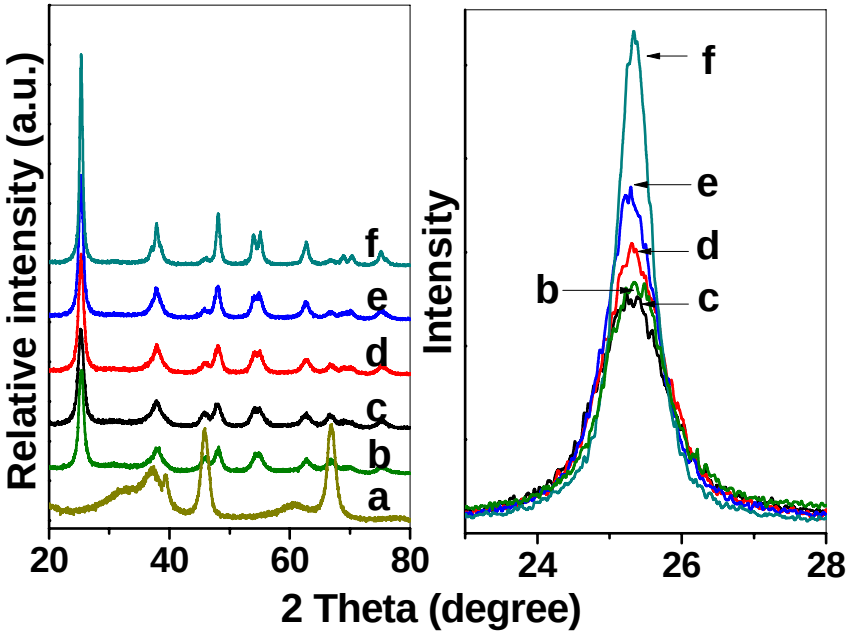

Figure 3. X-ray diffraction patterns of a) pristine Al_2O_3 nanofibers b) a-Ti-1-450 c) Ti-1-450 d) Ti-1.5-450 e) Ti-2.0-450 f) Ti-3.0-450

The XRD patterns of these TiO_2/Al_2O_3 nanocomposites and pristine Al_2O_3 nanofibers are given in Figure 3. The pristine alumina nanofibers prepared by calcination of boehmite nanofibre at 450°C presents as the γ-Al_2O_3 phase. For these TiO_2/Al_2O_3 nanocomposites, the predominant diffraction peaks are the anatase phase of TiO_2; only two weak peaks corresponding to the diffractions of (400) and (440) planes of γ-Al_2O_3.can be observed at about 45.8 and 66.8 °2θ. The anatase diffraction peaks intensified with the increase of Ti/Al molar ratio from 1 to 3, while the samples, a-Ti-1-450 and Ti-1-450, with same Ti/Al molar ratio exhibit the same diffraction intensity in spite of their different morphology. The crystal sizes of anatase for all these nanocomposites are calculated with the Scherrer equation and shown in Table 2. By comparison, the crystal size of anatase phase increases about two times as the Ti/Al molar ratio increases from 1 to 3, which is from 7.3 nm to 14.4 nm. However, it is worth mentioning here that, for the sample with 1 Ti/Al molar ratio without 1D morphology, the crystal size of anatas is about 8.4 nm which is larger than that for the sample possessing 1D morphology. Clearly, this difference results from poor titania

distribution in the sample without 1D morphology owing to its structure cracking during the drying step.

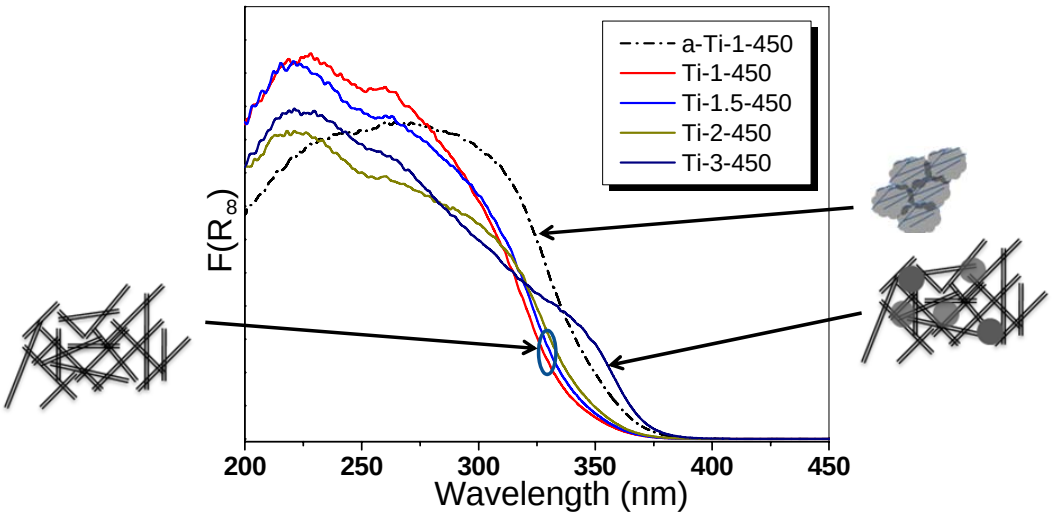

Figure 4. UV-visible spectra of as-synthesised TiO_2/Al_2O_3 nanocomposites

Diffuse reflectance UV-visible spectroscopy is used to determine the indirect interband transition energies for these nanocomposites. For the samples with fibrous morphologies, the increase of Ti/Al molar ratios from 1 to 2 results in an evident steepening of the UV-visible band and a concomitant red-shift of onset to approximately 380 nm. The largest red shift was observed for the nanocomposite with 3 Ti/Al molar ratio of which the morphology is interconnected titania microspheres. Interestingly, the densely aggregated TiO_2/Al_2O_3 nanocomposite, a-Ti-1-450, has the second largest red shift, despite its relatively low Ti/Al molar ratio (Ti/Al =1) among the nanocomposites.

TiO_2 (anatase) is known to be an indirect semiconductor. Using the diffuse reflectance spectra, the band gaps energy of as-synthesised nanocomposites can be evaluated by plotting $(F(R_\infty)\bullet E)^{1/2}$ against E from the spectroscopic data in Figure 4 (Where $E=h\nu$ represent the photoenergy and $F(R_\infty)$ is the so-called remission or Kubelka-Munk function)[29-32]. As shown

in Figure 5, the values are estimated by the intersection between the linear fit of the curves and the photon energy axis. It can be observed that the increase of Ti/Al molar ratio from 1 to 3 results in the indirect band gap energy E_g changing from 3.40 to 3.21, but the sample a-Ti-1-450 possesses a similar ratio for E_g to Ti-3-450 which unexpectedly presents at 3.21.

The crystal sizes of the as-synthesised nanocomposites are calculated from band gap shift (ΔE_g) using the following equation[33,34].

$$\Delta E_g \approx \frac{h^2}{8\mu R^2} - \frac{e^2}{\varepsilon R}$$

Where the ΔE_g is the blue shift relative to that of the bulk TiO_2 crystals, well known to be E_g=3.2 eV, h is Planck's constant, R is the radius of the particle, ε is the relative permittivity of the semiconductor, e is the elementary charge and μ is the reduced mass of the excition, i.e., the reduced effective mass of the electron charge and hole. One calculates μ=1.63 m_e (m_e is the electron rest mass)[35]. The equation provides an approximate prediction of the increase in bandgap energy for a semiconductor particle displaying size quantisation, and is also used to estimate the size of small semiconductor particles.

Table 2. The crystallite dimensions of anatase phase of titania calculated from both the Uv-spectra and X-ray diffraction patterns

Sample name	E_g	Uv calculation D =2R	XRD calculation
a-Ti-1-450	3.21	10 nm	8.4
Ti-1-450	3.40	2.2 nm	7.3
Ti-1.5-450	3.35	2.6 nm	7.9
Ti-2.0-450	3.30	3.2 nm	9.5
Ti-3.0-450	3.21	10 nm	14.4

The particle sizes of TiO_2 of as-synthesized nanocomposites calculated from UV-visible spectra are summarized along with the values calculated by Scherrer equation from XRD results (Table 2). It can be observed that for the samples with fibrous morphology, the crystal sizes calculated from XRD method are commonly larger than the values obtained from UV method; however, for the samples without fibrous morphology, a-Ti-1-450 and Ti-3-450, the discrepancy between the two kinds of calculations is not evident. Combined with TEM observation, the anatase nanocrytallites are evenly dispersed in low dimensionality on fibrous nanocomposites, but they are densely stacked into bulk particles for a-Ti-1-450 and Ti-3-450, which are without fibrous morphology. Therefore, in this work, the blue shifts of the anatase band gap for fibrous nanocomposites are attributed to low dimensional arrangement of anatase nanocrystallites which is close to TiO_2 nanosheet[36]. The effect of incorporating with alumina core on the shift of anatase absorption edge is not significant in this work.

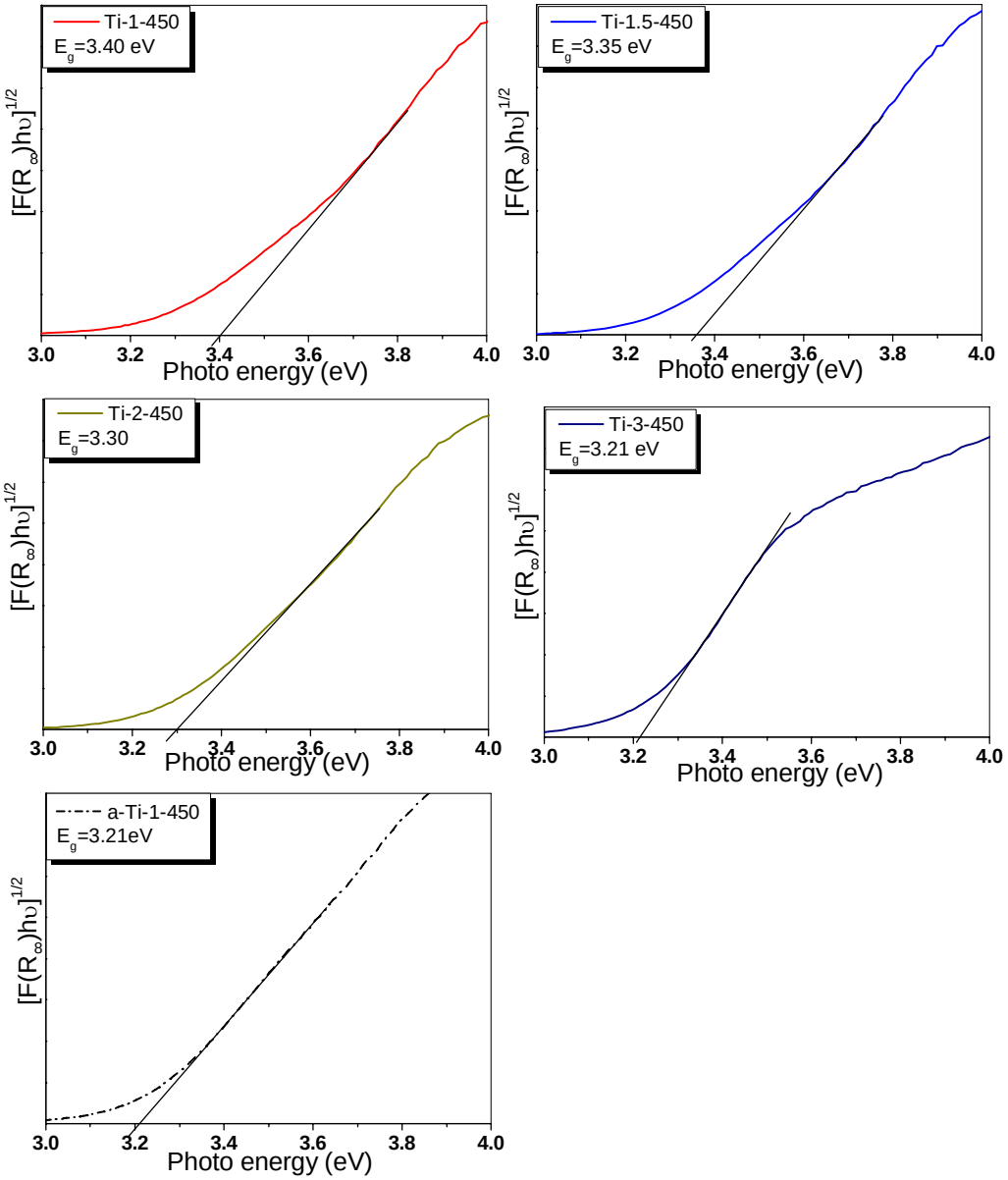

Figure 5. Determination of the indirect interband transition energies for as-synthesized TiO_2/Al_2O_3 nanocomposites

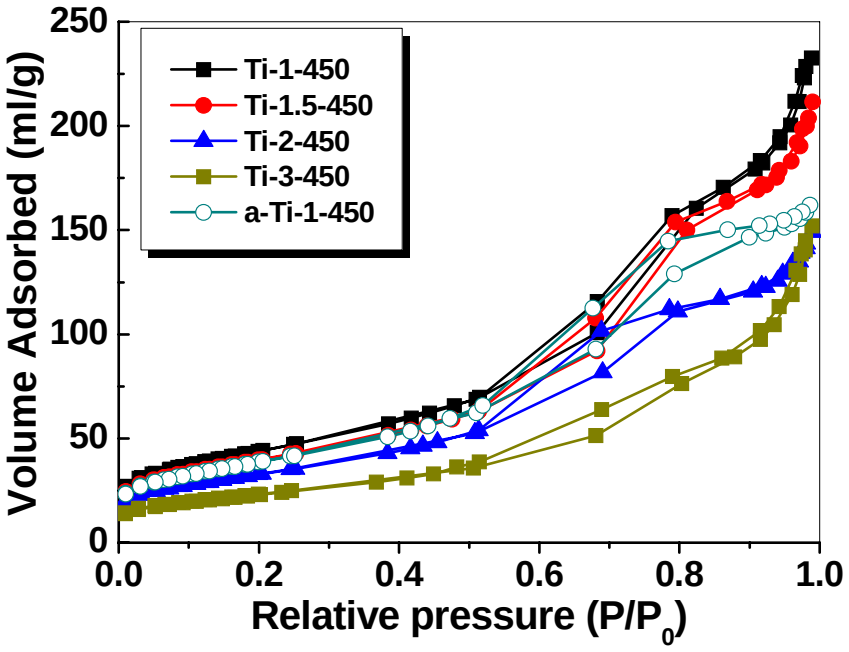

Figure 6. Nitrogen adsorption and desorption isotherms for as-synthesized nanocomposites

The surface area and textural structures of the as-synthesized nanocomposites are investigated by nitrogen adsorption-desorption isotherms (Figure 6). For the sample "a-Ti-1-450", the isotherm is of classical type IV with a H2 hysteresis loop[37]. This isotherm is the characteristic feature of mesoporous materials and the H2 hysteresis loop indicates the material comprising ink bottle pores or pore network[38].

The isotherm of this sample exhibits a plateau above a certain relative pressure, which is due to the tight agglomeration of alumina nanofibres and anatase with non-specific morphology. Interestingly, the samples with 1D morphologies and titania microsphere braced by nanofibres exhibit almost the same isotherms. Besides the Type IV isotherms and H2 hysteresis loop that can be observed, the characteristic feature of the isotherms of these samples is the dramatic uptake of N_2 adsorption at high relative pressure. Furthermore, in this part, the desorption branch essentially follows the adsorption branch. This shape of the isotherm resembles a combination of Type IV and Type II[37], indicating that the materials contain meso- and macroporous frameworks.

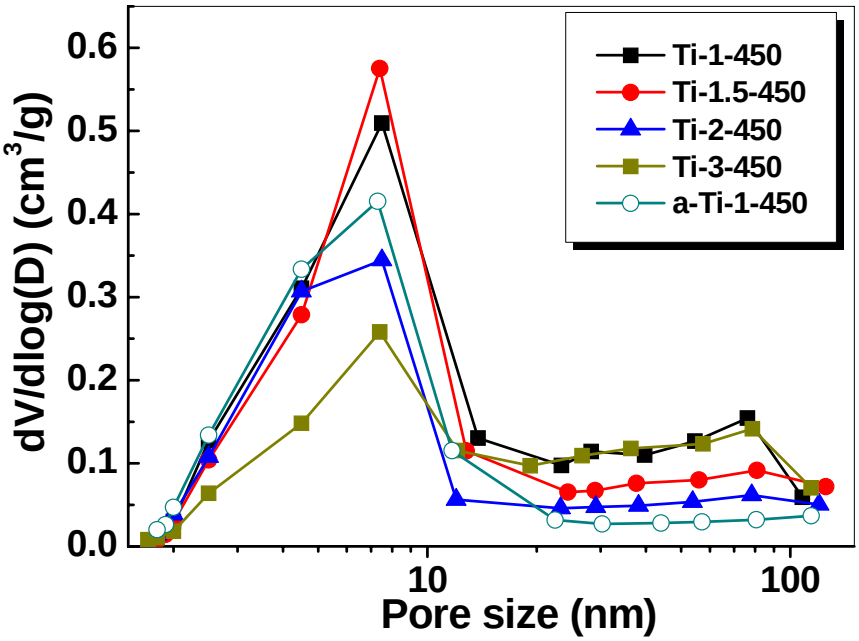

Figure 7. Pore size distributions for TiO_2/Al_2O_3 nanocomposites

The pore size distributions determined from the adsorption branch of the isotherms are shown in Figure 7. All these nanocomposites show two distributions from 1-11 nm and from 11-100 nm, respectively. The former distribution is attributed to the pores formed by anatase nanocrystallites and the latter part is assigned to a macroporous framework. Since the predominant distribution of the macroporous framework is larger than 100 nm, which exceeded the measurable range for N_2 physisorption, the distribution in this range is very small. Interestingly, the number of mesopores in the range from 1nm to 10nm does not simply increase with the increase of Ti/Al molar ratios, which increases as the Ti/Al molar ratio varies from 1 to 1.5, but decreases as further increasing titanium content. Such a decrease of mesoporous distribution could be readily ascribed to the growth of anatase nanocrystallites. The porosity of the materials decreases with the coarsening of anatase nanocrystallites. Moreover, it is also noted here that the tightly agglomerated sample, a-Ti-1-450, possesses more pores in the range from 1 to 3 nm compared with the samples having macroporous framework.

A more quantitative comparison on the textural structure is presented in Table 3. It can be observed that the surface area decreased with the increase of Ti/Al molar ratio, which should also be attributed to the crystal growth of titania. The morphology of nanocomposites imposes less effect on their surface areas: the surface area of the tightly agglomerated sample a-Ti-1-450 is only slightly smaller than its counterpart with 1D morphology.

Table 3. Pore structures of as-synthesised TiO_2/Al_2O_3 nanocomposites

Sample	BET surface area(m^2/g)	Average pore size (nm)	Pore volume (cm^3/g)
a-Ti-1-450	141	7.10	0.250
Ti-1-450	159	9.07	0.360
Ti-1.5-450	143	9.10	0.327
Ti-2-450	119	7.72	0.230
Ti-3-450	84	11.20	0.235

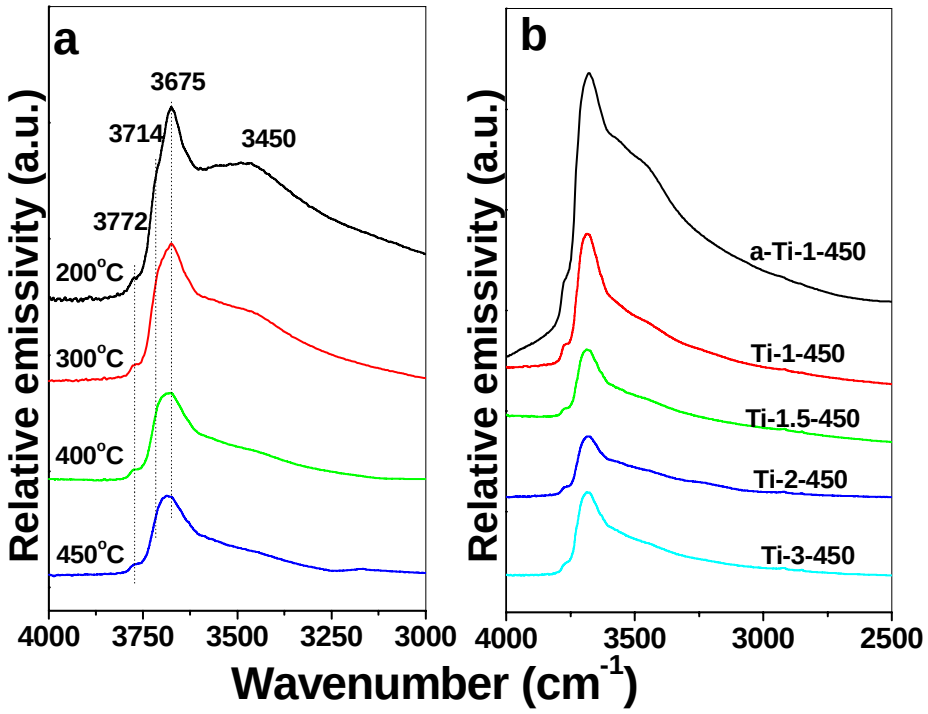

Figure 8. Infrared emission spectra of a) a representative sample (Ti-2-450) measured from 200°C to 450°C and b) all TiO_2/Al_2O_3 nanocomposites measured at 450°C

Infrared emission spectra was employed to determine the surface properties of as-synthesised nanocomposites as the technique allows the in-situ measurement of spectra at elevated temperature, while the simultaneous removal of surface-absorbed water during the heating facilitates the detection of specific surface hydroxyls of the materials. The maximum measuring temperature is limited to 450°C to prevent the specimen from undergoing possible phase change to rutile. Since all these nanocomposites have a high loading of titania, which varied from 1 to 3 in Ti/Al molar ratios, the surface OH stretching bands for all these nanocomposites are similar. Figure 8a shows the spectra obtained from 200°C to 450°C of Ti-2-450, which acts as a representative sample. At 200°C, the water of multilayer absorption has been removed, and only a single layer of absorbed water still resides, which is detected as a broad hump centred at 3450 cm^{-1}. In addition, a sharp band at 3675 cm^{-1} and a shoulder at 3714 cm^{-1} are also detected by IES. The band at 3675 cm^{-1} is assigned to the vibration of bridging OH groups which are generated by water molecules strongly bound to low

coordinated Ti^{4+} cations.The band at 3714 cm^{-1} is ascribed to the distal OH groups of anatase[39-41]. The band at 3772 cm^{-1} is from a novel species, compared with pristine titania, which has been detected even when small amounts of titania are incorporated on γ-Al_2O_3 supports[42]. This OH stretching band most likely results from the interaction between the titania and alumina. During heating the specimen, all species adsorbed on the surface, such as the adsorbed water and OH groups are gradually removed. As can be seen, the intensity of the band at 3675 cm^{-1} corresponding to the bridging OH groups significantly decreases, whereas that of the band corresponding to isolated OH group at 3714 cm^{-1} seems unchanged or only slightly decreases as the temperature varied from 200^{o}C to 450^{o}C. This variation is most likely due to their different origins as mentioned above; the water molecules bound to low coordiatied Ti^{4+} are significantly evacuated at elevated temperature while the distal OH groups of anatase seem relatively stable, which results in the two bands incorporating into one broad species at 450^{o}C.

The comparison of surface hydroxyl groups for all nanocomposites is conducted at 450^{o}C. As shown in Figure 8b, the surface species for the nanocomposites with 1D morphology and the titania microsphere braced by alumina nanofibres are almost same, independent of the Ti/Al molar ratio varying from 1 to 3. They are mainly bridging OH groups and distal OH groups of anatase. However, for the sample with tightly agglomerated morphology, its spectra shows that the intensity of the band at 3450 cm^{-1}, represents the adsorbed water, and is abnormally strong compared with other nanocomposites. This is presumably because the adsorbed species are difficult to remove for this sample as a result of the densified stacking of its constituents and more microporous distribution as indicated by nitrogen adsorption-desorption results. This difference derived from their morphologies may result in their different performances in catalytic applications.

5.4 CONCLUSION

In summary, we have proposed a new synthesis strategy for fabricating 1D TiO_2/Al_2O_3 nanocomposites with a core-shell structure by depositing titania species onto the 1D bundles

of boehmite nanofibres. These titania species are converted into anatase nanocrystallites with mesoporous aggregations in the subsequent calcination, while the assembly of particles with 1D morphology forms the marcoporous framework of this material. In this approach, to prepare a controllable and stable 1D nanostructure, the preparation is conducted by two coupled processes: depositing the titanium precursor on the 1D dispersion of boehmite nanofibres and further intensifying the condensation of titania species by a post-treatment step of addition of an excessive amount of water into synthetic system. The former process is well controlled by adsorbing small amount of water on the surface of boehmite nanofibres and the latter leads to formation of a robust titania wrapping around bundles of boehmite nanofibres. The robust titania wrapping is required in this approach to prevent the elaborate nanostructure from being crushed by capillary forces during the drying step. In accordance with this modified mechanism, we can synthesize 1D TiO_2/Al_2O_3 nanocomposites with Ti/Al molar ratio =2. Moreover, we also recognized that boehmite nanofibres can be used to prepare a stable emulsion of water in butanol solution. Because of this, at higher Ti/Al molar ratio, the un-hydrolyzed titanium species can form titania microsphere which are further braced by alumina nanofibers resulting in low-density aggregation. It should be mentioned here that the proposed synthesis is an effective approach for preparation of nanocomposites with macroporous materials at relatively low synthesis temperature, which may facilitate the synthesis of such materials on an industrial scale.

5.5 REFERENCE AND NOTES

(1) Chen, M. S.; Goodman, D. W. *Science* **2004**, *306*, 252.

(2) Fox, M. A.; Dulay, M. T. *Chem. Rev.* **1993**, *93*, 341.

(3) Linsebigler, A. L.; Lu, G.; Jr, J. T. Y. *Chem. Rev.* **1995**, *95*, 735.

(4) Formo, E.; Lee, E.; Campbell, D.; Xia, Y. *Nano. Lett.* **2008**, *8*, 668.

(5) Park, K.; Zhang, Q.; Garcia, B. B.; Zhou, X.; Jeong, Y.-H.; Cao, G. *Adv. Mater.* **2010**, *22*, 2329.

(6) Jose, R.; Thavasi, V.; Ramakrishna, S. *J. Am. Ceram. Soc.* **2009**, *92*, 289.

(7) Hoffmann, M. R.; Martin, S. T.; Choi, W.; Bahnemann, D. W. *Chem. Rev.* **1995**, *95*, 69.

(8) Zhao, J.; Chen, C.; Ma, W. *Top. Catal.* **2005**, *35*, 269.

(9) Reddy, B. M.; Khan, A. *Catal. Rev.* **2005**, *47*, 257.

(10) Zhu, H. Y.; Zhao, J.-C.; Liu, J. W.; Yang, X. Z.; Shen, Y. N. *Chem. Mater.* **2006**, *18*, 3992.

(11) Borque, M. P.; Lopez-Agudo, A.; Olguin, E.; Vrinat, M.; Cedeno, L.; Ramirez, J. *Appl. Catal.* **1999**, *180*, 53.

(12) Maity, S. K.; Ancheyta, J.; Soberanis, L.; Alonso, F.; Llanos, M. E. *Appl. Catal. A: Gen* **2003**, *244*, 141.

(13) Olguin, E.; Vrinat, M.; Cedeno, L.; Ramirez, J.; Borque, M.; Lopez-Agudo, A. *Appl. Catal. A: Gen* **1997**, *165*, 1.

(14) Yoshinaka, S.; Segawa, K. *Catal. Today* **1998**, *45*, 293.

(15) Ramirez, J.; Cedeno, L.; Busca, G. *Journal of Catalysis* **1999**, *184*, 59.

(16) Ramirez, J.; Gutierrez-Alejanjre, A. *J. Catal.* **1997**, *170*, 108.

(17) Ramirez, J.; Macias, G.; Cedeno, L.; Gutierrez-Alejandre, A.; Cuevas, R.; Castillo, P. *Catal. Today* **2004**, *98*, 19.

(18) Dzwigaj, S.; Louis, C.; Breysse, M.; Cattenot, M.; Belliere, V.; Geantet, C.; Vrinat, M.; Blanchard, P.; Payen, E.; Inoue, S.; Kudo, H.; Yoshimura, Y. *Applied Catalysis B: Environmental* **2003**, *41*, 181.

(19) Ramirez, J.; Fuentes, S.; Diaz, G.; Vrinat, M.; Breysse, M.; Lacroix, M. *Appl. Catal.* **1989**, *52*, 211.

(20) Gutierrez-Alejandre, A.; Ramirez, J.; Val, I. J.-d.; Penuelas-Galaz, M.; Sanchez-Neri, P.; Torres-Mancera, P. *Catal. Today* **2005**, *107-108*, 879.

(21) Segawa, K.; Takahashi, K.; Satoh, S. *Catal. Today* **2000**, *63*, 123.

(22) Grzechowiak, J. R.; Wereszczako-Zielinska, I.; Rynkowski, J.; Ziolek, M. *Appl. Catal. A: Gen* **2003**, *250*, 95.

(23) Rolison, D. R. *Science* **2003**, *299*, 1698.

(24) Ma, R.; Sasaki, T.; Bando, Y. *J. Am. Chem. Soc.* **2004**, *126*, 10382.

(25) Shen, S. C.; Ng, W. K.; Chen, Q.; Zeng, X. T.; Chew, M. Z.; Tan, R. B. H. *J. Nanosci. Nanotechno.* **2007**, *7*, 2726.

(26) Kloprogge, J. T.; Frost, R. L. *Phys. Chem. Chem. Phys.* **1999**, *1*, 1641.

(27) Husing, N.; Schubert, U. *Angew. Chem. Int. Ed* **1998**, *37*, 22.

(28) Pierre, A. C.; Pajonk, G. M. *Chem. Rev.* **2002**, *102*, 4243.

(29) Chen, X.; Mao, S. S. *Chem. Rev.* **2007**, *107*, 2891.

(30) Morales, A. E.; Mora, E. S.; Pal, U. *Rev. Mex. Fis. S* **2007**, *53*, 18.

(31) Liu, S.; Sun, X.; Li, J.-G.; Li, X.; Xiu, Z.; Huo, D. *Eur. J. Inorg. Chem.* **2009**, *2009*, 1214.

(32) Hagfeldt, A.; Gratzel, M. *Chem. Rev.* **1995**, *95*, 49.

(33) Brus, L. *J. Phys. Chem.* **1986**, *90*, 2555.

(34) Kavan, L.; Stoto, T.; Gratzel, M. *J. Phys. Chem.* **1993**, *97*, 9493.

(35) Kormann, C.; Bahnemann, D. W.; Hoffmann, M. R. *J. Phys. Chem.* **1988**, *92*, 5196.

(36) Sakai, N.; Ebina, Y.; Takada, K.; Sasaki, T. *J. Am. Ceram. Soc.* **2004**, *126*, 5851.

(37) Sing, K. S. W.; Everett, D. H.; Haul, R. A. W.; Moscou, L.; Pierotti, R. A.; Rouquerol, J.; Siemieniewska, T. *Pure & Appl. Chem.* **1985**, *57*, 603.

(38) Kruk, M.; Jaroniec, M. *Chem. Mater.* **2001**, *13*, 3169.

(39) Soria, J.; Sanz, J.; Sobrados, I.; Coronado, J. M.; Hernandez-Alonso, M. D.; Fresno, F. *J. Phys. Chem. C* **2010**, *114*, 16534.

(40) Morterra, C. *J. Chem. Soc., Faraday Trans. 1* **1988**, *84*, 1617.

(41) Arrouvel, C.; Digne, M.; Breysse, M.; Toulhoat, H.; Raybaud, P. *J. Catal.* **2004**, *222*, 152.

(42) Turek, A. M.; Wachs, I. E. *J. Phys. Chem.* **1992**, *96*, 5000.

Chapter 6:

Photocatalysis of TiO_2-Al_2O_3 core-shell nanocomposites with different morphologies

6.1 INTRODUCTION

Since the elucidation of the photocatalytic splitting of water on TiO_2 electrode under ultraviolet (UV) light by Fujishima and Honda[1], considerable efforts have been devoted to the research of TiO_2 materials mainly for its uses in emerging energy and environmental technologies[2]. These technologies include, but are not limited to, dye sensitized solar cells (DSSC)[3], organic photovoltaics (OPV), photocatalysis for direct hydrogen production[4] and pollutant photocatalytic degradation[5]. Using TiO_2 as photocatalyst to degrade low concentration but persistent organic pollutants provides an attractive and economically feasible approach for water purification under UV irradiations.

Traditional photocatalytic systems are based on the ultrafine powders or colloidal catalysts[6-8], which, however, are inherently defective in that they may agglomerate together during the decomposition reactions resulting in the deterioration of catalytic performance[9]. Moreover, the recovery of colloid particles from aqueous solutions for reuse is vexingly difficult. Various approaches to develop efficient, sustainable catalysts have been undertaken. These approaches include preparing and attaching the active components on various kinds of carriers such as fragments of clay layers[10], SBA-15 mesoporous molecular sieves[11,12], silica[13,14], alumina[15,16] or activated carbon[17]. There is a potential problem using traditional porous materials as support for photocatalytic reactions in that the light cannot penetrate through the pore walls to excite the TiO_2 nanocrystallites.

Recently, fabricating photocatalysts into a hierarchical structure in order to enhance its performance has attracted considerable attention. For example, Belcher and co-workers[18] used biological scaffolds as templates in order to incorporate a photocatalytic active

component for water splitting. Gao and co-workers[19] fabricated 1D hierarchical titania by coating protonated titanate nanoparticles on titanate nanorods followed by calcinations at various temperatures. In these two cases, the core-shell structure fabricated by attaching the active components to the surface of their respective carrier eliminates the adverse effects of the carrier sheltering the active component from light irradiation.

In the previous chapter, we synthesised a series of hierarchical TiO_2/Al_2O_3 nanocomposite with different morphologies including fibrous TiO_2/Al_2O_3 nanocomposites with core-shell structures, where anatase nanocrystallites were incorporated onto long bundles of alumina nanofibres, and TiO_2 mircospheres which were separated by alumina nanofibres. Given that the performance of titania in photocatalysis could be optimised by the morphology of the materials, core-shell structure of the fibrous nanocomposites could result in improved photocatalytic performance. In this chapter, we evaluate these as-synthesised nanocomposites by means of the photodegradation of phenol and sulforhodamine B dye under UV irradiation. We try to relate the catalytic performance to the characteristics of their morphologies, crystal sizes, surface areas.

6.2 EXPERIMENTAL SECTION

Catalyst preparation: Catalyst preparation has been mentioned in Chapter 5. For convenience, the comparison of physical properties of these nanocomposites is briefly listed quantitatively in Table 1. The meaning of their labels and specific morphology can be retrieved from Chapter 5. Briefly, these samples were labelled as Ti-"m"-T, where m is Ti/Al molar ratios and T is calcined temperature. For example, the sample labelled as Ti-2-750 indicated that Ti/Al molar ratio of this sample was 2, and it was crystallized by the calcinations at 750 ^{o}C. A specific sample was labeled as a-Ti-1-450, because this sample had a densely agglomerate morphology which had been introduced in chapter 5.

Table 1. Physical properties of resultant TiO_2/Al_2O_3 nanocomposites

Sample name	E_g	Specific surface area m^2/g	Crystal size of anatase phase
a-Ti-1-450	3.17	141	8.4 nm
Ti-1-450	3.40	159	7.3 nm
Ti-2.0-450	3.30	119	9.5 nm
Ti-3.0-450	3.21	84	14.4 nm

Photocatalytic activity test: The photocatalytic activity of the powder sample was evaluated in a three-phase fluid bed photoreactor. The UV light source equipped was a 38 W Hg lamp (NEC, FL15BL T8), the wavelength spectra of which was portrayed in Figure 1. The predominant peak was centered at about 356 nm. Phenol or sulforhodamine B aqueous solutions were used as model pollutants. The catalyst concentration was 0.5 g/L and the initial concentration of pollutant was 25 ppm for phenol or 1.8×10^{-5} M for sulforhodamine B. Prior to irradiation, the reactive solution was kept in the dark for a period of time, with air bubbled through, in order to achieve an adsorption-desorption equilibrium. At regular irradiation time intervals, the dispersion was sampled and filtered through a Millipore filter to remove the catalyst particles. The phenol concentration was analyzed by a high performance liquid chromatograph equipped with an Eclipse XDB-C8 column (Acetonitrile and 0.1% acetic acid solution were used as eluents), while that of the dye was monitored by colormetry using a UV-visible spectrometer.

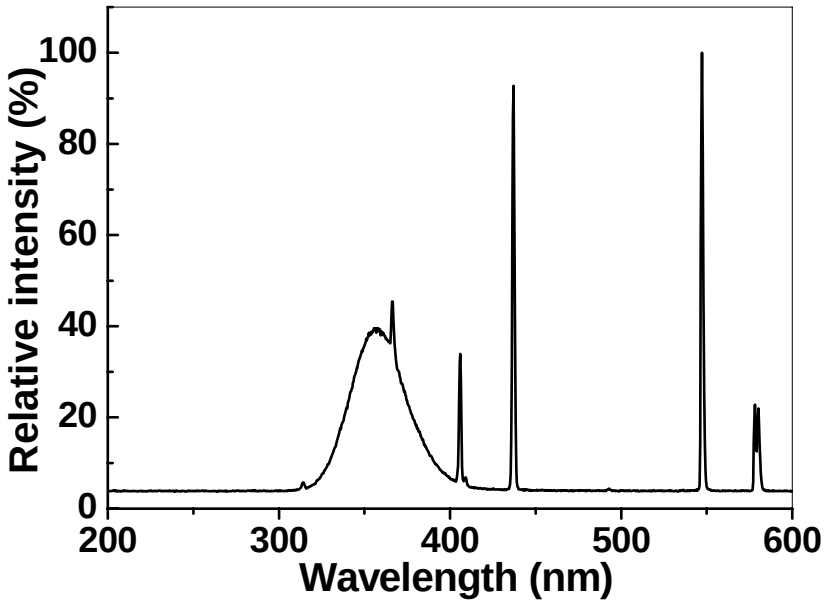

Figure 1. Wavelength spectra of the light sources

6.3 RESULT AND DISCUSSION

EFFECTS OF CATALYST MORPHOLOGIES

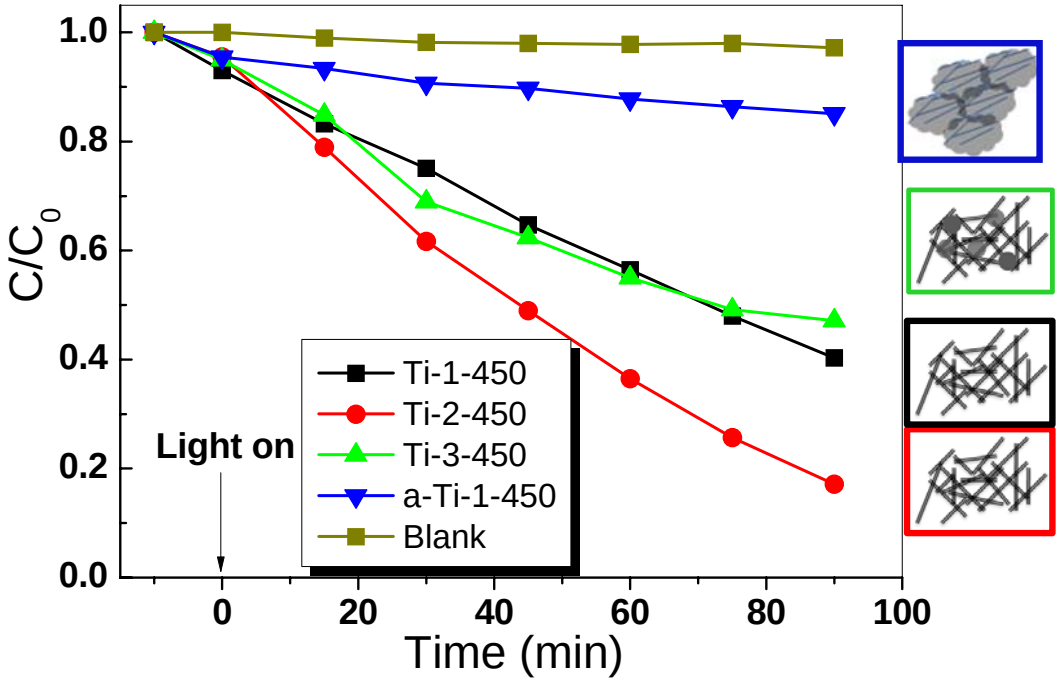

Figure 2. Temporal course of the photodegradation of the phenol in the presence of TiO_2/Al_2O_3 nanocomposites with various Ti/Al molar ratios with all the samples calcined at 450°C

From the data displayed in Figure 2, all the samples exhibit photocatalytic capability for phenol degradation to differing extents and the photodegradation of phenol without catalyst is negligible. For the fibrous TiO_2/Al_2O_3 nanocomposites, Ti-1-450 and Ti-2-450, the photocatalytic performance is strongly enhanced by the increase of Ti/Al molar ratio. The Ti-2-450 can degrade more than 80% of phenol in 90 min, while the sample Ti-1-450 can only degrade phenol about 40% in the same time. It is worth noting here that the sample a-Ti-1-450 possesses the same Ti/Al molar ratio and similar specific surface area as Ti-1-450 (sample with fibrous morphology), but its photocatalytic activity is relatively low (only 10 % of degradation) due to the densely agglomerated structure. Moreover, the sample Ti-3-450 has the highest Ti/Al molar ratio and it is comprised of many TiO_2 microspheres, about 0.5 μ in diameter, which are also highly dispersed into the pollutant solution. However, the photocatalytic activity of this sample is only close to Ti-1-450.

According to Serpone's work[20], the reaction kinetics of phenol photodegradation can be described by a modified Langmuir-Hinshelwood model in favor of a surface reaction, which is shown as follows.

$$\ln\frac{C_0}{C} + k(C_0 - C) = k_r K t \qquad (1)$$

Where C is the pollutant concentration, C_0 is its initial value; K is its adsorption coefficient while k_r is the reaction rate constant. The equation is the sum of zero-order and first-order rate equations, and the contribution of these two parts depends essentially on the initial concentration C_0. As generally the initial concentration of pollutant for photocatalysis is very small, the equation is further reduced to the pseudo-first order reaction.

$$\ln\frac{C_0}{C} = k't \qquad (2)$$

k' is the apparent first-order rate constant, the plot of $\ln(C/C_0)$ versus irradiation time gives a straight line, of which the slope equals to the *k'*.

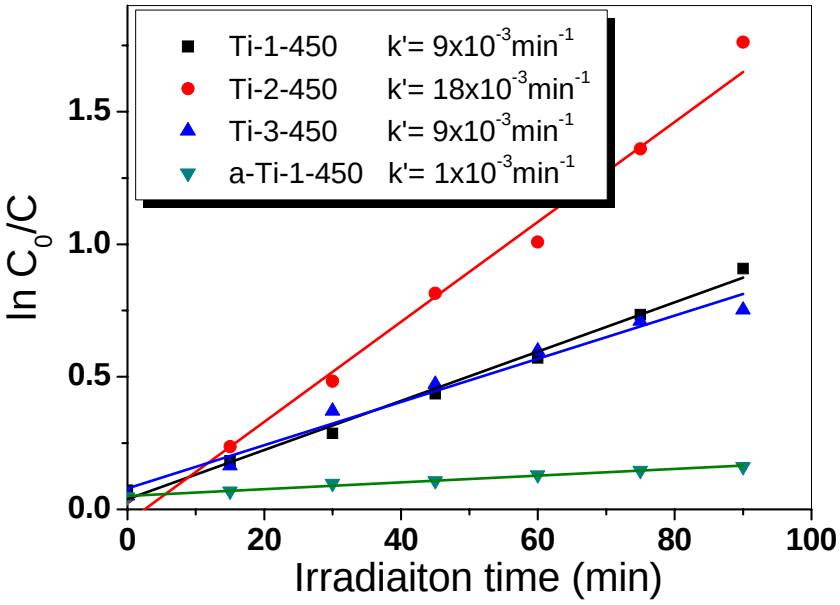

Figure 3. Linear fitness of the kinetics of phenol degradation for various catalysts during irradiation

Figure 3 illustrates the evolution of ln(C_0/C) as a function of irradiation time which is plotted from the data in Figure 2. Again a pseudo-first order reaction rate of the phenol photodegradation is verified. The differences in efficiencies for various catalysts cannot simply be attributed to their different band gap energy because of the catalyst with fibrous morphology possessing a large band gap but exhibiting high catalytic efficiency. Furthermore, as investigated in the effect of calcination temperatures, our experiments confirm that the catalytic performance of Ti-2-450 can be improved by increasing its crystal size of anatase, which can also exclude the possibility that the low catalytic activity of Ti-3-450 comparing with Ti-2-450 is due to the relative larger crystal size and the simultaneous decrease in surface area of Ti-3-450. Therefore, the only explanation for their different catalytic efficiencies is due to their different morphologies which results in different irradiation areas.

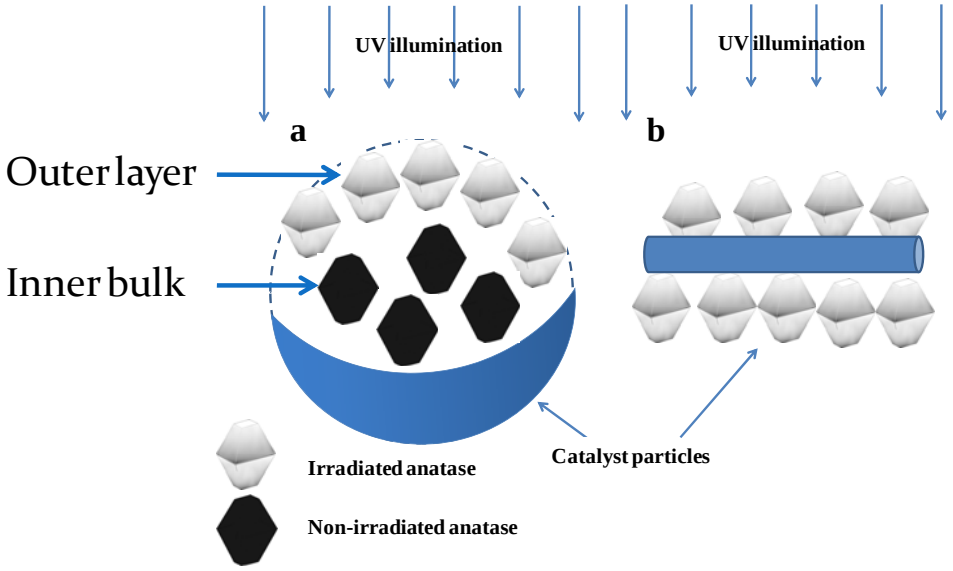

Scheme 1. Schematic of the morphological effects for these catalysts with various Ti/Al molar ratios a) catalyst with mircospheric morphology and b) catalyst with fibrous morphology

As we showed in Scheme 1, although the Ti-3-50 possesses more photoactive sites than other samples due to its highest Ti content and relatively large anatase crystal size, its spherical morphology leads to the possibility that many anatase nanocrystallites cannot be irradiated by UV light and the phenol pollutant can only be degraded on the first layer of anatase nanocrystallites. In contrast, for the nanocomposites with fibrous morphology, almost all anatase nanocrystallites are exposed on their outer surfaces and can be readily illuminated by UV light. Therefore, in this work, the overall photocatalytic efficiency of the nanocomposites with fibrous morphology is significantly better than that of the samples without.

The photocatalytic activities of all these nanocomposites are also evaluated by the degradation of sulforhodamine B dye. Dyes have more complicated chemical structures compared with phenol and most of them have light absorption in the visible range as well as in UV range (Figure 4). Therefore, the photo-degradation of dyes is usually faster than that

of phenol under UV-irradiation and also can be achieved under visible light illumination. The mechanism for dye degradation under visible light irradiation has been extensively studied[21,22], where dyes, rather than photocatalysts, are excited by visible light to appropriate singlet and triplet states, followed by electron injection into the conduction band of semiconductor.

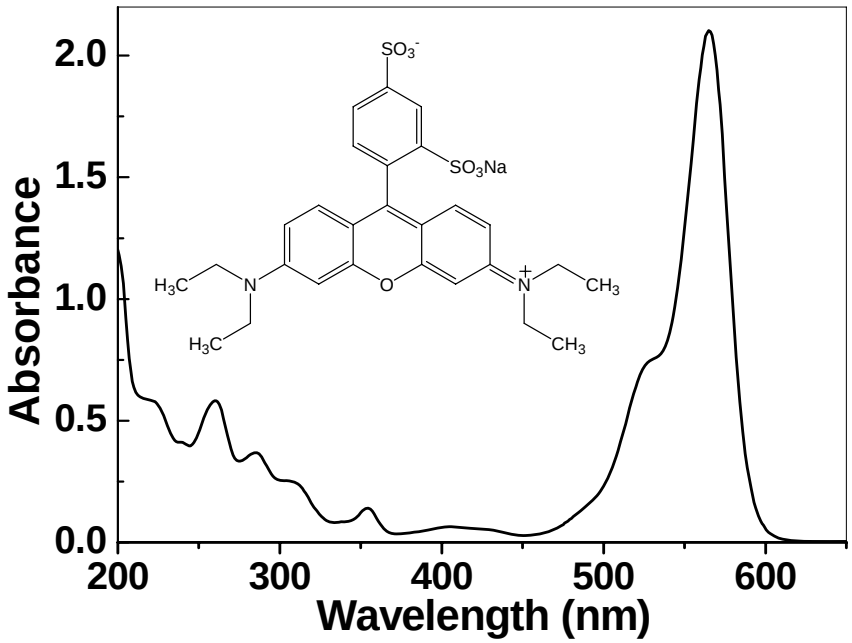

Figure 4. Uv-visible absorption band of sulforhodamine-B and its chemical structures

As shown in Scheme 2, for sulforhodamine-B, the oxidation potential (E ($SRB^{*}/SRB^{+\bullet}$)) is -1.30 V vs. NHE, which locates above the conduction band edge of TiO_2 at -0.5 V vs. NHE[23]. The potentials for reduction of oxygen to superoxide ion (E ($O_2/O_2^{-\bullet}$)) and for reduction of H_2O_2 to hydroxyl radical are -0.15 and 0.3 V vs. NHE respectively[24,25], which are also below the conduction band edge of TiO_2. Therefore, the light-excited dyes can inject electrons to the conduction band of TiO_2, and the electron can react with oxygen generating hydroxyl radicals that are highly oxidative and non-selective in order to decompose many organic compounds.

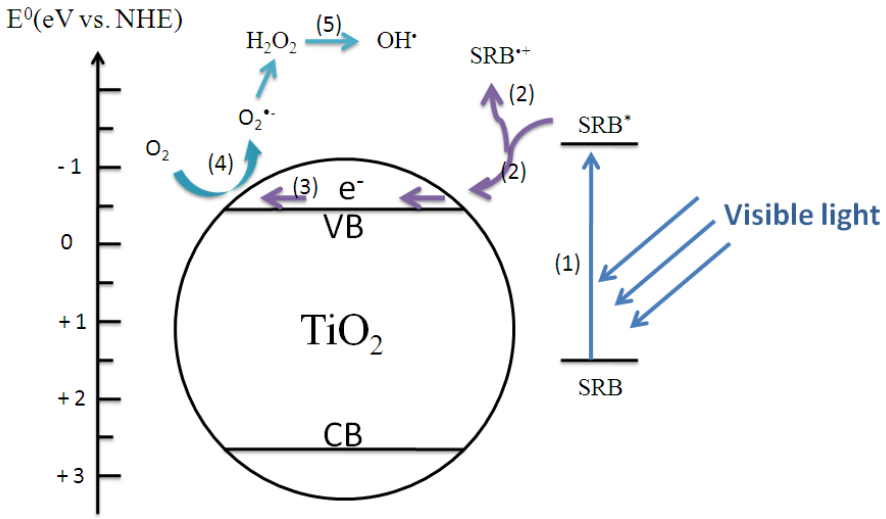

Scheme 2. Schematic mechanism of the photodegradation of SRB on TiO_2 particles under visible light irradiation[26]

The photoactivities sequence of SRB dye degradations for all these nanocomposites is similar to that of the phenol degradation: for fibrous photocatalysts, the catalytic performance is improved as the Ti/Al molar ratio increases from 1 to 2. While the Ti/Al molar ratio increase to 3, the catalyst changes its morphology to microsphere, therefore its catalytic performance decreases. This trend could also be attributed to the difference in the irradiated surface area of TiO_2 for the catalysts with various Ti/Al molar ratio, indicating that the SRB dye degradation under UV irradiation mainly corresponds to the semiconductor electronic excitation pathway.

However, the catalytic performance of Ti-3-450 seems to be enhanced in dye degradation, which is similar to that of Ti-1-450 in phenol degradation but is higher in dyes degradation. It should be emphasized here, because the degradation of phenol or dyes for all samples was carried out under the same conditions (catalyst concentration, air flow rate), the catalytic performances for these two samples (Ti-1-450 and Ti-3-450) were observed to be reproducible. The adsorptive capacity of all these nanocomposites for SRB dyes and phenol is very similar. The discrepancy in catalytic performance between the degradation of phenol

and SRB dye is possibly related to the specific photodegradation mechanism of the pollutant. The dye mechanism aforementioned was proposed for the visible light photocatalytic reaction but should also work in the dye's UV light photodegradation since the SRB dye absorption extends into the UV range as well.

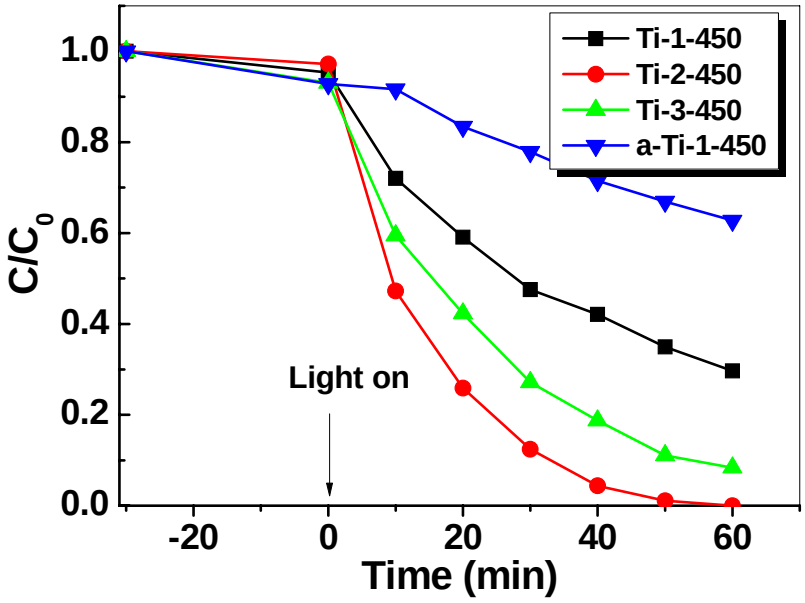

Figure 5. Temporal course of the photodegradation of the sulforhodamine B

In this work, we proposed that the morphology effect also exerts a role, at least to some extent. As shown in Scheme 3, compared with phenol degradation, the dye degradation proceeds by an alternative mechanism: initially, during the UV irradiation, the SRB dye mainly degrades on the irradiated anatase nanocrystallites which lie on the surface of titania particles. Secondly, the excited dyes can also diffuse into titania particulates and inject electrons into some nonirradiated anatase nanocrystallites which are located on the sublayer of the titania particulates. Further to this injection, the electron is scavenged by oxygen molecules and transformed into the highly active OH radical. Since there are less obscured anatase nanocrystallites in the sample with fibrous morphology, the latter process is only effective for Ti-3-450 whose mircospheric morphology indicates that many active sites cannot be irradiated during the photocatalytic reaction. This results in a discrepancy in

catalytic performances between the degradation of phenol and SRB dye for Ti-1-450 and Ti-3-450.

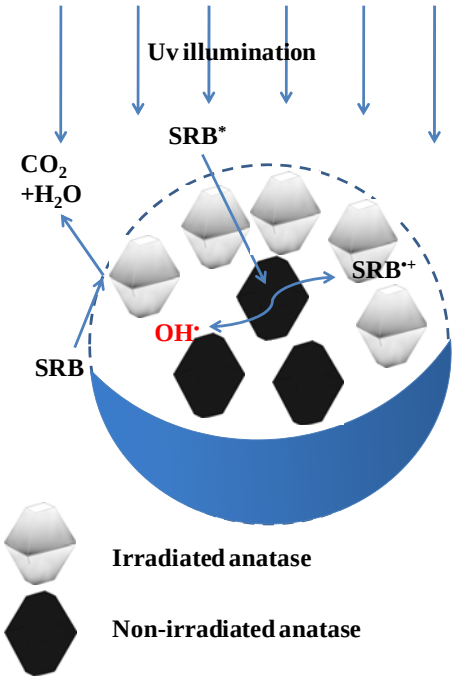

Scheme 3. Proposed enhanced mechanism of dye degradation on Ti-3-450 under UV irradiation

THE EFFECT OF CALCINATION TEMPERATURE

The key function for a heterogeneous photocatalysis is to generate a light-induced charge pair (e^- and h^+) separation, whose lifetime is of such stability as to facilitate redox chemistries. One key method of improving the performance of a photocatalyst is to provide a strategy which prevents the recombination of the separated charge pair[27,28]. For a pristine homo-semiconductor, the only readily available method is to improve its crystallinity in order to reduce the amount of crystal defect sites where the recombination readily occurs. However, calcination, which is usually utilised for this purpose, is deleterious, and results in the sintering of nanocrystallites[29].

The as-syntheisized TiO_2/Al_2O_3 nanocomposites possess a novel core-shell structure where the anatase nanocrystallites are evenly dispersed on the long bundles of alumina

nanofibres. The long alumina bundles act as hard templates and provide good mechanical and thermal stability to the materials. It is this increased stability that allows the preparation of highly crystalline TiO_2 nanoparticles by simple calcination without forming an undesired, agglomerated morphology. Thus, crystal size, distribution and dispersion can be precisely controlled in the as-synthesised material.

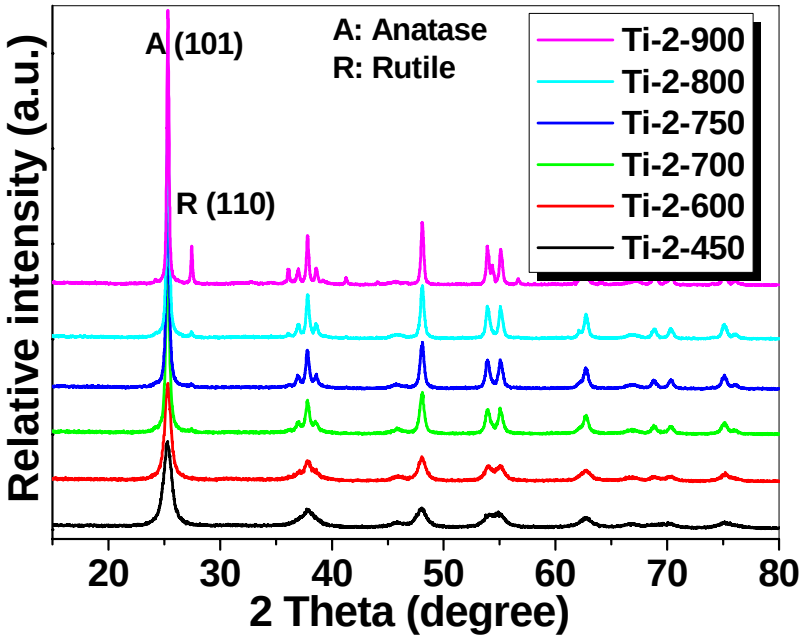

Figure 6. XRD patterns for the sample with 2 Ti/Al molar ratios calcined from 450°C to 900°C

Ti-2-450 exhibits the highest catalytic activity for the degradation of phenol under UV irradiation. Therefore, the fibrous nanocomposite with Ti/Al molar ratio m=2 is calcined from 450°C to 900°C. Even after calcination at 900°C, the prepared sample is still a flocculent white powder. In Figure 6, the XRD patterns of the calcined composites are given. Notably, the main crystal phase for all nanocomposites is anatase, with the calcination temperature elevating the intensity of diffractions characteristic of anatase phase dramatically. This intensity increase is indicative of increasing crystallinity. For the samples calcined above 700°C, their XRD patterns show a small portion of rutile phase present along

with anatase TiO_2. The phase contents were estimated from the respective XRD peak intensities using the following equation[30]:

$$f_A = \frac{1}{(1 + \frac{1}{K}\frac{I_R}{I_A})}$$

Where f_A is the fraction of the anatase phase; K = 0.79 since anatase is the predominant crystal phase in this sample. I_R and I_A are the integrated intensities of the rutile [110] and anatase [101] peaks, respectively.

The average crystallite size of TiO_2 was estimated by means of the Scherrer equation from the diffraction peaks [110] for rutile and [101] for anatase, and summarised in Table 2 with their respective phase content.

Table 2. Crystal sizes and phase component of the fibrous nanocomposites (Ti/Al=2) calcined at various temperatures

Sample name	XRD calculation		Phase (%)[a]	
	Anatase	Rutile	Anatase	Rutile
Ti-2-450	9.5 nm	—	100	—
Ti-2-600	12.6 nm	—	100	—
Ti-2-700	21.5 nm	27.6 nm	96	4
Ti-2-750	25.1 nm	27.9 nm	96	4
Ti-2-800	28.4 nm	37.3 nm	96	4
Ti-2-900	41.3 nm	59.3 nm	84	16

It can be observed that the crystal size of the anatase increases slightly from 9.5 nm to 12.6 nm when increasing the calcination temperature from 450°C to 600°C. However, when the calcination temperature increases from 600°C to 700°C, the crystal size of anatase

dramatically increases to 21.5 nm and from 700°C to 900°C, each 100°C increment leads to about 10 nm in coarsening for anatase nanocrystallites. In addition, the samples contain 4 % rutile phase when calcined in the temperature range from 700°C to 800°C, while for the sample calcined at 900°C, the percentage of rutile phase in this sample is about 84% and its crystal size is about 59.3 nm.

The diffuse reflectance UV-visible spectra for the calcined nanocomposites and commercial TiO_2 P25 are shown in Figure 7, where all spectra of samples were obtained at the same conditions. The absorption edges for the nanocomposites calcined from 450°C to 800°C are almost overlapping, which is notably similar to that of commercial TiO_2, P25. The evident difference between the calcined samples from 450°C to 800°C is that the absorption band, which is centred at 225 nm, gradually decreases as the calcination temperature of samples increases, while the P25 has the highest intensity of this band. This band corresponds to the isolated Ti species[31], indicating that the crystallization of TiO_2 happened at the expense of isolated Ti species as the calcination temperature increases.

The diffuse reflectance spectra for the sample calcined at 900°C exhibits distinct red shift of absorption edges. The absorption edge is estimated by plotting $[F(R_\infty)\cdot E]^{1/2}$ against E, where $E=h\nu$ represents the photoenergy, and $F(R_\infty)$ is the so-called remission or Kubelka-Munk function, and extrapolating the straight, linear portion of the spectra to $[F(R_\infty)\cdot E]^{1/2}=0$. Two band gaps about 3.0 and 3.2 respectively can be extracted from the spectra for Ti-2-900, indicating the red shift of this sample corresponds to the formation of rutile phase.

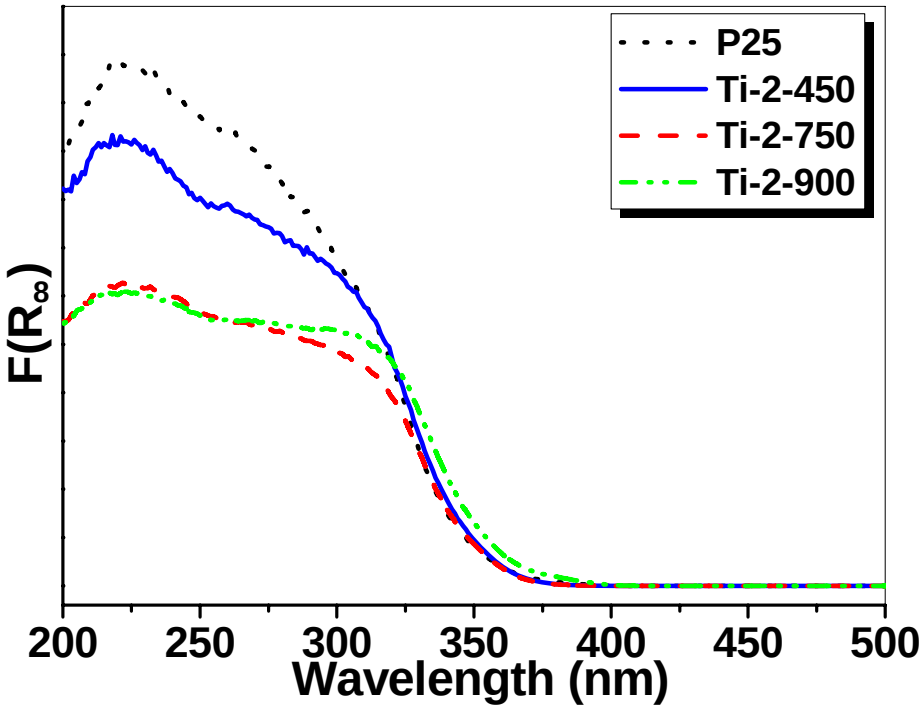

Figure 7. UV-visible spectra of calcined TiO_2/Al_2O_3 nanocomposites (Ti/Al=2)

The photoactivities of the calcined nanocomposites and commercial TiO_2 P25 for degradation of phenol are shown in Figure 8; apparent first-order rate constants of these samples are also calculated. It can be observed that the catalytic performances of these nanocomposites are promoted by elevating the calcination temperature up to 750^{o}C, whereas above this calcination temperature, their activities begin to drop back markedly. The sample calcined at 750^{o}C exhibits the highest activity, which can totally degrade 25 ppm phenol in 90 min. In contrast, for the commercial TiO_2 P25, the total degradation of 25 ppm phenol is finished in 60 min.

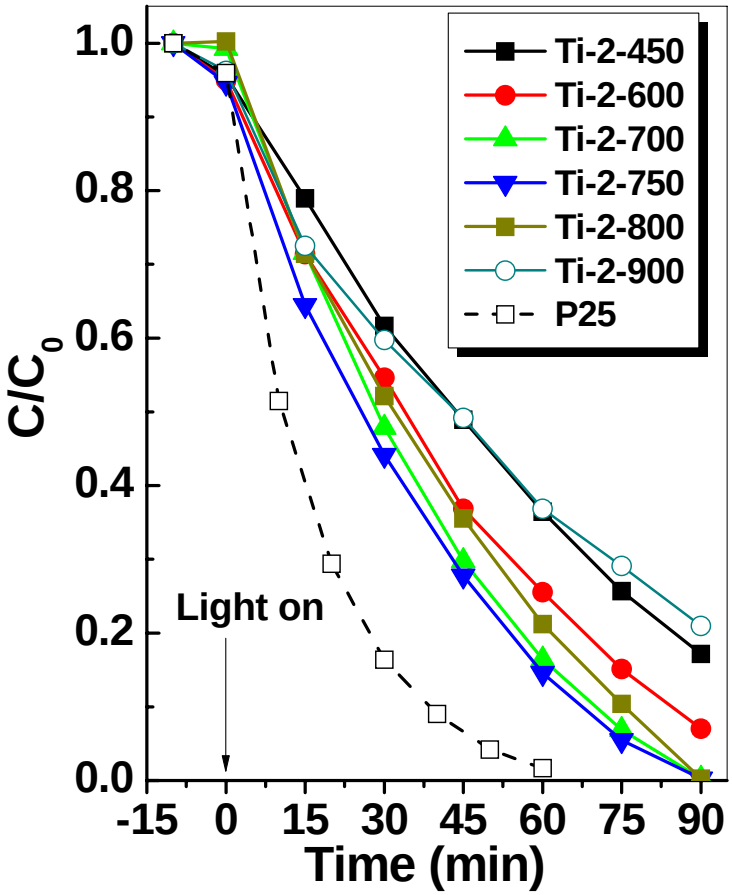

Figure 8. Temporal course of the photodegradation of phenol for the calcined nanocomposites (Ti/Al=2)

In this work, the photoactivities of these calcined nanocomposites is not as high as P25, but it should be noticed here that these nanocomposites contain a definite amount of alumina, of which the Ti/Al molar ratio is 2 and the mass percentage of TiO_2 is 75%. Moreover, as shown in Figure 9, the crystal size growth also results in the decrease of surface areas. Due to the fibrous morphology of these materials, all their surface areas can be regarded as exposed-surface area that is capable of harvesting light. Therefore, the turnover frequency based on the TiO_2 unit and surface areas is also calculated from the initial activity of the phenol degradation and summarised on Table 3.

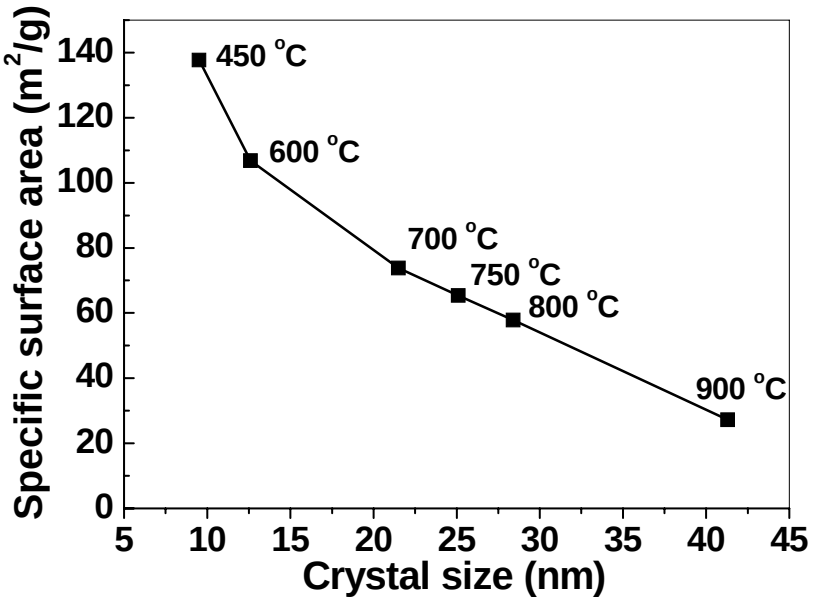

Figure 9. Specific surface area of calcined nanocomposites as a function of crystal sizes

Table 3. Rate constant and turnover frequency (initial activities) in the photodegradation of phenol over calcined nanocomposites

Sample name	k $10^{-3}min^{-1}$	Turnover frequency	
		TiO_2 unit $10^{-3}min^{-1}$	Surface area mol/m^2
Ti-2-450	18	1.02	6.95×10^{-8}
Ti-2-600	27	1.53	13.4×10^{-8}
Ti-2-700	34	1.92	24.5×10^{-8}
Ti-2-750	39	2.21	31.4×10^{-8}
Ti-2-800	29	1.64	26.6×10^{-8}
Ti-2-900	16	0.91	31.2×10^{-8}
P25	63	2.67	55.8×10^{-8}

Observed from Table 3, the turnover frequencies, which are based on surface area for the calcined nanocomposite catalysts are relatively low compared with P25. Clearly, the surface of P25 is more efficient for harvesting and utilising irradiated photons. However, the activity per unit of TiO_2 for the sample Ti-2-750 is very close to that of P25. This could be attributed to their fibrous morphology resulting in minimal agglomeration of anatase nanocrystallites.

In previous work, it was observed in several research groups[32,33] that catalysts with fibrous morphology can be separated easily from the aqueous system by sedimentation. In this work, we witnessed that as-prepared fibrous photocatalysts are more readily recovered by a simple filtration, compared with commercial P25. This is because, although the fibrous materials are aggregated in the filtration procedure, their morphologies also make the filtration cake contain large interparticle voids that can support a high filtration flux. In contrast, ultrafine powders or dispersed nanocrystallite easily peneterates and blocks the filter which leads to the high cost for separation at industrial scale.

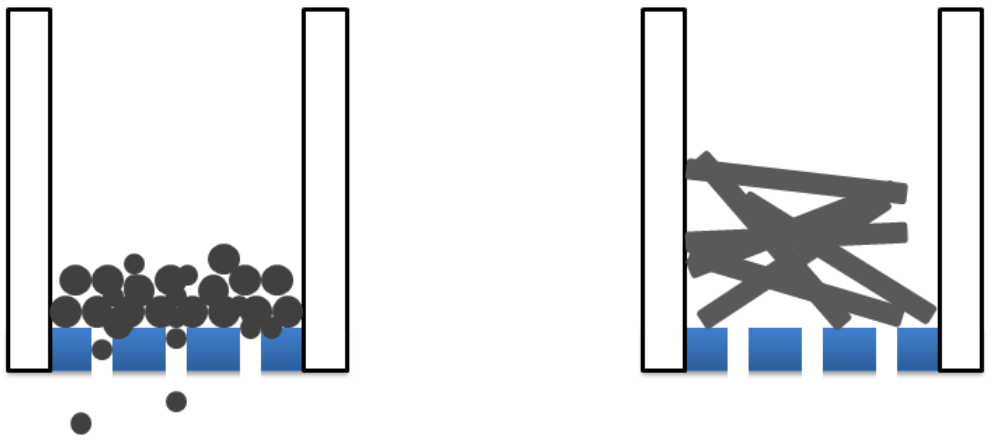

Scheme 4. Schematic shows that the fibrous catalyst can be separated readily and rapidly for reuse by filtration

6.4 CONCLUSION

In summary, we observed that the morphology for a photocatalyst is of critical importance. Three kinds of morphologies were investigated in this work. They are densely aggregated particles, highly separated TiO_2 microspheres and fibrous samples. Among them, the catalyst with fibrous morphology exhibits superior catalytic performance. This could be attributed to two factors. Firstly, TiO_2 nanocrystallites are evenly dispersed over the alumina bundles and all or a majority of them are exposed to light irradiation. Secondly, the particles with fibrous morphology could be easily dispersed into the reaction system rather than sedimentation, occuring as a result of bulk particles or aggregation of small nanocrystallites, and maximizes the light harvesting and the transportation of reactant molecular to active sites.

Furthermore, we optimized the catalytic performance by calcinations at elevated temperature. The samples were always flocculent white powders rather than sintered aggregates, exhibiting a good thermal stability of as-prepared nanocomposites. The sample calcined at 750^{o}C exhibits the highest activity, of which the initial activity (TOF) per unit of TiO_2 was very close to that of commercial P25. The fibrous morphology of as-prepared nanocomposites has an additional advantage in that they can be recovered readily and rapidly by filtration. The knowledge acquired in this work is important for designing novel photocatalysts that could combine high efficiency with rapid recoverability.

6.5 REFERENCE AND NOTES

(1) Fujishima, A.; Honda, K. *Nature* **1972**, *238*, 37.

(2) Chen, X.; Mao, S. S. *Chem. Rev.* **2007**, *107*, 2891.

(3) Hagfeldt, A.; Boschloo, G.; Sun, L.; Kloo, L.; Pettersson, H. *Chem. Rev.* **2010**, *110*, 6595.

(4) Esswein, A. J.; Nocera, D. G. *Chem. Rev.* **2007**, *107*, 4022.

(5) Hoffmann, M. R.; Martin, S. T.; Choi, W.; Bahnemann, D. W. *Chem. Rev.* **1995**, *95*, 69.

(6) Ohno, T.; Sarukawa, K.; Tokieda, K.; Matsumura, M. *J. Catal.* **2001**, *203*, 82.

(7) Linsebigler, A. L.; Lu, G.; Jr, J. T. Y. *Chem. Rev.* **1995**, *95*, 735.

(8) Hagfeldt, A.; Gratzel, M. *Chem. Rev.* **1995**, *95*, 49.

(9) Beydoun, D.; Amal, R. *J. Phys. Chem. B* **2000**, *104*, 4387.

(10) Yang, X.; Yang, D.; Zhu, H.; Liu, J.; Martins, W. N.; Frost, R.; Daniel, L.; Shen, Y. *J. Phys. Chem. C* **2009**, *113*, 8243.

(11) Ding, H.; Sun, H.; Shan, Y. *J. Photoch. Photobio. A* **2005**, *169*, 101.

(12) Wang, Z.; Zhang, F.; Yang, Y.; Xue, B.; Cai, J.; Guan, N. *Chem. Mater.* **2007**, *19*, 3286.

(13) Lim, T.-H.; Kim, S.-D. *Korean J. Chem. Eng.* **2002**, *19*, 1072.

(14) Pucher, P.; Benmami, M.; Azouani, R.; Krammer, G.; Chhor, K.; Bocquet, J.-F.; Kanaev, A. V. *Appl. Catal. A: Gen* **2007**, *332*, 297.

(15) Anderson, C.; Bard, A. J. *J, Phys. Chem. B* **1997**, *101*, 2611.

(16) Choi, H.; Stathatos, E.; Dionysiou, D. D. *Desalination* **2007**, *202*, 199.

(17) Cao, X.; Oda, Y.; Shiraishi, F. *Chem. Eng. J.* **2010**, *156*, 98.

(18) Nam, Y. S.; Magyar, A. P.; Lee, D.; Kim, J.-W.; Yun, D. S.; Park, H.; Jr, T. S. P.; Weitz, D. A.; Belcher, A. M. *Nat. Nanotechnol.* **2010**, *5*, 340.

(19) Qu, J.; Li, G. R.; Gao, X. P. *Energy Environ. Sci.* **2010**.

(20) Al-Ekabi, H.; Serpone, N. *J. Phys. Chem.* **1988**, *92*, 5726.

(21) Zhao, J.; Chen, C.; Ma, W. *Top. Catal.* **2005**, *35*, 269.

(22) Zhao, W.; Chen, C.; Li, X.; Zhao, J. *J. Phys. Chem. B* **2002**, *106*, 5022.

(23) Liu, G.; Li, X.; Zhao, J. *Environ. Sci. Technol.* **2000**, *34*, 3982.

(24) He, J.; Zhao, J.; Hidaka, H.; Serpone, N. *J. Chem. Soc., Faraday Trans.* **1998**, *94*, 2375.

(25) Jaeger, C. D.; Bard, A. J. *J. Phys. Chem.* **1979**, *83*, 3146.

(26) Fang, Y.; Huang, Y.; Liu, D.; Huang, Y.; Gao, W.; David, J. *J. Environ. Sci.* **2007**, *19*, 97.

(27) Fujishima, A.; Zhang, X.; Tryk, D. A. *Surf. Sci. Rep.* **2008**, *63*, 515.

(28) Ohtani, B.; Ogawa, Y.; Nishimoto, S.-i. *J. Phys. Chem. B* **1997**, *101*, 3746.

(29) Sin, A.; Odier, P. *Adv. Mater.* **2000**, *12*, 649.

(30) Scotti, R.; Bellobono, I. R.; Canevali, C.; Cannas, C.; Catti, M.; Arienzo, M. D.; Musinu, A.; Polizzi, S.; Sommariva, M.; Testino, A.; Marazzoni, F. *Chem. Mater.* **2008**, *20*, 4051.

(31) Zhang, W.; Froba, M.; Wang, J.; Tanev, P. T.; Wong, J.; Pinnavaia, T. J. *J. Am. Chem. Soc.* **1996**, *118*, 9164.

(32) Li, J.; Ma, W.; Chen, C.; Zhao, J.; Zhu, H.; Gao, X. *J. Mol. Catal. A: Chem.* **2007**, *261*, 131.

(33) Yang, D.; Liu, H.; Zheng, Z.; Yuan, Y.; Zhao, J.-c.; Waclawik, E. R.; Ke, X.; Zhu, H. *J. Am. Chem. Soc.* **2009**, *131*, 17885.

Chapter 7:

Conclusions

In this thesis, we developed a new strategy to prepare hierarchical macro-mesoporous nanocomposites without the use of any organic space filler\template or other specific technologies. Two kinds of fibrous ZrO_2/Al_2O_3 and TiO_2/Al_2O_3 nanocomposites were successfully synthesised using boehmite nanofibers as a hard temperate followed by a simple calcination. Verified by TEM, the nanocomposites possess a novel core-shell structure where a ZrO_2 or TiO_2 shell is evenly distributed onto a core of long, bundled alumina nanofibres. The core of fibrous alumina of the resultant nanocomposite provides the material with considerable mechanical and thermal stability, and, more importantly, the growth of metal oxide nanocrystallites is also inhibited by the metal oxide/alumina interface during additional calcination, which results in an even distribution of the crystallites of metal oxide.

Interestingly, the stacking of resulting materials is a hierarchical macro-mesoporous nanocomposite: the assembly of nanocrystallites forming a mesoporous layers enveloped the alumina bundles and the bundles of coated, fibrous alumina aggregate generating the macroporous framework of the nanocomposites. To the best of our knowledge, this nanostructure has never been reported previously. In addition, the nanocomposites can be prepared with extremely high Zr or Ti to Al molar ratios which, in this thesis, are 1:1 for zirconia materials and 2:1 for titania materials. Thanks to the core-shell structure, the surface properties of nanocomposite are close to that of the pristine transition metal oxide while the molar ratio of the materials determined by XPS is above three times as much as the bulk value indicating the availability of the catalytically active component.

To better understand the formation of the unique nanostructure of these fibrous nanocomposites (1D), we combine several characterisation approaches, such as SEM, TEM, Hot-stage Raman, FT-IR emission spectroscopy and solid-state ^{27}Al MAS NMR spectra to trace the preparation procedures:

The process starts with the preparation of dispersive system of boehmite nanofibres. The dispersibility of boehmite nanofibres was briefly introduced in Chapter 2. The boehmite nanofibres can form a stable suspension in aqueous solution (Scheme 1b) but usually flocculate in organic solution (Scheme 1a). Just as with normal colloid particles, the dispersion of boehmite nanofibres in an aqueous solution is a sensitive balance between repulsive interparticle forces associated with the electrical double-layer around the particles and the attractive van der Waals forces as described in Derjaguin-Landau-Verwey-Overbeek theory (DLVO). In this work, by adsorbing a thin layer of water molecules onto the surface hydroxyl groups of boehmite nanocrystallites, we can prepare evenly dispersed bundles of boehmite nanofibers in a hydrophobic organic medium (Scheme 1c).

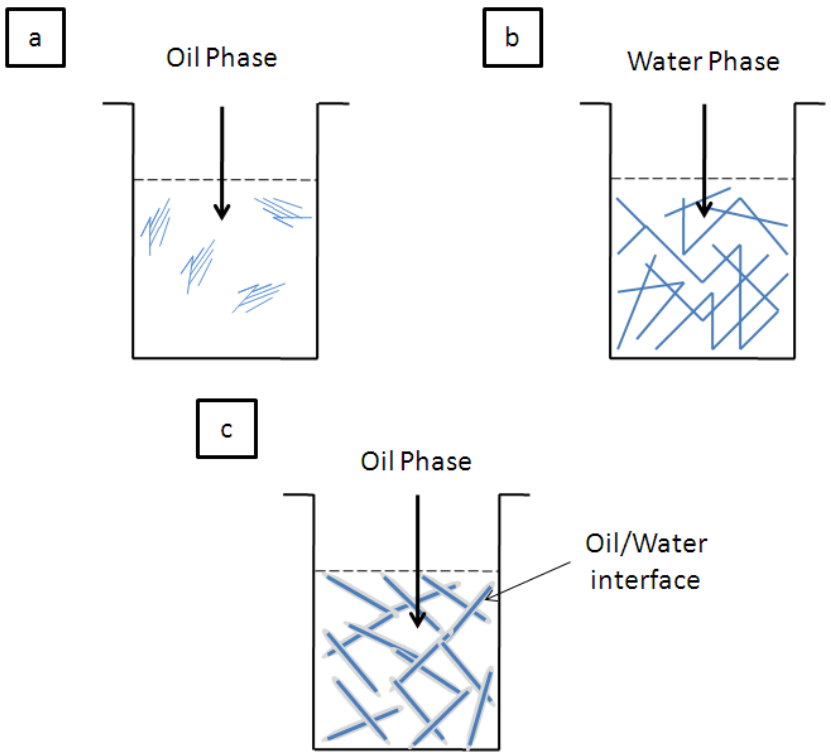

Scheme 1. The suspension state of boehmite nanoifibres a) in oil phase b) in water phase,and c) in oil phase with the aid of oil/water interface

This case should be regarded as a hydrated aggregation of hydrophilic particles dispersed in a hydrophobic medium. Since the Van der Waals attraction force on close approach of two

nanoparticles is extremely large, separating the aggregation of nanoparticles inevitably requires some considerable force. The repulsive hydration force, which arises between two surfaces when water molecules orient with and bind to the hydrophilic surface forming a hydration layer around nanoparticles, is necessary to separate the hydrophilic surface of two overlapped particles. Meanwhile, the lack of corresponding repulsion is just the fundamental reason that dry boehmite nanofibres are prone to aggregation in oil phase[1].

The repulsive hydration force is a short-range force. This force increases with the water molecule in the hydration layer around nanoparticles being squeezed out. The the strength of this force depends largely on the energy required to dehydrate these hydrophilic groups. Empirically, the repulsive hydration energy (per unit area) follows an exponential decay:

$$W_a^H(D) = W_0 \exp\left(-\frac{D}{\lambda_0}\right)$$

Where D is a surface separation, W_0= 3-30 mJm^{-2} and λ_0, 0.6 -1.1 nm, is the decay length. As measured experimentally, the effective range of hydration forces is ~ 3 nm^2.

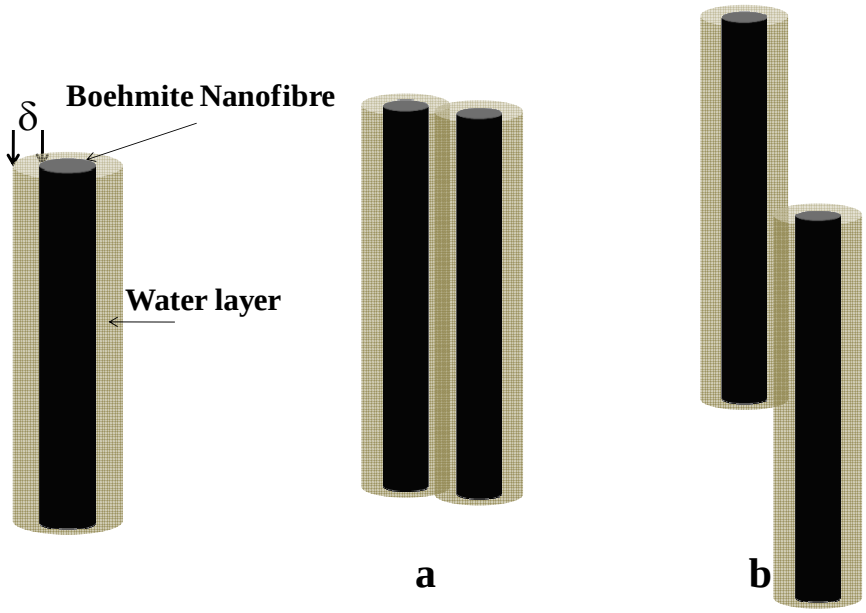

Scheme 2. A schematic illustrating the linear arrangement of boehmite nanofibres driven by hydration repulsive force a) the strongest hydration repulsive force acting between two parallelly orientated nanofibres b) change to linear arrangement to minimize the hydration repulsive force

In our work, the amount of water distributed on the boehmite nanofibres is strictly controlled. In practice, we restrict the thickness of the water layer to 2 ~ 3 nm by calculation, assuming that the water is evenly distributed on the surface of each boehmite nanofibre. For boehmite nanofibres, the hydration repulsive force strongly depends on the orientations of boehmite nanofibres. The hydration repulsive energy is strongest for the parallel orientation of two overlapped nanofibres. As the hydrated boehmite nanofibres are restricted closely by the limited amount of water, there is a strong hydration repulsive force acting between two parallelly orientated nanofibres. They are prone to align to minimise overlapped areas in order to achieve a balance between hydration repulsive energy and van der Waals attractive energy. Therefore, the long bundles are made up of a collection of boehmite nanofibres with a hydration repulsive force acting between them.

The toughness of each bundle is maintained by the Van der Waals force between each of theinterconnected nanofibres. As these hydrated nanofibres are dispersed into oil phase, the toughness of each bundle is also maintained by the Laplace pressure, which is the pressure difference between the inside and the outside of a droplet, expressed by the following Young-Laplace equation:

$$\Delta P \equiv P_{inside} - P_{outside} = \gamma_{ow}\left(\frac{1}{R_1} + \frac{1}{R_2}\right)$$

Where in the case of R_1 being equal to R_2,

$$\Delta P = \frac{2\gamma_{ow}}{R}$$

Where P_{inside} is the pressure inside the droplet, $P_{outside}$ is the pressure outside the droplet, γ_{ow} is the water/oil interfacial tension, R is the radius of the bubble.

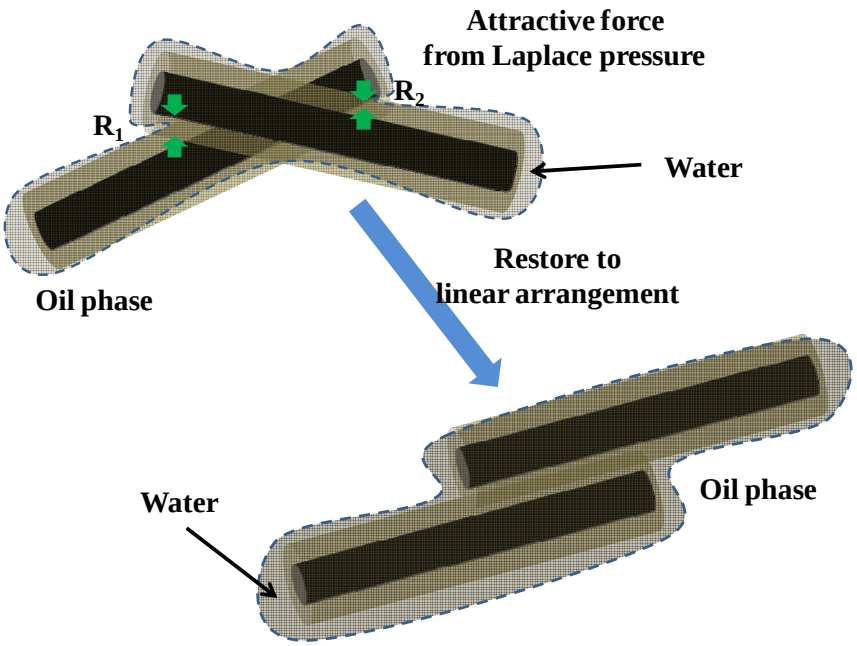

Scheme 3. A schematic illustrating that the linear arrangement is maintained by interfacial force

Indeed, the long bundle of boehmite nanofibres is restricted in a droplet possessing a large aspect ratio. The bend of the bundle will give rise to the interfacial curvatures and generate pressure differences. As the radius of curvature, generated by nanomaterials, is on a nanometer scale, according to the equation the pressure difference will be extremely large. It will result in an attractive force between two nanofibres. Therefore, the bended bundle will readily restore into the linear arrangement of interconnected nanofibres[3].

The long bundles of boehmite nanofibres are capable of forming entanglements with a weak Van der Waals attraction between them to develop self-supporting network structures. This network is fairly stable and can resist sedimentation. From our work, it is evident that the dispersions of these fibrous particles are known to form gels.

In the next step, we used the oil phase to segregate the dispersed long bundles of boehmite nanofibres. The main advantage of this design is that we can exclusively deposit an amorphous ZrO_2 or TiO_2 layer on the outer-surface of boehmite bundles by the localised

hydrolysis of zirconium or titanium alkoxide. This also requires that the amount of water distributed on the boehmite nanofibres is strictly controlled. Since the amount of water is relatively less for the hydrolysis and condensation of zirconia/titania species, in this thesis, the preparation of a fully hydrolysed amorphous layer is realized by two methods: (1) by heating a suspension at elevated temperature to intensify sol-gel reaction, or (2) by post-addition of water to separately control the hydrolysis and condensation processes.

After the drying step, fibrous ZrO_2/Al_2O_3 and TiO_2/Al_2O_3 nanocomposites were transformed by sample calcination. Determined by the *in situ* hot-stage Raman and FT-IR emission spectroscopy, the crystallization of metal oxide proceeds with the calcination temperature increasing, while the boehmite nanofibers transform to the isomorphous γ-Al_2O_3 at 450^{o}C. The interaction between transition metal oxide nanocrystallites and γ-Al_2O_3 can be detected by XPS and ^{27}Al MAS-NMR. In Chapter 4, during the preparation of ZrO_2/Al_2O_3 nanocomposites, XPS results show that the zirconium ions bound to the alumina support lead to a displacement of the bonding energies of $Zr3d_{5/2}$ to the value of 0.9 eV. ^{27}Al MAS-NMR results show that compared with pristine γ-Al_2O_3, pentacoordinated aluminium sites emerge in the nanocomposite materials with this component typically corresponding to amorphous alumina. Identified by the XRD, the tetragonal zirconia nanocrystallites dispersed on alumina cores exhibit crystal sizes much smaller than that of the pristine zirconia prepared under the same conditions. These three characterisation methods unambiguously suggest that the metal oxide nanocrystallites are incorporated onto the alumina support by a small proportion of amorphous alumina which also retards the crystal growth of the metal oxide nanocrystallites.

At this stage, our strategy has succeeded in constructing ZrO_2 and TiO_2 hierarchical nanocomposites. Both syntheses start with the hydrolysis and condensation reactions of their corresponding metal alkoxide precursor, followed with generating an amorphous metal oxide layer around the skeleton of alumina nanofibres to form fibreous morphology. After calcination, the amorphous layer is transformed into a mesoporous layer of metal oxide,

which is assembled by many small nanocrystalites. Using metal alkoxide as precursor is the only prerequisite, and is the only limitation of our synthetic strategy. The more pronounced differences in the synthesis of these two nanocomposites are that the zirconium butoxide is relatively sensitive to hydrolysis and condensation, while the titanium species is relatively sensitive to the thermal treatment. As we described in chapter 5, these defferences in properties of metal alkoxide also result into the modification of synthetic processes, and this should be noticed if preparing other metal oxide nanocomposites.

We also examined catalytic applications for our resultant nanocomposites. In the literature, crystalline ZrO_2 and TiO_2 usually exhibit high intrinsic activities in catalysis reactions as catalyst or catalyst support. To the best of the author's knowledge, the performances for ZrO_2 and TiO_2 nanocomposites with core-shell structure and hierarchically meso-macropores have not been previously examined.

A series of 1D (fibrous) ZrO_2/Al_2O_3 with different Zr molar percentage was developed into solid superacids by loading sulfate ions. We evaluated the performances of these fibrous solid superacids by the benzoylation reaction of toluene with benzoyl chloride at reflux. The fibrous superacid with 50 % Zr molar percentage exhibits higher activity than that of the pristine sulfated zirconia by a factor of 1.4. The high activity of such a catalyst is attributed to the large surface area of zirconia nanocrystallites being readily accessible to the reactant molecules due to the unique core-shell structure.

Moreover, we also prepared a serious of TiO_2/Al_2O_3 nanocomposites with various Ti/Al molar ratio and different morphologies including fibrous TiO_2/Al_2O_3 nanocomposites and titania microspheres segregated by alumina nanofibres. In this case, we noted that morphology is a crucial aspect for the performance of a photocatalyst. The photocatalyst with fibrous morphology exhibits superior catalytic performance. This is because of two aspects: first, for fibrous catalyst the TiO_2 nanocrystallites are evenly dispersed on the alumina bundles ensuring the majority are exposed to the light irradiation, and, second, the

particles with fibrous morphology are highly dispersive in reaction system. Whereas, for the photocatalyst with microspherical morphology only the first layer of TiO_2 nanocrystallites can be irradiated, this results in relatively low utilisation of surface area for photocatalysis. Indeed, the importance of morphology exhibited in our work even surpasses some other factors usually discussed in photocatalyst evaluation, such as band gap of anatase, crystal size or phase composition.

Besides, the photocatalytic performance of fibrous TiO_2/Al_2O_3 was improved by calcination at elevated temperature to increase crystallinity and reduce the recombination rate of photo-induced electron-hole pairs. The fibrous nanocomposite calcined at 750^{o}C exhibits the highest catalytic performance for the degradation of phenol. In fact, its degradation activity of per TiO_2 unit is very close to the gold-standard commercial photocatalyst, P25. Furthermore, we found that the fibrous particles were much easier to recover by filtration than with ultrafine nanopowders. We proposed that this is because the aggregation of fibrous particles during filtration also contains a considerable amount of large interparticle voids which can support a high filtration flux. This knowledge has been noted to be important for designing novel photocatalyst for industrial applications.

REFERENCE

(1) Fang, Z. N.; Xue, H. T.; Bao, W.; Yang, Y.; Zhou, L. W.; Huang, J. P. *Chem. Phys. Lett.* **2007**, *441*, 314.

(2) Briscoe, W. In *Colloid Science: Principles, methods and applications*; Cosgrove, T., Ed.; John Wiley and Sons, Ltd, Publication: Chichester, 2010, p 329.

(3) Hughes, R. In *Colloid Science: Principles, methods and applications*; Cosgrove, T., Ed.; John Wiley and Sons, Ltd, Publication: Chichester, 2010, p 18.

Appendices

Chapter2

Scheme 1. Preparation of the rhodium nanoparticle catalyst....26

Chapter3

Chapter4

Scheme 1. Benzoylation of toluene with benzoyl chloride....74

Scheme 2. Schematic diagram of catalytic reactor for Benzoylation of toluene with benzoyl chloride....77

Chapter5

Scheme 1. Schematic for Formation of TiO_2/Al_2O_3 with different morphologies....112

Chapter6

Scheme 1. Schematic of the morphological effects for these catalysts with various Ti/Al molar ratios a) catalyst with mircospheric morphology and b) catalyst with fibrous morphology....135

Scheme 2. Schematic mechanism of the photodegradation of SRB on TiO_2 particles under visible light irradiation[26]....137

Scheme 3. Proposed enhanced mechanism of dye degradation on Ti-3-450 under UV irradiation....139

Scheme 4. Schematic shows that the fibrous catalyst can be separated readily and rapidly for reuse by filtration....146

Chapter7

Scheme 1. The suspension state of boehmite nanoifibres a) in oil phase b) in water phase,and c) in oil phase with the aid of oil/water interface....152

Scheme 2. A schematic illustrating the linear arrangement of boehmite nanofibres driven by hydration repulsive force a) the strongest hydration repulsive force acting between two parallelly orientated nanofibres b) change to linear arrangement to minimize the hydration repulsive force....153

Scheme 3. A schematic illustrating that the linear arrangement is maintained by interfacial force....155